ABSTRACT

SHAPED CHARGES HAVING A POROUS TUNGSTEN LINER -AN EXPERIMENTAL AND THEORETICAL STUDY OF METAL COMPRESSION, JET FORMATION, AND PENETRATION MECHANICS

by
Brian Edward Fuchs

The use of porous tungsten as a liner for shaped charges to improve their penetration was proposed by Ki-Hwan Oh in his invention disclosure "Shock Extrusion of Ingots from Powders or Solids", at the New Mexico Institute of Mining and Technology, Socorro NM on June 7, 1988. The intention was to increase the ductility of the normally brittle metal by heating the liner to a high temperature by shock compaction during its acceleration just before jet formation.

The feasibility of increasing the ductility of tungsten in this way is the subject of the present study. The theory and prior experimental studies of porous metal compression by shock waves are reviewed, with special attention to ways for determining the temperature of the compressed material. In this theoretical study a new equation of state is developed, and experimental shaped charges with porous tungsten liners are designed and tested. One of the shaped charges was also modeled on a computer for this study.

An improved equation of state for porous tungsten is developed and compared with experimental data from the literature and other equations of state. The proposed equation of state shows improved correlation to experimental data for tungsten with high initial porosity. This is achieved while maintaining the close correlation to data obtained by most equations of state at higher initial densities.

After preliminary studies, two shaped charge liner designs having porous tungsten liners with initial densities of 65% and 80% of the solid density were designed, manufactured, and test fired. Steel target plates were used to determine the penetration. As shown by the flash radiography, the jets formed were particulated on a small scale, causing the density of the jets to diminish with distance from the charge. A relatively long distance between the shaped charge and the target plates was required to provide room for the flash radiographs. This caused low jet densities and a particulated jet that had little penetration into the target plates.

The jet formation for the liner with initial density 65% of the solid was modeled by continuum hydrodynamic computations using Lawrence Livermore National Laboratory's CALE computer code. Near zero strength was used for the jet after formation, as well as a fitted equation of state for tungsten with low initial porosity. The modeling confirmed that low strength in the jet formation caused the fine particulation of the jet as it stretches.

By using a combination of techniques developed in this work, improved temperature determinations were made. These indicated that the temperature of the shock-compressed tungsten liner varied from 350°C at the sides of the cone to 2,087°C at the apex. The shaped charge needs to be redesigned in order to achieve the temperatures of approximately 1000°C required to beneficially change the properties of tungsten. The study concludes with recommendations for future work. Proposals for shaped charges with initially porous tungsten liners that may form coherent jets are made. A test method to verify predicted penetration characteristics of finely particulated jets, developed in this study, is discussed.

SHAPED CHARGES HAVING A POROUS TUNGSTEN LINER -AN EXPERIMENTAL AND THEORETICAL STUDY OF METAL COMPRESSION, JET FORMATION, AND PENETRATION MECHANICS

by
Brian Edward Fuchs

A Dissertation
Submitted to the Faculty of
New Jersey Institute of Technology
in Partial Fulfillment of the Requirements for the Degree of
Doctor of Philosophy

Department of Mechanical Engineering

January 1997

APPROVAL PAGE

Title of Thesis: Shaped Charges Having a Porous Tungsten Liner-an Experimental and Theoretical Study of Metal Compression, Jet Formation, and Penetration Mechanics

Name of Candidate: Brian Edward Fuchs
Doctor of Philosophy, 1996

Thesis and Abstract Approved:

Dr. John Droughton, Thesis Advisor — Date
Professor of Mechanical Engineering, NJIT

Dr. Per-Anders Persson, Committee Member — Date
Professor of Mineral and Environmental Engineering
Senior Scientist EMRTC, Director RCEM
New Mexico Institute of Mining and Technology

Dr. Pasquale J. Florio, Committee Member — Date
Associate Professor of Mechanical Engineering,
NJIT

Dr. Robert P. Kirchner, Committee Member — Date
Professor of Mechanical Engineering, NJIT

Dr. Rong-Yaw Chen, Committee Member — Date
Professor of Mechanical Engineering, NJIT

BIOGRAPHICAL SKETCH

Author: Brian Edward Fuchs

Degree: Doctor of Philosophy

Undergraduate and Graduate Education:

- Doctor of Philisophy in Mechanical Engineering
  New Jersey Institute of Technology, Newark, NJ, 1997
- Master of Science in Mechanical Engineering
  New Jersey Institute of Technology, Newark, NJ, 1987
- Bachelor of Science in Mechanical Engineering
  New Jersey Institute of Technology, Newark, NJ, 1983

Major: Mechanical Engineering

Publications:

B. Fuchs and P. Lu "Implementation of Inverse Multiprofile Streak Technique" Special Publication ARDEC-SP-87001 June 1987.

E. Baker, E. Dalyrmple, B. Fuchs, J. Howell, and P. Lu "Axisymmetric Steady State Detonation Mach Stem and Semi-Infinite Steel Witness Plate Interaction" Technical Report ARDEC-TR-88008, July 1988.

B. Fuchs "Picatinny Arsenal Cylinder Expansion Test and a Mathematical Examination of the Expanding Cylinder" Technical Report ARAED-TR-95014, October 1995.

Travers, B. E. C., B. Fuchs, A. Rapko, and M. Joyce. "Development of a Formulation for the Special Operations Force (SOF) Enhanced Moldable Explosive Charge (SEMEC) Technical Report ARAED-TR-95024, October 1995.

B. Fuchs, E. Baker, E. Dalyrmple, and P. Lu "Measuring Detonation Front Configuration via Flash Radiography and Ultra High Speed Streak Photography". Proceedings of SPIE, the International Society for Optical Engineering, Volume 832 17-19 Aug. 1987 San Diego, California. pp. 130-137.

E. Baker, B. Fishburn, B. Fuchs, and P. Lu "Formation and Structure of Axisymetric Steady-State Detonation Mach Stems in Condensed Explosives". Journal of Energetic Materials. Vol. 5 Sept.-Dec. 1987 pp. 239-256.

P. Lu, B. Fuchs, J. Costello, and R. King "Sympathetic Detonation Sensitivity Evaluation of the Less Sensitive 25 mm Munition Propellant:. 1989 JANNAF Propulsion Systems Hazards Subcommittee Meeting, San Antonio TX. Feb. 23, 1989.

P. Lu, P. Hui, A. Grabowski, R. King, and B. Fuchs "Blast Measurements of Shaped Charge Jet Impacted Gun Propellants". 1989 JANNAF Combustion Meeting.

Ng., William, Richard Fong, Brian Fuchs, Brian Travers, Bernie Rice. "New Selectable EFP Warhead Technology". A.D.P.A. 41st Annual Bomb & Warhead Technical Meeting. 15-16 May 1991, Naval Ocean Systems Center, Point Loma San Diego CA.

R. Campbell, E. L. Baker, and B. Fuchs. "Computational Design of Shaped Charge Jet Attack Experimentation". Proceedings of the SCS 1993 Eastern Multiconference, Ballistics Conference, Arlington, Va. March 1993

Baker, E. L., T. Voung, B. Fuchs "EFP and Shaped Charge Concrete Penetration" 7th TARDEC Ground Vehicle Survivability Symp, Monterey, CA, March 1996.

Patents:

"High Explosive Assembly for Projecting Long Rods". E. Baker, B. Fuchs, B. Fishburn, P. Lu, DAR-35-87.

"Tapered Disc Penetrating Explosive Charge". B. Fuchs, B. Fishburn, E. Baker, P. Lu, DAR-17-88.

ACKNOWLEDGMENT

The completion of this thesis required the cooperation between two institutes of higher learning and my employer, U.S. Army ARDEC at Picatinny Arsenal. I wish to thank my advisor Dr. John Droughton at the New Jersey Institute of Technology, Dr. Per-Anders Persson at the New Mexico Institute of Mining and Technology where I spent a year researching explosives, and Dr. Pai Lu and Mr. Joseph Orosz, my past and present supervisors at ARDEC. I also want to thank my fellow employees at Picatinny Arsenal, particularly Mr. John Howell and Mr. Gerard Gillen who assisted in the explosive testing. I also want to thank my wife Sandra and our three children, Edward, Alexander, and Erika, and my parents for their patience and support during this endeavor.

TABLE OF CONTENTS

TABLE OF CONTENTS
(Continued)

Chapter **Page**

TABLE OF CONTENTS
(Continued)

TABLE OF CONTENTS
(Continued)

TABLE OF CONTENTS
(Continued)

Chapter **Page**

LIST OF TABLES

LIST OF FIGURES

LIST OF FIGURES
(Continued)

LIST OF FIGURES
(Continued)

LIST OF FIGURES
(Continued)

CHAPTER 1

INTRODUCTION

A variety of methods are available for concentrating the mechanical effect of a detonation. A commonly used method utilizes the Monroe effect, Ref. (1), also known as the cavity effect. This is based on the observation that a plate next to an explosive will have a deeper dent after detonation in areas close to where the explosive contained a cavity. The cavity allows the explosive's reaction products room to be accelerated into the cavity, focusing the momentum to impact the opposite side of the cavity. The effect is enhanced if the cavity is lined with some non-reacting material, usually metal. Frequently, the cavity and liner are cone-shaped, and the arrangement is referred to as a "shaped charge".

In the utilization of a shaped charge the explosive is first detonated. The detonation is a rapid chemical reaction that drives a shock wave through the material. The chemical reaction is completed in a thin layer just behind the shock wave. The detonation wave on impact with the liner causes a shock wave to travel through the liner. The initial shock accompanied by the following high pressure gas collapses the liner towards the axis of the cone. The solid liner at the extreme strain rates caused by the detonation behaves as liquid. The collapse forces the inner layer of the liner into a rapidly moving jet, concentrating the force of the detonation, and a following slower slug. The jet, with its high velocity, has the ability to penetrate large distances of a target material. Shaped charges are used in commercial, demolition, and military applications. Typical civilian

applications include perforator charges for increasing the flow from oil wells, and for clearing plugged exits for molten iron in steel mills.

Shaped charge performance depends on many factors, such as the density, velocity, straightness, and breakup time of the jet. Straight, coherent uniform jets of high density and velocity deliver the deepest penetration. Density and velocity are material dependent. Jet straightness is related to the symmetry of collapse of the liner, which is principally determined by the structural symmetry and uniformity of the liner, and the symmetry of the detonation shock wave. Physical uniformity of the liner is a matter of fabrication; symmetry of the shock wave depends on the uniformity of explosive fill and its initiation. Confinement, in the form of an external casing, surrounding the explosive charge, may also affect the symmetry to some extent. Jet break-up is related to the plastic deformation properties of the material before and after shocking. High speeds of sound within the jet material are desirable because they permit higher speeds of liner collapse before compressibility effects cause formation of incoherent jets.

1.1 Possible Shaped Charge Liner Materials

Liners are typically made from oxygen free copper, which can undergo large plastic deformation without breaking, are easily fabricated, and are economical and readily available. However, they have only moderately high density. Many materials have a higher density than copper, and would be potentially more effective than copper as a liner for shaped charges. The Los Alamos publication "Selected Hugoniots", Ref (2), provides a listing of those that have been used in explosive systems.

Table 1 Material Properties from Selected Hugoniots

Material	Density ρ_o gm/cc	Speed of Sound c_o km/sec
Iridium	22.284	3.916
Platinum	21.419	3.598
Rhenium	21.021	4.184
Gold	19.240	3.056
Tungsten	19.224	4.029
Tantalum	16.654	3.414
Mercury	13.540	1.490
Hafnium	12.885	2.964
Rhodium	12.428	4.807
Palladium	11.991	3.948
Thallium	11.840	1.862
Thorium	11.680	2.133
Lead	11.350	2.051
Silver	10.490	3.229
Molybdenum	10.206	5.124
Bismuth	9.836	1.826
Copper	8.930	3.940

By selecting the materials from this list that have a higher speed of sound than copper, a selection of materials that might be used to fabricated superior shaped charges is made. These materials in order of the highest speed of sound to the lowest are: molybdenum, rhodium, rhenium, tungsten, and palladium. These speeds of sound are fitted from shock speed/particle velocity measurements and are appropriate for the present investigation since they are based on high pressure shock conditions. They differ from the conventionally determined and reported speeds of elastic sound which, for example are 5.22 and 4.76 km/sec for tungsten and copper, respectively Ref. (3).

Based solely on speed of sound and density considerations, these materials would be more suitable than copper. However most are too expensive to be practical for use in shaped charges. Only molybdenum and tungsten are available in sufficient quantities at reasonable cost. While molybdenum has the higher speed of sound, tungsten's significantly higher density makes it the more attractive alternative. Tungsten is brittle at room temperature, but has greater ductility at elevated temperature. If the ductility problem could be overcome, tungsten would make a superior liner for shaped charges.

1.2 Porous Tungsten as a Shaped Charge Liner Material

In the course of collapse of a solid metal liner leading to formation of the jet, the temperature of the material is raised, but not to a degree sufficient to permit plastic deformation of fully dense tungsten. Porous metal can be compacted by the "free flight powder compaction forging" method developed at the Center for Explosives Technology Research at the New Mexico Institute of Technology at the New Mexico Institute of

Mining and Technology, Socorro, NM, Ref (4). In explosive compaction of porous materials, including porous tungsten, the compaction aspect will contribute an incremental heating component. The question is whether this incremental heating component, under shock conditions as they might exist in a shaped charge, would contribute sufficient additional heating beyond that normally experienced by the non-porous material to permit plastic deformation of tungsten. Porous brittle metals are being utilized in shaped charges for oil well perforation, where the intention is to avoid the creation of a slug which could block the hole. Little is known about the pertinent effects of porosity in these oil well perforators.

The temperature dependence upon the properties of tungsten is known under a pressure around one atmosphere. These properties were determined under equilibrium conditions over longer time periods, much longer than those prevailing under shock compression conditions in shaped charges. Crystal growth that can occur under the static conditions at which these temperature dependencies were determined cannot occur in the extremely short time periods of the shock process. The effect of temperature on tungsten's properties under short-term shock conditions cannot be projected from data obtained under long-term observations, but must be determined experimentally.

1.3 Research Objectives

In order to evaluate the feasibility of porous tungsten as a shaped charge liner the following research objectives were pursued:

1. A new equation of state for porous tungsten was developed and utilized for computing shock temperatures.

2. Computer modeling of the jet formation process was completed to verify the assumptions concerning strength properties and collapse process of the shocked material in a porous tungsten shaped charge. Equation of state parameters were fitted for porous tungsten.

3. Shaped charges were designed, fabricated, and tested.

CHAPTER 2

LITERATURE SURVEY

The literature survey for this work covers several diverse areas of warhead design. In order to clarify the literature survey, detonations have been separated from shocks. The review of detonations has been placed in the appendix.

2.1 Shock Waves in Solids

Ideal detonation waves are extremely rapid forms of combustion characterized by a constant velocity shock wave which initiates and supports the following chemical reaction. The detonation transmits or generates shock waves into adjacent non reacting materials. The extreme pressure from detonations is far beyond the mechanical strength of materials. Therefore, the internal stresses caused by the material's strength may be ignored for such conditions. It is more important to consider the compressibility of solids.

2.1.1 Fundamental Equations of Shock Discontinuities in Solids

One dimensional shock interactions are assumed. Figure 1 shows the conditions at either side of a shock front propagating through a solid at rest.

There are five unknown variables required to determine the final state of the system: density, pressure, shock velocity, energy, and particle velocity. Some information on the relationships between these variables can be obtained from the conservation equations, forming the Rankine-Hugoniot relations, Refs. (5) and (6).

The equation for the conservation of mass with a coordinate system moving with the detonation front is used. In this coordinate system, the undisturbed material is moving with a velocity u_s toward the front. The variable u_p is the particle velocity of the shocked material in a fixed reference frame.

$$\rho_o u_s = \rho(u_s - u_p) \tag{2.1}$$

where: ρ is the density

ρ_o is the initial density

u_s is the shock speed

u_p is the particle velocity

In applying the conservation of momentum, a control volume expanding with the front is used in a fixed reference frame. The control volume then includes all of the shocked material. The shock velocity moves forward at velocity u_s taking in the material at rest, $u_o = 0$, and ρ_o to a final velocity of u_p. The conservation of momentum becomes:

$$P - P_o = \rho_o u_s u_p \tag{2.2}$$

where: P_o is the initial pressure

P is the shock pressure

The quantity $\rho_o u_s$ is defined as the shock impedance

This work follows the convention in detonation and shock physics where the specific internal energy is represented by the variable e, and not the variable u used in thermodynamics, since u is used here for velocity.

From the Conservation of Energy:

$$\Delta e = P_o v_o - Pv + \tfrac{1}{2}\left(u_s^{\,2} - \left(u_s - u_p\right)^2\right) \tag{2.3}$$

The conservation of energy can be expressed as a function of pressure and volume. From equation 2.1:

$$\left(u_s - u_p\right) = \frac{v}{v_o} u_s$$

and equations 2.1 and 2.2

$$u_s^2 = P v_o \left(\frac{v_o}{v_o - v}\right)$$

into equation 2.3 with the assumption that P_o=0

$$\Delta e = -Pv + \tfrac{1}{2} P v_o \left(\frac{v_o}{v_o - v}\right)\left(1 - \frac{v^2}{v_o^2}\right)$$

which reduces to

$$\Delta e = \tfrac{1}{2} P\left(v_o - v\right) \tag{2.4}$$

The equations of mass, momentum, and energy are not sufficient to solve for the five unknowns. An equation of state describing the properties of the specific material considered is required. The simplest and most commonly used form of an equation of state is the linear u_s-u_p fit.

$$u_s = c + su_p \tag{2.5}$$

where: u_s = shock speed,

u_p = particle velocity.

c = a fitting constant, approximately the speed of sound, about 8 km/s to 0.7 km/s.

s = a fitting constant, about 2 to 0.7.

This equation represents both condensed solids and liquids. Sometimes a u_p^2 term containing a third constant is added to improve the fit. The state for all possible shocks can be plotted on a curve, the Hugoniot curve. Using equations 2.2 and 2.5:

$$P = \rho_o\left(c + su_p\right)u_p \tag{2.6}$$

This yields the solid Hugoniot curve in the pressure versus particle velocity plane. The Hugoniot curves are typically plotted in the pressure verses particle velocity plane. An example with a variety of materials is shown in Figure 2. This figure also shows the reverse Hugoniot and expansion isentropes for several explosives (see Appendix 1).

The Rayleigh line is defined as the line joining the initial state and the shocked state. In the pressure particle velocity plane, its slope is given by the conservation of momentum, equation 2.2:

$$\frac{P - P_o}{u_p} = \rho_o u_s \tag{2.2}$$

Under some conditions, such as certain phase changes, the Rayleigh line cannot be drawn to the final pressure without crossing the Hugoniot curve at lower pressures. For these conditions there are two shock waves of different velocities.

Other relationships can be developed among the variables. Some are these relationships are given, using the simplifying assumption that P_o=0, Ref. (5).

$$P = \frac{c^2(v_o - v)}{\left[v_o - s(v_o - v)\right]^2} \tag{2.7}$$

$$e = \frac{1}{2}\left(u_p^{\ 2}\right) \tag{2.8}$$

$$P = 2e\frac{\sqrt{c} + s\sqrt{2e}}{\sqrt{2e + \left(\sqrt{c} + s\sqrt{2e}\right)(v_o - 1)}} \tag{2.9}$$

$$v = \frac{c}{2s^2\rho}\left[\sqrt{1 + \frac{4sv_o}{c}P} + \frac{2s(s-1)v_o}{c}P - 1\right] \tag{2.10}$$

$$e = \frac{1}{2}\frac{c(v_o - v)^2}{\left(v_o - s(v_o - v)\right)^2} \tag{2.11}$$

2.1.2 Shock Waves from Plate Impacts

In situations when the initial particle velocity is not zero, for example with colliding plates, the equations must be modified to allow for an initial velocity. The matching of shock conditions between two dissimilar materials is also possible. These conditions are represented in Figure 3, showing the one-dimensional interaction between two materials following a plane impact.

Equation 2.1 becomes:

$$\rho_o(u_s - u_o) = \rho(u_s - u_p) \tag{2.12}$$

Equation 2.2, with an initial velocity and pressure, becomes:

$$P - P_o = \rho_o(u_s - u_o)(u_p - u_o) \tag{2.13}$$

Equation 2.5, for an initially moving body becomes:

$$u_s - u_p = c + s(u_p - u_o) \tag{2.14}$$

When the materials interact, not only must these conservation conditions be met but the pressure and the mass velocity must also be continuous and equal at the boundary. The state of the materials must change to meet these conditions. The above equations can be used to solve the pressure, particle velocity, and shock speed at the plane of contact, collision. The solution is often easier to obtain graphically by using the Hugoniot chart, Figure 2, and equation 2.6. For the conditions in Figure 3, a graphical solution is shown in Figure 4.

The Hugoniot curve for the projectile material is reflected in the pressure axis and moved in the velocity axis such that the initial velocity is at zero pressure. This accounts for the initial conditions and for the shock wave moving backwards within the material.

The density of the solid shocked once can be determined from equation 2.12:

$$\rho_o(u_s - u_o) = \rho(u_s - u_p) \tag{2.12}$$

by using equation 2.5 to eliminate the shock speed u_s.

$$\frac{\rho}{\rho_o} = \frac{c + su_p}{c + (s-1)u_p} \tag{2.15}$$

Equation 2.15 cannot be used for repetitive shocks if ρ_o is taken as the unshocked value of density. The temperature, and therefore the density, will have been changed by the preceding shocks.

The graphical method is easily applied to many problems, see Figure 4. Since the Hugoniot curves are frequently reflected, many Hugoniot graphs are placed on transparencies. Reflections of the materials are then made by flipping one Hugoniot curve over and placing it on another chart. Wax pencils are then used to mark the charts and determine the state of the materials. If the shocks are assumed not to attenuate, the materials after a chain of interactions or reflections in the shock waves can easily and clearly be graphically determined.

2.1.3 Shock Transfer Between Materials

When a shock wave passes from one material to another, the shock compression properties of both materials must be considered. The interactions can be subdivided into three types, with reference to the initial materials: (1) shocks into material with a higher shock impedance, (2) shocks into material with the same shock impedance, and (3) shocks into material with a lower shock impedance. If the impedances are equal the shock pressure remains unchanged, as if a shock were being transmitted within the same material. For higher impedance target materials, such as the shock being transmitted from a light into a heavy material, a shock wave is reflected back into the light material. This increases the pressure in both the impacting and the impacted material (see Figure 5).

The relative impedances of the materials determine the reflected pressures within the materials. For low impedance materials, such as a shock being transmitted from a heavy to a light material or even into air, the pressure is reduced. Since shock waves do not exist that lower pressure, a rarefaction wave enters the impacting material, as shown in Figure 6. Unlike the shock wave, the rarefaction wave is not a discontinuity; the pressure in it is reduced gradually over a finite distance. It is often possible to still use the Hugoniot curve to describe the release of pressure in the material, since this closely matches the isentrope Ref. (6).

2.1.4 The Shock Interactions of Detonations

The procedures applied above are equally applicable to interactions of detonations and non-reacting media. A brief discussion on the shock physics of detonation is given in the appendix. The Hugoniot chart in Figure 2 includes not only solid Hugoniot curves, but also the Hugoniots curves and expansion isentropes for some typical explosives. The chart has the explosive Hugoniot curves reflected about the initial conditions, the CJ point, represented by a dot on each Hugoniot curve. The CJ point and detonations are discussed in the appendix. By presenting the chart in this fashion the pressures and particle velocities for the one-dimensional interactions between these explosives and any of the other materials are immediately obtainable.

2.1.5 The Stability of Shock Waves

When a pressure pulse travels through a material, the material is brought to a state of higher pressure, temperature, and density. Consequently the speed of sound in the material is increased. For the mass behind the shock front, it is the speed $c + u_p$ that determines the communication of conditions on the shock front. The large value of $c + u_p$ causes a degradation of the pressure at the front, Ref. (5).

From thermodynamics, for a release along the isentrope:

$$de=Tds - Pdv \tag{2.16}$$

for $ds = 0$, then

$$de = -Pdv \tag{2.17}$$

Initially solid materials have a final volume, at zero pressure, which is slightly larger than the initial volume. This is due to the heating of the material by the shock wave, Figure 7.

A reflected wave within the material can combine with a rarefaction wave to form a strong tensile wave. If the magnitude of the tension is such that it exceeds the ultimate strength of the material, fracture will occur. This is called spalling. The spalled surface on metals has a distinctive rough appearance that experts can easily identify. This phenomenon has been utilized in anti-tank weapons such as the high explosive plastic or HEP charges. These charges can destroy some armored vehicles without penetrating. The response to this has been the addition of spall liners to the inside of the vehicles and spaced armor.

2.2 The Effect of Porosity on Shock Properties

The previous relations were derived for non-porous materials and require modifications to provide a simplified explanation of the shock properties of porous materials. Porous materials have relatively large changes in volume in shock processes. From equation 2.4, $e = {}^1/_2\ P(v_o\text{-}v)$, it can be seen that after shock compaction porous materials have much higher internal energies and temperatures at the compressed state. The speed of sound in these materials is greatly increased due to the large compression and high temperature.

The shock compression can be separated into three different regions, see Figure 8: Ref. (7)

1. At low pressures elastic compression prevails, without permanent damage to the material.
2. At higher pressures beyond the yield strength of the porous material, void collapse begins. This begins the plastic region of the collapse process.
3. At higher pressures yet, the voids have collapsed and the material is fully dense.

For relatively high porosity materials in the elastic portion of the shock, Hugoniot curve changes in volume are due mostly to the changing geometry of the pores. For materials with lower porosity, the change in volume is due more to the compression of the solid portion of the material. Shock pressures from detonations are generally much

greater than the elastic portion of the Hugoniot curve. The elastic portion of the Hugoniot curve is not required or covered in this work.

The release portion porous materials differs from that of solid materials. The volume at zero pressure after release is typically smaller than the initial volume due to the void collapse, see Figure 9. An initially solid material will have a slightly larger volume due to internal heating.

At low pressures and high initial porosities the plastic portion of the Hugoniot curve is governed more by pore collapse than by compression of the solid portion of the material. At higher pressure the compression of the solids becomes significant. A physical description of the shock Hugoniot curve for completely compressed materials can be extended to the partially compressed region to account for the compression of the solid portion. For this reason the completely compressed region will be covered first.

2.2.1 Initially Porous Materials Completely Shock Compressed

2.2.1.1 Mie-Grüneisen Equation of State: The Mie-Grüneisen equation of state was originally developed from statistical mechanics of crystals, Ref. (8) (5). This equation of state has been applied to higher pressure and energy states with a moderate amount of success. This equation of state assumes:

$$\frac{\gamma}{v} = \left.\frac{\partial P}{\partial e}\right|_v = \text{a constant} \qquad (2.18)$$

where:

γ= is defined as the Grüneisen gamma

This equation of state derives its theoretical basis from the theory of the lattice structure of solids, which does not apply to states other than crystalline solids. Despite this, the Mie-Grüneisen equation of state has been applied to liquids with energies not far off the solid Hugoniot curve. In application the pressure and energy of an initially solid Hugoniot curve is used as a basis for finding the pressure of the porous material at the same volume. This is shown in Figure 10. The pressure is computed by the following equation:

$$P_H = P_s + \frac{\gamma}{v}(e_H - e_s)$$

where: P_H = pressure of porous material along its Hugoniot
P_s = pressure of solid at the same volume
e_h = energy of the porous material
e_s = energy of the solid at the same volume (2.19)

By using the pressure, volume relationship, equation 2.7, for the solid material:

$$P = \frac{c^2(v_o - v)}{\left[v_o - s(v_o - v)\right]^2} \tag{2.7}$$

and equation 2.4 for the energy terms

$$e = \tfrac{1}{2} P(v_o - v) \tag{2.4}$$

in equation 2.19, the relationship between volume and pressure can be determined for the porous material:

$$P = \frac{\left[2v - \gamma(v_o - v)\right]c^2(v_o - v)}{\left[2v - \gamma(v_{oo} - v)\right]\left[v_o - s(v_o - v)\right]^2} \tag{2.20}$$

A plot of equation 2.20, Figure 11, shows that for large porosities, increasing shock pressures are predicted to cause an increase in volume. This conclusion is supported by Krupnikov et. al. Ref. (9). Data from Krupnikov et. al. and other sources, Ref. (9)(10)(11)(12)(13) were examined, table 1. A comparison between these data and the Mie-Grüneisen equation of state is shown in Figure 12. The Oh-Persson incomplete compaction equation, covered later, was used for this graph.

The tungsten data supports the conclusion of Krupnikov et. al. For the lowest initial densities the specific volume on the porous Hugoniot curve increased with increasing shock pressures. This behavior is not as pronounced as the Mie-Grüneisen equation of state predicts. The data show that this is because the value of the Mie-Grüneisen gamma decreases with increasing internal energies.

Shock compression experiments with porous materials tend to show variations in the measured pressures. This is possibly due to density variations within the matrix for which an average value may not be suitable.

2.2.1.2 Volume Limitations on the Mie-Grüneisen Equation of State: The u_s-u_p equation of state for a solid material predicts a volume for which the pressure goes to infinity, Ref. (14). From equation 2.7:

$$P = \frac{c^2(v_0 - v)}{\left(v_0 - s(v_0 - v)\right)^2} \tag{2.7}$$

Then $P \rightarrow \infty$ when $c^2(v_o - v) = \infty$ or $(v_o - s(v_o - v)) = 0$. Only the second of these expressions is possible. Then:

$$v = \frac{v_o(s-1)}{s} \quad \text{For } P \rightarrow \infty. \tag{2.21}$$

The Mie-Grüneisen equation of state yields another point at which $P \rightarrow \infty$.

For equation 2.19:

$$P = P_s + \frac{\gamma}{v}(e_p - e_s) \tag{2.19}$$

using equation 2.4 for the energy of the porous material

$$e_p = \tfrac{1}{2} P(v_{oo} - v) \tag{2.4}$$

where: v_{oo} is the initial specific volume of the porous material

then

$$P = P_s + \frac{\gamma}{v}\left(\tfrac{1}{2} P(v_{oo} - v) - e_s\right)$$

and rearranging

$$P\left(1 - \tfrac{1}{2}\frac{\gamma}{v}(v_{oo} - v)\right) = P_s - \frac{\gamma}{v} e_s \tag{2.22}$$

Then $P \rightarrow \infty$ when:

$$\left(1 - \tfrac{1}{2}\frac{\gamma}{v}(v_{oo} - v)\right) = 0 \quad \text{if } P_s - \frac{\gamma}{v} e_s \text{ is assumed to be limited}$$

then

$$v = \frac{v_{oo}\gamma}{2+\gamma} \qquad \text{For } P \rightarrow \infty \tag{2.23}$$

This limiting case for porous materials predicts that the material cannot be compressed beyond a limiting specific volume. For large initial volumes, with large initial porosity, this theory predicts that the solid volume of the material is not achievable at any pressure. This phenomenon has been reported in the literature for cotton wool, Ref. (15).

2.2.1.3 The Grüneisen Parameter Determined from Ambient Conditions: The Grüneisen gamma can be determined from some of the typical material properties measured at low pressures and ambient conditions that are available in material handbooks, Ref. (5).

Since:

$$\gamma = v\frac{\partial P}{\partial e}\Big)_v = v\frac{\partial P}{\partial T}\Big)_v \frac{\partial T}{\partial e}\Big)_v \tag{2.24}$$

and:

$$\frac{\partial P}{\partial T}\Big)_v = \frac{\partial P}{\partial v}\Big)_v \frac{\partial v}{\partial T}\Big)_v \qquad \text{by definition} \quad \frac{1}{c_v} = \frac{\partial T}{\partial e}\Big)_v \tag{2.25}$$

Then

$$\gamma = \frac{v}{c_v}\frac{\partial P}{\partial T}\Big)_v = -\frac{v}{c_v}\frac{\partial P}{\partial v}\Big)_T \frac{\partial v}{\partial T}\Big)_P \tag{2.26}$$

The volumetric thermal expansion is:

$$3\alpha = \frac{1}{v}\frac{\partial v}{\partial T}\Big)_T \tag{2.27}$$

The isothermal compressibility is:

$$K = -\frac{1}{v}\frac{\partial v}{\partial P}\Big)_T \tag{2.28}$$

Then the Grüneisen parameter can be expressed as:

$$\frac{\gamma}{v} = \frac{3\alpha}{c_v K} \tag{2.29}$$

Figure 12 shows the computed Mie-Grüneisen equation of state pressures for porous tungsten. The Mie-Grüneisen equation of state predicts the pressures accurately for low initial porosities, but rapidly becomes inaccurate at high initial porosities. From this figure it can be seen that the value of $\left.\frac{\partial P}{\partial e}\right|_v$ must be diminishing at higher temperature and energy states. McQueen et. al. also investigated the Grüneisen parameter and determined it to be nearly constant within the temperature ranges experienced in most shock interactions. Ref. (16).

The temperature dependence of Grüneisen's gamma was studied by Sternberg. Ref. (17). He determined that the constant gamma equation of state is valid up to a substantial fraction of the melt temperature. This explains the success of the constant gamma equation of state for low initial porosity.

2.2.1.4 Grüneisen Parameter and the Speed of Sound:

For partial derivatives:

$$\frac{\partial P}{\partial v}\Big)_s = \frac{\partial P}{\partial v}\Big)_e + \frac{\partial P}{\partial e}\Big)_v \frac{\partial e}{\partial v}\Big)_s \tag{2.30}$$

Where the Mie-Grüneisen equation of state:

$$\gamma = v\frac{\partial P}{\partial e}\Big)_v \tag{2.18}$$

from

$$de = Tds - Pdv\,, \qquad -P = \frac{\partial e}{\partial v}\Big)_s \tag{2.31}$$

For partial derivatives:

$$\frac{\partial P}{\partial v}\Big)_H = \frac{\partial P}{\partial v}\Big)_e + \frac{\partial P}{\partial e}\Big)_v \frac{\partial e}{\partial v}\Big)_H \tag{2.32}$$

or

$$\frac{\partial P}{\partial v}\Big)_e = \frac{\partial P}{\partial v}\Big)_H - \frac{\partial P}{\partial e}\Big)_v \frac{\partial e}{\partial v}\Big)_H$$

Then

$$\frac{\partial P}{\partial v}\Big)_s = \frac{\partial P}{\partial v}\Big)_H + \frac{\partial P}{\partial e}\Big)_v \left(\frac{\partial e}{\partial v}\Big)_s - \frac{\partial e}{\partial v}\Big)_H\right) \tag{2.33}$$

Since the speed of sound, c, is

$$c = \sqrt{\frac{\partial P}{\partial \rho}\Big)_s} \tag{2.34}$$

Then

$$\rho = \frac{1}{v}, \qquad \partial\rho = -\frac{\partial P}{v^2}, \qquad c = \sqrt{-v^2\frac{\partial P}{\partial v}\Big)_s} \tag{2.35}$$

And the speed of sound equals

$$c = \sqrt{-v^2\left(\frac{\partial P}{\partial v}\Big)_H + \frac{\partial P}{\partial e}\Big)_v \left(\frac{\partial e}{\partial v}\Big)_s - \frac{\partial e}{\partial v}\Big)_H\right)\right)} \tag{2.36}$$

and for the Mie-Grüneisen equation of state

$$c = \sqrt{-v^2\left(\frac{\partial P}{\partial v}\right)_H + \frac{\gamma}{v}\left(-P - \frac{\partial e}{\partial v}\right)_H\Bigg)}$$

If a linear u_s-u_p fit is used for the Hugoniot curve

$$P = \frac{c^2(v_0 - v)}{\left(v_0 - s(v_0 - v)\right)^2} \tag{2.7}$$

$$\left(\frac{\partial P}{\partial v}\right)_H = -c^2\left(\frac{\left(v_0 + s(v_0 - v)\right)}{\left(v_0 - s(v_0 - v)\right)^3}\right) \tag{2.37}$$

and

$$e = \frac{1}{2}\frac{c(v_0 - v)^2}{\left(v_0 - s(v_0 - v)\right)^2} \tag{2.38}$$

$$\left(\frac{\partial e}{\partial v}\right)_H = -c(v_0 - v)\left(\frac{v_0}{\left(v_0 - s(v_0 - v)\right)^3}\right) \tag{2.39}$$

Rarefaction waves, which reduce the pressure on shocked materials, travel at the local speed of sound. The speed of sound changes depending upon the state of the material. By using equation 2.36 the relationship between the Mie-Grüneisen gamma and the state could be determined by studying the release wave.

2.2.1.5 Grüneisen Parameter and Temperature Calculations: The Mie-Grüneisen equation of state can be used to calculate the temperature of the shocked states, see Ref. (5).

From thermodynamics:

$$de = Tds - Pdv \tag{2.16}$$

$$ds = \frac{\partial s}{\partial T}\Big)_v dT + \frac{\partial s}{\partial v}\Big)_T dv \tag{2.40}$$

Since: $s = f(T, v)$

Then:

$$Tds = T\frac{\partial s}{\partial T}\Big)_v dT + T\frac{\partial s}{\partial v}\Big)_T dV \tag{2.41}$$

From the definition of the specific heat:

$$c_v = \frac{\partial e}{\partial T}\Big)_v = T\frac{\partial s}{\partial T}\Big)_v \tag{2.42}$$

and from the Maxwell relations:

$$\frac{\partial P}{\partial T}\Big)_v = \frac{\partial s}{\partial v}\Big)_T \tag{2.43}$$

then:

$$Tds = c_v dT + T\frac{\partial P}{\partial T}\Big)_v dv \tag{2.44}$$

Using the Mie-Grüneisen equation of state, the value of $\frac{\partial P}{\partial T}\Big)_v$ can be expressed by:

$$\frac{\partial P}{\partial T}\Big)_v = \frac{\partial P}{\partial e}\Big)_v \frac{\partial e}{\partial T}\Big)_v = \frac{\gamma}{v} c_v \tag{2.45}$$

Using equations 2.45 and 2.44 in equation 2.16:

$$de = c_V dT + T\frac{\gamma}{v} dv - Pdv \tag{2.46}$$

By restricting the differentials to a path along the Hugoniot curve:

$$\left.\frac{\partial e}{\partial v}\right)_H = c_v \left.\frac{\partial T}{\partial v}\right)_H + c_v \frac{\gamma}{v} T - P \tag{2.47}$$

For a shock process, equation 2.4 applies

$$\Delta e = \tfrac{1}{2}(P + P_o)(v_o - v) \tag{2.4}$$

The change in energy along the Hugoniot curve is then:

$$\left.\frac{\partial e}{\partial v}\right)_H = \tfrac{1}{2}\left.\frac{\partial P}{\partial v}\right)_H (v_o - v) - \tfrac{1}{2} P \tag{2.48}$$

Equating $\left.\frac{\partial e}{\partial v}\right)_H$ in equations 2.47 and 2.48:

$$c_v \left.\frac{\partial T}{\partial v}\right)_H + \frac{\gamma}{v} T c_v = \tfrac{1}{2}\left.\frac{\partial P}{\partial v}\right)_H (v_o - v) + \tfrac{1}{2} P \tag{2.49}$$

This is a differential equation of the form:

$$Ay' + By = f(v) \tag{2.50}$$

The value of $\left.\frac{\partial P}{\partial v}\right)_H$ can be determined from the equation of state and the Rankine-Hugoniot relationships developed earlier. The solution, which Meyers has solved is:

$$T = T_o e^{\frac{\gamma}{v}(v_o - v)} + \frac{(v_o - v)}{2c_v} P + \frac{e^{\frac{\gamma}{v}v}}{2c_v} \int_{v_o}^{v} P e^{\frac{\gamma}{v}v} \left(2 - \frac{\gamma}{v}(v_o - v)\right) dv \tag{2.51}$$

This equation must be numerically integrated.

The temperature within the material decreases as the material undergoes an isentropic release. For this situation, equation 2.44 becomes:

$$Tds = c_v dT + T\frac{\gamma}{v}c_v dv$$

For an isentropic process ds = 0 or:

$$T\frac{\gamma}{v}c_v dv = -c_v dT$$

$$\frac{dT}{T} = -\frac{\gamma}{v}dv \qquad (2.52)$$

Solving equation 2.52, with $\frac{\gamma}{v} = \frac{\gamma_o}{v_o}$ = a constant

$$T_2 = T_1 e^{\frac{\gamma_o}{v_o}(v_1 - v_2)} \qquad (2.53)$$

where:

subscript o is for the undisturbed material

subscript 1 is for the shocked material

subscript 2 is for the released state

2.2.1.6 Grüneisen Parameter and Specific Heat Relations: Coperthwaite Ref. (18) studied the Mie-Grüneisen gamma in relation to the specific heat at constant volume. From the definition of specific heat at constant volume:

$$c_v = \frac{\partial e}{\partial T}\Big)_v \qquad (2.42)$$

With the Maxwell relationship

$$T = \frac{\partial e}{\partial s}\Big)_v \qquad (2.54)$$

equation 2.42 becomes

$$c_v = T\frac{\partial s}{\partial T}\Big)_v \tag{2.55}$$

Taking the derivative with respect to volume at constant temperature:

$$\frac{\partial c_v}{\partial v}\Big)_T = \frac{\partial}{\partial v}\left(T\frac{\partial s}{\partial T}\Big)_v\right)_T \tag{2.56}$$

Using the Maxwell Relationships

$$\frac{\partial s}{\partial v}\Big)_T = \frac{\partial P}{\partial T}\Big)_v \tag{2.43}$$

Then

$$\frac{\partial c_v}{\partial v}\Big)_T = T\frac{\partial^2 P}{\partial T^2}\Big)_v \tag{2.57}$$

For a constant specific heat at constant volume

$$\frac{\partial P}{\partial T}\Big) = f(v) \tag{2.58}$$

For a constant specific heat at constant volume the above equation will have an equation of state for pressure, volume, and temperature with the general form:

$$P = f(v)T + g(v) \tag{2.59}$$

The equation of state for energy, pressure, and volume is obtained from manipulation of equation 2.58:

$$\partial P = f(v)\partial T \tag{2.60}$$

Then:

$$\left.\frac{\partial e}{\partial p}\right)_v = \frac{c_v}{f(v)} \tag{2.61}$$

Integration yields:

$$e = \left[\frac{c_v}{f(v)}\right] P + g'(v) \tag{2.62}$$

The assumption of a constant c_v is equivalent to the assumption made in the Mie-Grüneisen equation of state assumption that the value of $\left.\frac{\partial P}{\partial e}\right)_v$ is a function of volume only. Specific heat at constant volume varies with temperature. Kormer et al., Ref (19), and Krupnikov et. al., Ref. (9), have studied variable specific heat equations of state in relation to the Grüneisen parameter.

From the development of the Mie-Grüneisen equation of state it is shown that the value of $\left.\frac{\partial P}{\partial e}\right)_v$ is required for an accurate representation of more than the pressure of higher energy state off the Hugoniot curve. This value is required for the determination of the speed of sound and the temperature of shocked states.

Zharkov and Kalemin have suggested tungsten as an ideal material in which to study the energy dependence of the Grüneisen gamma because of the very high melting point, Ref. (15). They also report the value of the Mie-Grüneisen gamma for a ideal electron Fermi gas as equal to $^2/_3$.

2.2.1.7 The Constant Derivative Limitations Mie-Grüneisen Equation of State:

In the Mie-Grüneisen equation of state the value of $\frac{\gamma}{v}$ must increase with decreasing volumes for a constant γ. In order to increase the applicability of the equation of state the Constant Derivative Limitations Mie-Grüneisen equation of State uses Ref (20):

$$\left.\frac{\partial P}{\partial e}\right|_v = \frac{\gamma}{v_o} = \Gamma \tag{2.63}$$

The value of $\left.\frac{\partial P}{\partial e}\right|_v$ then remains constant. This reduces the increase seen in the Mie-Grüneisen equation of state but does not reflect the decreasing value of $\left.\frac{\partial P}{\partial e}\right|_v$ seen in experimentation.

The constant derivative Mie-Grüneisen equation of state also has a limiting volume. Following the earlier development the limiting volume would be:

$$v = v_{oo} - \frac{2v_o}{(\Gamma)} \tag{2.64}$$

For the constant derivative equation of state the pressure of the porous material can be determined, in the same manner as equation 2.20.

$$P = \frac{\left[1 - \frac{\Gamma}{2}(v_o - v)\right] c^2 (v_o - v)}{\left[1 - \frac{\Gamma}{2}(v_{oo} - v)\right] \left[v_o - s(v_o - v)\right]^2} \tag{2.65}$$

2.2.1.8 The Oh and Persson Equation of State for Porous Materials: This equation of state uses the approximate relationship that the change in energy with volume is equal along states of constant pressures and along the Hugoniot curve, Ref. (21),(22),(23).

$$\left.\frac{\partial e}{\partial v}\right|_p \approx \left.\frac{\partial e}{\partial v}\right|_H \tag{2.66}$$

Utilizing thermodynamics, shock physics, and equation 2.66, Oh and Persson developed a new relationship for γ:

$$\gamma(e) = v\left.\frac{\partial P}{\partial e}\right|_v = v\frac{c+(s-1)\sqrt{2e}}{c+s\sqrt{2e}}\frac{c}{\sqrt{2e}}\frac{c+2s\sqrt{2e}}{2c+s\sqrt{2e}} \tag{2.67}$$

This introduces a variable relationship between γ and energy, which is known to exist. The formulation was empirically modified to better fit experimental data and to match the low energy states:

$$\gamma(v,e) = v\left.\frac{\partial P}{\partial e}\right|_v = v\frac{c}{\sqrt{2e+\left(\frac{c}{2\gamma_o}\frac{v_o}{v}\right)^2}}\frac{c+2s\sqrt{2e}}{2c+s\sqrt{2e}} \tag{2.68}$$

The pressure of the initially porous material is given by:

$$P_{por}(V) = P_H(V) + \frac{1}{V}\int_{e_H}^{e_{por}} \gamma(V,E)de \tag{2.69}$$

Equations 2.68 and 2.69 are the Oh and Persson equation of state for completely compacted initially porous metals that have undergone shock compaction. Oh and Persson's model has been used to compute the Hugoniot curves of several metals, Figures 13, 14, 15. These plots use Oh and Persson's incomplete compaction equation, covered later, in addition to the modified gamma formulation. This affects only the lowest pressure portion of the curves. The equation of state performs well, even though the

approximation that $\left.\frac{\partial e}{\partial v}\right|_p \approx \left.\frac{\partial e}{\partial v}\right|_H$ and the possible changes in structure (state and crystal structure) are ignored.

Oh's gamma function at zero energy is equal to γ_o, the value of the Grüneisen parameter at ambient conditions. The value obtained from equation 2.28 should be utilized to determine this value. The values obtained from shock experimentation are from low initial porosities, and therefore low energies, and will closely match this value.

Johnson's review, Ref. (23) of the equation of state was highly critical. He determined a loss of accuracy at high internal densities. Oh and Persson's original paper overstated the applicability and range of the equation of state, but the usefulness and accuracy can be seen in Figures 13, 14, 15. The Oh and Persson equation of state is particularly useful as a first approximation for the porous Hugoniot of metals where the only experimental data available is for the solid Hugoniot. The loss of accuracy at high initial densities can be anticipated from an equation of state that is not fitted to a particular data set. The equation has introduced an energy term into the relationship which can reasonably be expected.

2.2.2 Partially Compressed Relationships

Equations of state for the partially densified regions can be divided into two general types, rate independent and rate dependent equations of state. The shock processes are assumed to be instantaneous changes in state. The rate dependent equations of state, while successful in computer models that spread the shock wave over several cells, do not reflect this physical model. These equations have been used successfully in modeling the release isentrope of both completely and incompletely densified materials. The rate independent forms do not reflect a possible increase in porosity in the release process, although breakup can occur.

2.2.2.1 Partially Compressed Region Rate Independent Forms:

2.2.2.1.1 Snow-Plow Model: In studies that assume complete compression of the initially porous material and negligible internal strength, the snow plow model has been applied, Ref. (5). In this model the material is assumed to compress without resistance to the specific volume of the solid and then follow the Hugoniot curve of the solid material. This model cannot be utilized for very porous materials because of the large internal energy differences, or for materials with any appreciable strength. It was an early approximation and is no longer utilized.

2.2.2.1.2 Herman's P-α Model: In 1969 Herman proposed the P-α theory, Ref. (24), to account for the plastic portion of the porous Hugoniot curve. In this theory porosity is defined as:

$$\alpha = \frac{v}{v_s}$$

where: α = porosity
v = specific volume
v_s = the specific volume of the solid at the same pressure and temperature (2.70)

The equation of state for a solid material is:

$$P = f(v_s, e) \tag{2.71}$$

The equation of state for the porous material is then

$$P = f\left(\frac{v_s}{\alpha}, e\right)$$

and (2.73)

$$\alpha = g(P, e)$$

Since the pressure and energy are related along the Hugoniot curve, the porosity can be simplified as:

$$\alpha = g(v_s, e) \tag{2.74}$$

Herman then proposed a polynomial fit for the plastic region:

$$\alpha = \alpha_0 + \alpha_1 P + \alpha_2 P^2 + \alpha_3 P^3 + \ldots \tag{2.75}$$

A cubic form was used to fit experimental data. The Mie-Grüneisen equation of state was used to account for the energy differences experienced in porous compression.

The P-α equation of state thermodynamically and physically describes the process of porous compression within the plastic region. This equation of state, with modifications, became a basis for much of the following work.

2.2.2.1.3 Boades Exponential P-α Model: Boade suggested an exponential P-α model: Ref. (25)

$$\alpha_2 = 1 + (\alpha_1 - 1)e^{\hat{a}(P_2 - P_1)} \tag{2.76}$$

where: $\alpha_1 = \frac{v_P}{v_s}$ at pressure P_1

$\alpha_2 = \frac{v_P}{v_s}$ at pressure P_2

$\hat{a}$ = adjustible variable

v_p = the specific volume of the porous material

2.2.2.1.4 Oh and Persson's Incomplete Compaction: In examining Boades' results, Oh and Persson investigated possible theoretical bases for the success of Boade's exponential P-α model, Ref. (26). Rewriting equation 2.76:

$$P = \left(P_1 + \frac{1}{\hat{a}} \ln(v_1 - v_{s1}) + \frac{1}{\hat{a}} \ln\left(\frac{v_s}{v_{s1}}\right)\right) + \frac{1}{\hat{a}} \ln\left(\frac{1}{v - v_{s1}}\right) \tag{2.77}$$

where: v_{S1}= the specific volume of the solid portion

subscript 1, values at state 1, the elastic limit for the initially porous material.

They assumed that during the plastic deformation the increase in strength due to work hardening is approximately equal to the decrease in strength due to deformation heating. This allowed the utilization of green compaction to the problem Ref. (26). Using James' linear fit to the Meyer work hardening index:

$$\hat{a} = 5n - 9.4$$

where: n is the Meyer work hardening index

$$W = \text{constant}\left(\frac{d}{D}\right)^n$$

W = the applied load in a hardness test

D = ball diameter

d = diameter of the impression

With the approximation that $v_1 \approx v_\infty$ (the initial porous volume) and $v_{s1} \approx v_o$ (the solid volume at zero pressure):

$$P \approx \sigma_y + \log\left(\frac{v_\infty}{v_o} - 1\right) + \frac{1}{\hat{a}}\log\left(\frac{v_s}{v - v_s}\right) \qquad (2.78)$$

where: σ_y = yield strength

which can be rewritten as:

$$v = v_s(P)\left[1 + \left(\frac{v_\infty}{v_o} - 1\right)e^{-(5n-9.4)(P-\sigma_y)}\right] \qquad (2.79)$$

Where: $v_s(P)$ = the specific volume of the solid material absent the voids at a given pressure

For low pressures the volume of the solid portion of the material, $v_s(P)$, can be approximated by the solid specific volume, at zero pressure. As the pressure increases, the decreasing volume of the solid portion must be accurately reflected. This equation of

state has successfully been applied to a variety of metals. It has the advantage of providing the incomplete compaction Hugoniot curves of materials without prior experimentation. When reliable experimental data are available, Boade's exponential P-α equation of state will necessarily provide a better fit, as it is fitted to the data and has the same form as Oh's and Persson's equation.

2.2.2.2 Rate Dependent Forms:

2.2.2.2.1 Butcher's Rate Dependent Form: Rate dependent pore collapse models have also been used to describe the pore collapse in porous materials. Butcher, studying 80% dense polyurethane suggested a model of: Ref. (27)

$$\dot{\alpha} = \dot{\alpha}_e + \dot{\alpha}_p \tag{2.80}$$

where: $\dot{\alpha}_e$ = the time rate of change of the recoverable (elastic) porosity
$\dot{\alpha}_p$ = *the* time rate of change of the plastic porosity

α_e is given by:

$$\begin{aligned} &\dot{\alpha}_e = M\dot{P} \\ &M = \frac{d\alpha_e}{dP} = \frac{\alpha}{\rho_{so} c_o^2}\left[1 - \frac{\alpha}{h(\alpha)}\right] \\ &h(\alpha) = a\alpha + [1 - a] \\ &a = \frac{c_e - c_o}{c_o[\alpha_o - 1]} \end{aligned} \tag{2.81}$$

$\dot{\alpha}_p$ is then given by:

$$\dot{\alpha} = M(\alpha)\left\{\dot{P}_i + \frac{1}{\tau_o}\left[P - P_{eq}(\alpha)\right]\right\} \tag{2.82}$$

where:

$\dot{P}_i = \frac{dP_i}{dt}$ P_i = instantaeous stress rate if entire deformation were elastic

$M(\alpha)$ a function of the elastic change in porosity

P_{eq} = an equilibrium pressure

c_0 = initial solid speed of sound

c_e = elastic wave velocity

ρ_{so} = initial density of the solid matrix

τ_0 = relaxation time

Butcher concluded that this was an oversimplification of the pore collapse process.

2.2.2.2.2 Carrol and Holts Spherical Pore Collapse Model: Carrol and Holt, Ref. (28), expanded on Butcher's work. They assumed a sphere of material, outer radius b, with a spherical pore of average diameter a. The initial porosity α_o is then:

$$\left(\frac{b_o}{a_o}\right)^3 = \frac{\alpha_o}{(\alpha_o - 1)} \tag{2.83}$$

The porosity is then given by:

$$\alpha = \frac{b^3}{\left(b^3 - a^3\right)} \tag{2.84}$$

The dynamic pore collapse relation is given as:

$$\tau^2 Y Q(\ddot{\alpha}, \dot{\alpha}, \alpha) = P - P_{eq}(\alpha) \tag{2.85}$$

where: Y is the yield strength

τ is a material time constant $\quad \tau = \frac{\rho a_o^2}{3Y(\alpha_o - 1)^{2/3}}$ (2.86)

Q is a function defined as

$$Q(\ddot{\alpha},\dot{\alpha},\alpha)=-\ddot{\alpha}\left[(\alpha-1)^{-1/3}-\alpha^{-1/3}\right]+\frac{1}{6}\dot{\alpha}^2\left[(\alpha-1)^{-4/3}-\alpha^{-4/3}\right] \qquad (2.87)$$

P_{eq} is the equilibrium pressure from static pore collapse relation

$$P_{eq}=\begin{cases}\dfrac{4G(\alpha_o-\alpha)}{3\alpha(\alpha-1)} & (\alpha_o\geq\alpha\geq\alpha_1)\\ \dfrac{2}{3}Y\left(1-\dfrac{[2G(\alpha_0-\alpha)]}{Y\alpha}\right)+ln\left(\dfrac{2G(\alpha_0-\alpha)}{Y(\alpha-1)}\right) & (\alpha_1\geq\alpha\geq\alpha_2)\\ \dfrac{2}{3}Y\,ln\left(\dfrac{\alpha}{(\alpha-1)}\right) & (\alpha_1\geq\alpha\geq 1)\end{cases} \qquad (2.88)$$

where G is the shear modulus

Equation 2.85 is simplified by assuming constant porosity during the elastic and elastic plastic phases, up to a critical pressure. The porosity is then changed only in the plastic pore collapse phase.

$$\tau^2YQ(\ddot{\alpha},\dot{\alpha},\alpha)=P-\frac{2}{3}Y\,ln\left(\frac{\alpha}{\alpha-1}\right) \qquad (P_{crit}\leq P\leq\infty) \quad (2.89)$$

where:

$$P_{crit}=\frac{2}{3}Y\,ln\left(\frac{\alpha_o}{\alpha_o-1}\right) \qquad (2.90)$$

2.2.2.2.3 TEPLA-F Model: Johnson and Addessio Ref. (29)(30) have developed the TEPLA-F rate dependent equation of state for porosity. This model has been used for both porous compaction and to track the porosity that can occur during a release process.

In the TEPLA-F equation of state the pressure in the solid portion of the matrix is calculated separately. The pressure of the material is then:

$$P(\rho, e, \omega) = \omega P_S(\rho_S, e_s)$$

where:

ω = the material solidity = 1 - ϕ (2.91)

ϕ = porosity = $\dfrac{\text{void volume}}{\text{total volume}}$

subscript s is for the solid portion of the material

The equation of state is defined in differential form as:

$$dP' = P_{v'}\, dv' + P'_{e'}\, de'$$
$$dT' = Q_{v'}\, dv' + Q_{e'}\, de'$$
$$de' = T'\, ds' - pv'$$

where: ' signifies the solid portion of the material

s = entropy

T' = temperature, the temperature of the porous material is assumed equal to

the porous material is assumed equal to the temperature of the solid

p = pressure

P = function of v' and e' yielding pressure

Q = function of v' and e' yielding temperature

v = volume

with:

$$B' = -v'\left(\frac{\partial p'}{\partial v'}\right)_s \qquad (2.92)$$

Gurson, Ref. (31), studied ductile failure in metals at stresses lower than those experienced in shock wave interactions. Johnson and Addessio applied this methodology to high strain rates. This paper, Ref. (32), shows some developments in the rate of change of porosity with pressure. For this equation of state the rate of change in porosity is:

$$\dot{\phi} = (1-\phi)\dot{\varepsilon}^{p}_{kk}$$

where:

$$\phi = \text{ porosity} = \frac{\text{void volume}}{\text{total volume}} \qquad (2.93)$$

ε = the volumetric contribution to plastic strain

In this equation of state the pressure in the solid portion of the matrix is calculated separately. The model assumes that some porosity is always present, or the (1-ϕ) becomes zero and the strain becomes infinite. The pressure of the material is then:

$$P(\rho,e,\omega) = \omega\, P_S(\rho_S, e_s)$$

where:

ω = The material solidity = 1 - ϕ (2.94)

Subscript s is for the solid portion of the material

Using the Mie-Grüneisen equation of state and the shock Hugoniot equations in the above equation;

$$\dot{P} = \Gamma_s s_{ij}\dot{e}_{ij} - B\dot{\varepsilon}_{kk} + \alpha\dot{\varepsilon}^{kk}_{ij}$$

where:

B = the bulk modulus of elastisity of the macroscopic material (2.95)

α = B - $(1+\Gamma)P$

Γ = the Gruneisen parameter

The plastic strain is :

$$\dot{\varepsilon}_{ij}^{p} = \frac{1}{3\tau_r}\left(\sigma_{ij} - \sigma_{ij}^{eq}\right)$$

where:

τ_r = a rate sensitive parameter with units of times (2.96)

σ_{ij}^{eq} = equilibrium stress, a projection of the current stress state, σ_{ij}^{eq}, onto a yield surface

The volumetric and deviatoric plastic strain rates are obtained from:

$$\dot{\varepsilon}_{kk}^{p} = -\frac{1}{\tau_r}\left(P - P^{eq}\right) \tag{2.97}$$

and $$\dot{e}_{ij}^{p} = \frac{1}{\tau\tau_r}\left(\tau - \tau^{eq}\right)s_{ij} \tag{2.98}$$

The equilibrium stress is the scaled material stress to the yield surface:

$$s_{ij}^{eq} = \frac{\tau^{eq}}{\tau}s_{ij} \tag{2.99}$$

Substitution of equations 2.93 into 2.97 yields

$$\dot{\phi} = -\frac{1}{\tau_r}(1-\phi)\left(P - P^{eq}\right) \tag{2.100}$$

The version used in the CALE Code presented later in this work was modified to some degree from the above developments, Ref. (33). For this case:

$$b = \rho\left(\frac{\partial p}{\partial \rho}\right)_s \tag{2.101}$$

$$\dot{\phi} = -\frac{P - P_c}{b - P}\frac{1}{1-\phi} + \frac{P_{min}}{\phi} \qquad \text{for compression} \tag{2.102}$$

where: P_{min}= minimum pressure used in the computation

P_c= compaction pressure, pressure at which the voids begin to be squeezed out, $P_c = -P_{min}\ln(\phi)$

For materials in tension with increasing porosity the rate of change of porosity equation is modified to:

$$\dot{\phi} = -\frac{P + P_c}{b - P}(1 - \phi) \tag{2.103}$$

$$\dot{\phi} = -\frac{1}{\tau_r}(1 - \phi)(P - P^{eq}) \tag{2.104}$$

The rate dependent forms of the porous equation of state are a simplification of the pore collapse process. Optical micrographs by Wright, Flinn, and Korth, Ref. (34) of explosively compacted 304 stainless steel and Staudhammer and Murr's, Ref. (35), study of compacted tungsten and 304 stainless steel rods show a much more complex phenomenon. These reports show that the compaction is not of spherical voids in a matrix. The void collapse is not uniform. The material collapses in the direction of the shock wave. Localized jetting and melting occurs.

The rate independent forms of the porous equation of state, on the other hand, ignore the time required for the pores to collapse. Equilibrium of the shocked material is assumed to be instantaneous. For most materials with extremely small pore sizes the time for the material to reach equilibrium is very short. The rate independent forms also ignore the inhomogeneities caused by local heating and melting. It is not feasible to model most porous materials with each pore represented in the mesh. The approximations from the rate independent or the rate dependent methods must be accepted.

2.3 Gurney Method for Estimating the Velocity of Metal Driven by a Detonation

In a shaped charge the explosive drives the walls of the liner to a higher velocity than the initial particle velocity due to the shock wave. This is caused by the acceleration of the liner by the detonation products between the time the detonation wave impacts the liner and the collapse of the liner.

R.W. Gurney, Ref. (36)(37) developed a method for determining the velocity of metal fragments created by a detonation. This method is rather simplistic, but the results obtained correlate well with experiments. The model assumes a linear velocity distribution throughout the reacted gases, and a constant velocity within the wall.

Gurney's assumption creates a partitioning of the available kinetic energy between the gases and the wall. For an explosive driving a plate, Figure 16, the energy available to move material is from the chemical reaction, E. The mass of the explosive and its detonation gases, is defined by the variable C, and the mass of the metal plate is M. For a differential mass m:

$$CE = \int \tfrac{1}{2} mV^2 dy_{gasses} + \int \tfrac{1}{2} mV^2 dy_{metal} \qquad (2.105)$$

Where: V = The material velocity

For a uniform plate velocity

$$\int \tfrac{1}{2} mV^2 dy_{metal} = \tfrac{1}{2} MV^2 \qquad (2.106)$$

A linear velocity distribution is assumed for the detonation gasses. The gasses at the wall are moving with the metal at a velocity of V. The gasses on the free surface are moving

with a velocity of V_{gasses}. This yields a velocity distribution of:

$$V_{gasses} = (V_o + V)\frac{y}{y_o} - V \tag{2.107}$$

then

$$\int \tfrac{1}{2} m V^2 dy_{gasses} = \tfrac{1}{2}\int_{y=0}^{y=y_o}\left(\rho_{explosive}\left((V_o + V)\frac{y}{y_o} - V\right)^2\right)dy \tag{2.108}$$

then the conservation of energy yields:

$$CE = \tfrac{1}{2}\int_{y=0}^{y=y_o}\left(\rho_{explosive}\left((V_o + V)\frac{y}{y_o} - V\right)^2\right)dy + \tfrac{1}{2}MV^2$$

$$y_o\rho_{explosive}\left(\tfrac{1}{3}(V_o + V)^2 - (V_o + V)V + V^2\right) + MV^2 = 2CE$$

$$C\left(\tfrac{1}{3}(V_o + V)^2 - (V_o + V)V + V^2\right) + MV^2 = 2CE \tag{2.109}$$

$$\left(\tfrac{1}{3}(V_o + V)^2 - (V_o + V)V + V^2\right) + \frac{M}{C}V^2 = 2E$$

The conservation of momentum requires that:

$$MV = \rho_{explosive}\int_{y=0}^{y=y_o}\left((V_o + V)\frac{y}{y_o} - V\right)dy$$

$$MV = \rho_{explosive}y_o\left((V_o + V)\frac{1}{2} - V\right) = C\left((V_o + V)\frac{1}{2} - V\right) \tag{2.110}$$

from which

$$2V\left(1 + \frac{M}{C}\right) = (V_0 + V) \tag{2.111}$$

then:

$$\frac{V}{\sqrt{2E}} = \left(\frac{3}{1 + 5\frac{M}{C} + 4\left(\frac{M}{C}\right)^2} \right)^{\frac{1}{2}} \qquad (2.112)$$

The Gurney constant, $\sqrt{2E}$, is determined experimentally from a cylinder test at an expansion ratio of seven times the initial value, Ref. (38). This is a point where the metal wall has approximately achieved its maximum velocity and the cylinder wall has not yet fragmented. The same method has been applied to a variety of geometies, cylinders, sandwiched plates, spheres, etc.

2.4 Shaped Charges

There is a variety of methods for concentrating the energy available from detonations. A common method is through the use of the Monroe or hollow cavity effect. Increased efficiency is obtained if the cavity is lined with some non-reacting material. The arrangement is called a shaped charge. A variety of cavity shapes have been used, but conical liners are covered here. A typical shaped charge has the configuration shown in Figure 17.

2.4.1 Shaped Charge Jet Formation

The detonation wave travels from the detonator of the charge down. As it travels it collapses the liner onto itself. The collapse point, where the liner material meets, also travels down the charge. The material entering the collapse point divides and forms two masses: the leading and faster moving jet and the slower slug. A typical collapse is shown in Figure. 18

For the analysis of the collapse process, the velocity of the collapsing walls must be known. The Gurney method, covered in section 2.3, predicts the wall velocities accurately, except during the initial acceleration portion. Typical models approximate this acceleration with a variety of approximations. The amount of explosive interacting with the copper wall changes (decreases) as the detonation moves down the charge. Problems of this type were studied by Pugh, Eichelberger, and Rostoker in 1952, leading to the PER theory, Ref. (39)(40). This is a variation of the earlier Birkoff et. al. theory, which had a constant collapsing wall velocity.

For the present development, the details of the initial acceleration of the liner will be ignored. With this approximation, and the geometry in Figures 18 and 19, the relationship between the angle, θ, and the collapsing wall velocity is:

$$\sin(\theta) = \frac{V_o}{2U} \tag{2.113}$$

The vector relationship, Figure 20,at the moving junction from the law of sines

$$V = \frac{\cos(\beta + \alpha)}{\sin(\beta)} \tag{2.114}$$

the collapse point velocity is:

$$V_1 = \frac{V_o \cos(\beta - \alpha - \theta)}{\sin(\beta)} \tag{2.115}$$

An incompressible flow approximation is used in this analysis. This approximation works well if the liner material does not undergo supersonic flow. The internal strength of the material can be ignored at these extreme pressures. A coordinate system moving with the collapse point is used to simplify the problem. Under these conditions the material flows straight into the collapse point, as shown in Figure 21.

The first conservation equation can now be applied to the problem. The first equation applied is the Bernoulli equation. For this problem, this reduces to:

$$P + \tfrac{1}{2}\rho_o V^2 = \text{constant} \tag{2.116}$$

For this condition the liner is unconfined, and the pressure remains constant. The liner material moves, in this coordinate system, at equal speed into the collapse point, into the

jet, and into the slug. The influx angle determines how large a fraction of the liner mass will flow into each. Using the sign conventions for velocity:

$$V = V_j = -V_s \tag{2.117}$$

In the fixed coordinate system:

$$V_j = V_l + V \tag{2.118}$$

and

$$V_s = V_l - V \tag{2.119}$$

Using equations 2.118 and 2.119 in equations 2.115 and 2.116

$$V_j = V_o \, csc\left(\frac{\beta}{2}\right) cos\left(\alpha + \theta - \frac{\beta}{2}\right) \tag{2.120}$$

and

$$V_s = V_o \, sec\left(\frac{\beta}{2}\right) cos\left(\alpha + \theta - \frac{\beta}{2}\right) \tag{2.121}$$

equation 2.113 can now be used to eliminate the angle θ in equations 2.120 and 2.121.

$$V_j = V_o \, csc\left(\frac{\beta}{2}\right) cos\left(\alpha - \frac{\beta}{2} + sin^{-1}\left(\frac{V_o}{2U}\right)\right) \tag{2.122}$$

$$V_s = V_o \, sec\left(\frac{\beta}{2}\right) cos\left(\alpha - \frac{\beta}{2} + sin^{-1}\left(\frac{V_o}{2U}\right)\right) \tag{2.123}$$

The mass of the liner, m, entering the jet, m_j, and the slug, m_S, can now be investigated. By applying the conservation of mass:

$$dm = dm_j + dm_s \tag{2.124}$$

From the conservation of momentum, along the x-axis

$$-\mathrm{dm}\,V\,cos(\beta) = \mathrm{dm}_j V_j + \mathrm{dm}_s V_s \tag{2.125}$$

From equation 2.117

$$V = V_j = -V_s \tag{2.126}$$

$$\mathrm{dm}\,cos(\beta) = \mathrm{dm}_s - \mathrm{dm}_j \tag{2.127}$$

using equation 2.125 and equation 2.126

$$\frac{\mathrm{dm}_j}{\mathrm{dm}} = sin^2\left(\frac{\beta}{2}\right) \tag{2.128}$$

and

$$\frac{\mathrm{dm}_s}{\mathrm{dm}} = cos^2\left(\frac{\beta}{2}\right) \tag{2.129}$$

From Figure 22 it can be seen that the angle β is not convenient to calculate. The angle is depended upon the variations in the liner contour. The angle β^+, Figure 22, would be much more amenable to computations, as it is independent of contour.

The PER theory uses cylindrical coordinates of the point M (r,z) and the coordinates of P' (X tan A, X). Using the collapse velocity of the wall and the geometry in Figure 21, the time since the detonation has passed a point (elapsed time from the start of motion), t:

$$Z = X + V_o(t - T)sin(A) \tag{2.130}$$

Where: Z = the axial coordinate

r = the radial coordinate

and

$$r = X\,tan(\alpha) - V_o(t - T)cos(A) \tag{2.131}$$

where:

t = elapsed time from start of motion

$$T = \frac{X}{D} = \frac{X}{U\,cos(\alpha)}$$

$$A = \alpha + \theta$$

The time at which the point reaches the axis, the collapse point, is determined by setting r = 0 in equation 2.131.

$$t - T = X\,tan(\alpha) \tag{2.132}$$

By definition the slope is

$$\frac{dr}{dZ} = tan(\beta) \tag{2.133}$$

Using equations 2.130 and 2.131 to find $\frac{dr}{dZ}$, and equating to tan ß

$$tan(\beta) = \frac{sin(\alpha) + 2\,sin(\theta)cos(A) - X\,sin(\alpha)\left(1 - tan(A)tan(\theta)\right)\frac{V_o'}{V_o}}{cos(\alpha) - 2\,sin(\theta)sin(A) + X\,sin(\alpha)\left(tan(A) + tan(\theta)\right)\frac{V_o'}{V_o}} \tag{2.134}$$

$$\text{where: } V_o' = \frac{V_o}{X} \quad V_o' = \frac{dV_o}{dX} \tag{2.135}$$

Equation 2.114 and the relationships $2\theta = \beta - \alpha$ and $2A = \beta^+ + \alpha$, (see Figures 23 and 24) are used to simplify equation 2.135.

$$tan(\beta) = \frac{sin(\beta^+) - X\, sin(\alpha)(1 - tan(A)tan(\theta))\frac{V_o'}{V_o}}{cos(\beta^+) + X\, sin(\alpha)(tan(A) + tan(\theta))\frac{V_o'}{V_o}} \qquad (2.136)$$

The above simplified theory provides an adequate understanding of shaped charge functioning. The model ignores compressibility effects and real material properties. Computational models have been used to account for these effects. Some codes use variations of the above development to create a quasi one dimensional code. This is possible because the equations allow for simple computations to be made in the radial directions in axisymmetic geometries. These codes do not predict the breakup of the shaped charge jet when the collapse velocity is above Mach 1.2, which has been determined experimentally to occur, Ref. (41).

2.4.2 Shaped Charge Jet Penetration

Shaped charge jets velocities vary along the length of the jet. This is a result of the larger amount of explosives surrounding the tip of the liner than other parts of the cone. This causes the regions closer to the tip to collapse faster and form a faster portion of the jet. The jet then stretches with time and distance. While this causes the jet to reduce in diameter, the longer jet causes a deeper penetration into the target. There is a limit to this effect, however, since the jet cannot stretch indefinitely and eventually breaks up. Walters and Zukas give an excellent description of the penetration process, Ref. (40).

The initial analysis of the penetration process will examine a jet, or rod, of uniform velocity, density, and constant length. As in the analysis for the formation of the jet, the internal strength of the material is neglected. For the rod in Figure 24 a coordinate system moving with the penetration is chosen.

For this problem steady state conditions are assumed to exist throughout the penetration. The pressure is then the pressure at the interface of the rod and the target. From Bernoulli's equation:

$$\tfrac{1}{2}\rho_j(V-U)^2 = \tfrac{1}{2}\rho_T U^2 \qquad (2.137)$$

It is assumed that there is no residual penetration after the rod is eroded away. The penetration, Φ, is then the penetration velocity times the time of penetration:

$$\Phi = U\frac{l}{(V-U)} \qquad (2.138)$$

By using equation 2.137 to solve for $\frac{U}{(V-U)}$ in equation 2.138:

$$\Phi = l\left(\frac{\rho_j}{\rho_T}\right)^{1/2} \qquad (2.139)$$

While this analysis is very simplistic, it provides a very useful relationship between penetration and the densities of the jet and the target. An interesting development in equation 2.139 is that it predicts that the penetration is independent of the velocity of the rod. Clearly this is possible if the interaction pressures are in the range where strength considerations can truly be neglected. From equation 2.139 another interesting derivation

is possible. Many materials of different density are available for the target. If weight is the only consideration in selecting a target to prevent complete penetration:

$$W = P(1 \text{ unit square})\,\rho_t \tag{2.140}$$

where: W = Weight per unit surface area at a thickness that just defeats penetration

For two target materials of different density, $\rho_1 > \rho_2$:

$$W_1 = P_1\rho_1 = l\left(\frac{\rho_j}{\rho_1}\right)^{1/2}\rho_1$$

and

$$W_2 = P_2\rho_2 = l\left(\frac{\rho_j}{\rho_2}\right)^{1/2}\rho_2 \tag{2.141}$$

the ratio of weights for material 1 and 2 is:

$$\frac{W_1}{W_2} = \sqrt{\frac{\rho_1}{\rho_2}} \tag{2.142}$$

Since ρ_1 is greater than ρ_2 the weight of material 1 to stop the penetration is greater than that of material 2. From this development it is seen that targets with higher densities stop the penetration in a shorter distance, but the same level of protection is obtained from a thicker and lighter layer of a lower density material.

A more complete and more accurate analysis has been made for variable velocity jets, Ref. (40). The jet is assumed to have a linear velocity profile, with a faster velocity at the tip. This assumption leads to a virtual origin. For this development the jet is at a point

along the axis at time zero. As the jet develops it stretches, with the tip moving at a constant velocity, and a linear velocity profile is established. With these assumptions the jet velocity at any point and time is determined by:

$$V(x,t) = \frac{V_{tip}}{V_{tip}t}x = \frac{x}{t} \tag{2.143}$$

and the position of the tip of the jet:

$$x_{tip} = V_{tip}t \tag{2.144}$$

The time required for the jet to reach the target is:

$$t_o = \frac{x_{s.o.}}{V_{tip}} \tag{2.145}$$

where:

V_{tip} = the tip velocity

$x_{s.o.}$ = the distance from the virtual origin to the target

t_o = the time required to reach the target

equation 2.137 is still applicable

$$\tfrac{1}{2}\rho_j(V-U)^2 = \tfrac{1}{2}\rho_T U^2 \tag{2.137}$$

Solving for the penetration velocity U:

$$\left(V - \left(1 + \left(\frac{\rho_T}{\rho_j}\right)^{1/2}\right)U\right)\left(V + \left(-1 + \left(\frac{\rho_T}{\rho_j}\right)^{1/2}\right)U\right) = 0 \tag{2.146}$$

$$U = \frac{V}{\left(1+\left(\frac{\rho_T}{\rho_j}\right)^{1/2}\right)} \tag{2.147}$$

The second root might be negative, which is not possible, this solution is discounted.

Equation 2.139 in differential form:

$$\frac{d\Phi}{dl} = \frac{U}{V-U} = -\left(\frac{\rho_T}{\rho_j}\right)^{-1/2} \tag{2.148}$$

The penetration depth, in terms of the impinging velocity and time, is:

$$\Phi(t) = tV(t) - x_{s.o.} \tag{2.149}$$

By definition:

$$U = \frac{d\Phi}{dt} \tag{2.150}$$

The differential relation between the jet velocity and penetration is:

$$U = \frac{d\Phi}{dt} = V + t\frac{dV}{dt} \tag{2.151}$$

Using equations 2.147 and 2.151 to eliminate the penetration velocity:

$$\frac{V}{\left(1+\left(\frac{\rho_T}{\rho_j}\right)^{1/2}\right)} = V + t\frac{dV}{dt}$$

$$V\left(\frac{1}{\left(1+\left(\frac{\rho_T}{\rho_j}\right)^{1/2}\right)}-1\right)=t\frac{dV}{dt} \tag{2.152}$$

setting $\left(\frac{\rho_T}{\rho_j}\right)^{1/2}=\Omega$

$$V\left(\frac{-\Omega}{1+\Omega}\right)=t\frac{dV}{dt} \tag{2.153}$$

Integrating both sides of equation 2.153

$$\int_{t_0}^{t}\frac{\left(\frac{-\Omega}{1+\Omega}\right)}{t}dt=\int_{V_{tip}}^{V}\frac{1}{V}dV \tag{2.154}$$

Then:

$$\left(\frac{-\Omega}{1+\Omega}\right)\ln\left(\frac{t}{t_o}\right)=\ln\left(\frac{V}{V_{tip}}\right) \tag{2.155}$$

Solving for the jet velocity:

$$V=V_{tip}\left(\frac{t_o}{t}\right)^{\left(\frac{\Omega}{1+\Omega}\right)} \tag{2.156}$$

equation 2.150 becomes:

$$\Phi(t)=V_{tip}t\left(\frac{t_o}{t}\right)^{\left(\frac{\Omega}{1+\Omega}\right)}-x_{s.o.} \tag{2.157}$$

This yields the penetration as a function of time. As the penetration progresses the velocity of the impinging jet decreases. At some point the pressures induced are so low that strength considerations of the target and jet materials become significant, and finally the penetration stops. These situations are approximated by choosing a cutoff velocity at which the penetration supposedly stops. This velocity is above the actual cutoff velocity in order to account for the effects of material strength. The total penetration then can be stated as:

$$\Phi = x_{s.o.}\left(\left(\frac{V_{tip}}{V_{tail}}\right)^{\frac{1}{\Omega}} - 1\right) \tag{2.158}$$

2.5. Computer Modeling of Shock Waves and Detonations

A method for computer modeling shock wave interactions was first proposed by Von Neumann and Richtmyer in 1950 Ref. (43). Their proposal was for a one dimensional model which was later incorporated in the highly successful SIN code,

Ref. (42). Modern computer codes for shock interactions, hydrocodes, model in two and three dimensions. Computers cannot model the materials as in a continuous form; instead, a mesh must be used. The material can either move through the mesh, Eulerian, or the mesh can move with the material, Lagrangian. For multiple materials, the Eulerian system must account for cells with mixed materials, but high strain rates are a problem. In Lagrangian codes, the cell can remain a pure material, but the cells can become severely distorted, causing a failure of the code.

In Lagrangian codes the differential conservation equations are, Ref. (5)(42):

Conservation of mass

$$\frac{D\rho}{Dt} + \rho\vec{\nabla}\vec{u} = 0 \tag{2.159}$$

Conservation of momentum

$$\frac{\rho D\vec{u}}{Dt} = -\vec{\nabla}P \tag{2.160}$$

Conservation of energy, for no chemical reactions

$$\frac{de}{dT} + P\frac{dv}{dt} = 0 \tag{2.161}$$

In Eulerian codes the differential conservation equations are, Ref. (5)(42):

Conservation of mass

$$\frac{\partial \rho}{\partial t} + \vec{\nabla}(\rho \vec{u}) = 0 \tag{2.162}$$

Conservation of momentum

$$\rho\left(\frac{\partial \vec{u}}{\partial t} + \vec{u}\vec{\nabla}\vec{u}\right) = -\vec{\nabla}P \tag{2.163}$$

Conservation of energy, for no chemical reactions

$$\frac{\partial}{\partial t}\left(e + \tfrac{1}{2}u^2\right)\rho + \vec{\nabla}\cdot\left(\rho\left(e + \tfrac{1}{2}\vec{u}^2\right)\vec{u} + P\vec{u}\right) = 0 \tag{2.164}$$

A relation Between Lagrangian and Eulerian Referentials

$$\left(\frac{D}{Dt}\right)_L = \left(\frac{\partial}{\partial t}\right)_e + \vec{u}\vec{\nabla} \tag{2.165}$$

In computer modeling these equations are rewritten as difference equations. The time step size becomes a critical factor in the accuracy of the model. The Courant condition, Ref. (31), is frequently used to determine the time step. The Courant condition is where the time step is less than the least time in the problem for a sound wave to completely cross a cell.

A mixed form of computer modeling, which allows for movement of the mesh and material through it, has been developed. These arbitrary Lagrange Eulerian (ALE) models allow the mesh to move with areas of interest, and avoid the extreme distortions of cells. The ALE codes have been successfully used in modeling shaped charges, with their relatively complex formation process.

Shock waves bring about instantaneous changes in state. For a finite difference the discontinuity cannot be modeled. In order to model the shock front, a concept of artificial viscosity is utilized. A viscous term is added that spreads the shock wave front over several cells. The more spread out the pressure wave, the less instability is exhibited in the pressure wave. If the wave is spread out too far, a poor representation of shock interactions is obtained.

A disadvantage of using artificial viscosity is the loss of energy caused by the model approximately integrating the Hugoniot curve for the energy. The actual energy in a shock process is one half the pressure times the change in volume.

For solid materials, this approximation is moderately accurate, and corrections are not frequently applied. For porous materials, with large change in volumes, this approximation is insufficient.

CHAPTER 3

NEW EQUATION OF STATE FOR THE SHOCK COMPACTION OF POROUS TUNGSTEN

In order to compute the properties of the shock compacted porous tungsten an improved equation of state was desired that had an improved comparison to the available data and did not require the numerical integration in the Oh and Persson equation of state. After the literature search, this process was started with a study of the behavior of the Oh and Persson equation of state.

3.1 An Investigation of the Behavior of the Oh and Persson Equation of State

At large energies the Oh and Persson gamma, equation 2.68

$$\gamma(v,e) = v\left.\frac{\partial P}{\partial e}\right|_v = v\frac{c}{\sqrt{2e+\left(\frac{c}{2\gamma_o}\frac{v_o}{v}\right)^2}}\frac{c+2s\sqrt{2e}}{2c+s\sqrt{2e}} \qquad (2.68)$$

asymptotes to

$$\gamma(\text{energy}\rightarrow\infty) = \frac{2c}{\sqrt{2e}} \qquad (3.1)$$

The value of gamma is then only a function of energy, and the parameters in the linear u_s u_p equation of state speed of sound.

Oh and Persson's gamma function has another critical volume at which the pressure reaches infinity. If the energy is assumed to be very large, equation 3.1 can be used for the gamma function in equation 2.18 and solved to:

$$P_{por}(v) = P_H(v) + \frac{1}{v}\int_{E_H}^{E_{por}} \gamma(v,e)de = P_H(v) + \frac{1}{v}\int_{E_H}^{E_{por}} \frac{2c}{\sqrt{2e}}de \qquad (3.2)$$

which has the solution

$$P_{por}(v) = P_H(v) + \frac{1}{v}2c\left(\sqrt{2e}\right)\Big|_{e_H}^{e_{por}} \qquad (3.3)$$

using equation 2.4 for the energies

$$e = \tfrac{1}{2}P(v_o - v) \qquad (2.4)$$

then

$$P_{por}(v) = P_H(v) + \frac{2c}{V}\left(\sqrt{P(v_{oo} - v)} - \sqrt{P(v_o - v)}\right)$$

$$P_{por}(v) - \frac{2c}{v}\sqrt{P(v_{oo} - v)} = P_H(v) - \frac{2c}{V}\sqrt{P(v_o - v)}$$

As the pressure approaches infinity $P >> \sqrt{P}$

$$P_{por}(v) = P_H(v)$$

The Oh and Persson gamma predicts infinite pressure only when the solid Hugoniot curve has infinite pressure. This can only happen if the value of $\left.\frac{\partial P}{\partial e}\right|_v$ is zero. Al'tshuler Ref. (44) has given the value of γ at high energies as .5, determined from quantum-statistical calculations. By equation 2.23, this would mean that materials with an initial density of less than 20% of the solid could not be compressed to the solid density by a shock wave.

3.2 Modifications to the Oh and Persson Equation of State

Oh and Persson's equation of state requires a numerical integration for solution. With the large number of cells and time steps in a numeric code, this equation of state produces a very slow and inefficient code. For the current investigation a procedure is required to which modifies the equation of state such that a solution to the integral can be determined. The Oh and Persson equation could be approximately factored into two parts in the following manner:

$$\gamma(v,E) = \frac{c(c+2s\sqrt{2e})}{(2c+s\sqrt{2e})\sqrt{2e+\left(\frac{cv_0}{2\gamma_0 v}\right)^2}}$$

If the above equation is approximated by dropping the $\left(\frac{cv_0}{2\gamma_0 v}\right)^2$ term and the functions ϕ and μ are assumed such that:

$$\gamma(v,E) = \frac{c}{\sqrt{2e}}\frac{(c+2s\sqrt{2e})}{(2c+s\sqrt{2e})} = \frac{\phi}{\sqrt{2e}} + \frac{\mu}{(2c+s\sqrt{2e})}$$

Then:

$$\phi = \frac{c}{2} \qquad\qquad \mu = \frac{3}{2}cs$$

The solution to equation 2.69 becomes:

$$P_{por} = P_H(v) + \frac{1}{v}\int_{E_H}^{E_{por}}\left(\frac{c}{2\sqrt{2e}} + \frac{3}{2}\frac{cs}{2c+s\sqrt{2e}}\right)de \qquad (3.4)$$

Which reduces to

$$P_{por} = P_H(v) + \frac{1}{v}\left(2c\sqrt{2e} - \frac{3c^2}{s}\ln\left(2c\sqrt{2e}\right)\right)\Bigg|_{E_H}^{E_{por}} \tag{3.5}$$

The above equation was further modified to assure a gamma that matches the measured value at low energies. The logarithmic term was also removed to improve the fit to experimental data and the $\sqrt{2e}$ term was halved. The equation of state then becomes:

$$\gamma = \frac{c}{\sqrt{\left(2e + \left(\frac{c}{\gamma_0}\right)^2\right)}} \tag{3.6}$$

$$P_{por} = P_H(v) + \frac{c}{v}\sqrt{2e + \left(\frac{c}{\gamma_o}\right)^2}\Bigg|_{e_H}^{e_{por}} \tag{3.7}$$

The use of the above equation, the approximate Oh and Persson equation of state, has greatly increased the speed of computer programs using an energy dependent gamma equation of state. The approximate Oh and Persson equation of state performs well when compared to the Oh and Persson equation of state. The results are discussed in the next section.

This equation of state, like the original, has the value of the initial Grüneisen parameter at zero energy. For very high energy states the value is approximately:

$$\gamma(\text{energy} \rightarrow \infty) = \frac{c}{\sqrt{(2e)}} \tag{3.8}$$

This is half the value of the Oh and Persson model at very high energy states. Better agreement to data can be achieved if the value of c is fitted to experimental value. The value may be separate from the value from the linear u_s u_p equation of state for the solid.

This equation was further modified to account for the high energy value of the Grüneisen parameter of .5. The Grüneisen parameter is approximated by separating out the high energy value form the low energy:

$$\gamma = \gamma_{\text{lowenergy}} + \gamma_{\text{highenergy}}$$

where:

$$\gamma_{\text{high energy}} = .5$$

then

$$\gamma_{\text{low energy}} = \gamma_o - .5$$

When value of the Grüneisen parameter in equation 3.6 is replaced by the value of the low energy gamma, equation 3.6 becomes:

$$\gamma = \frac{c}{\sqrt{\left(2e + \left(\frac{c}{\gamma_o}\right)^2\right)}} + .5 \qquad (3.9)$$

And equation 3.7 becomes:

$$P_{por} = P_H(v) + \frac{c}{v}\left(\sqrt{2e_p + \left(\frac{c}{\gamma_o}\right)^2} - \sqrt{2e_s + \left(\frac{c}{\gamma_o}\right)^2}\right) + \frac{.5}{v_p}\left(e_p - e_s\right) \qquad (3.10)$$

This represents the new equation of state developed for this work.

3.3 Utilizing the Full Range Equations of State

A full range equation of state must be capable of handling the complete and incomplete compaction regimes. Numeric hydrocodes determine pressure as a function of volume. The rate independent equations have the porosity as a function of pressure. The rate dependent equations have the time rate change of the porosity as a function of the pressure. The following development uses the Oh and Persson incomplete compaction routine.

The full range Hugoniot curve can be determined from equations 2.67, 2.79, and the Rankine Hugoniot shock condition. Solutions to these two equations become complicated. Equation 2.67 relates the compaction as a function of pressure. Equation 2.79 relates the pressure as a function of volume and pressure along the Hugoniot curve of a solid material at the same volume. These equations cannot be solved simultaneously.

To solve the equations an iteration procedure is used starting at the total volume and a guess at the pressure. Next an estimate of the volume of the porous material in the absence of voids is calculated from the pressure. The pressure of a solid at this volume is calculated. The shock energies from equation 2.4 are used in equation 2.67 to solve for Oh and Persson's γ. Equation 2.69 is integrated using the volume of the porous material in the absence of voids to calculate the pressure. If the initial pressure and the final pressure do not match, another iteration is tried with a new pressure. This procedure is tedious and utilizes too much computer time to be feasible in obtaining the Hugoniot curve for a porous material. Complicating the problem is the integral required for the Oh

and Persson equation of state. By trial, a ten step numeric integral is required to fit the experimental data well.

The procedure has been implemented in MY1DL, Ref. (45), a one dimensional Lagrangian hydrodynamic computer code. Some changes in the code where required to accurately model porous materials. The energy of the porous material is computed using equation 2.4 for each time step until the pressure starts to decrease. This eliminates the inaccuracies caused by the numeric integral along the Hugoniot curve used in the code to determine energy. Once the pressure starts to decrease the code follows an isentropic release.

The iterations required to use the Oh and Persson full range equation of state were not efficient in the code, requiring a much longer time to run. It was not added to a two dimensional hydro-code for this reason.

Comparison between different fully compacted equations of state were made using the Oh and Persson incomplete compaction equation. Figures 13, 14 and, 15, show the Oh and Persson full-range equation of state in comparison to data for three materials. The equations of state perform extremely well for these materials. In comparison, Figure 12 shows the Mie-Grüneisen equation of state, which has excellent agreement at low initial porosities, but very poor agreement at low initial densities. Figures 24, 25 and, 26 show the approximate Oh and Persson equation of state. This equation performs at high initial porosities much better than the Mie-Grüneisen equation of state, but not as well as the Oh and Persson equation of state.

A further examination of the equations of state was made for tungsten. Table 1 shows the measure shock parameters for porous tungsten available from the literature. Table 2 shows a comparison of the Mie Grüneisen equation of state to the pressures using two different methods. The first used equation 2.20 directly. The second uses equation 2.19 with an energy calculated from equation 2.4 and the experimentally obtained data. The quality of the methods was determined using the average of the square of the measured pressure minus the calculated pressure. This value is similar to the least mean square value minimized in the optimization of lines and curves. For the values using equation 2.20, the value of this number was 12,036. For the numbers using the energy calculated from the tests the value is 1,239.

This comparison demonstrates some of the problems in using the Mie-Grüneisen equation of state. A pressure can be calculated for a given volume, energy, and γ (from either experimentation or modeling) which does not lie on the Hugoniot curve predicted by the Mie-Grüneisen equation of state.

The large variations in calculated pressure show another problem with incomplete compaction equations. When the material is porous the volume changes rapidly with pressure. Small changes in measured pressure are reflected in large change in the volume of the solid portion of the material. The solids are relatively stiff, and these errors show up as large errors in the calculated pressure and energy of the solid portion.

Another comparison was conducted for the approximate Oh and Persson equation of state, Table 3. The average of the square of the measured pressure minus the calculated pressure was 1,047, with an average error of 3.29 GPa. This was calculated

using a value of c in equation 3.7 of 3.7, which was selected to improve the fit. For a value of c from the linear u_s u_p equation of state of 4.029 the value was 1,074, with an average error of 2.18 Gpa. Changes in the value of c provided only a minimal increase in accuracy. This equation of state provided improved accuracy in comparison to the Mie-Grüneisen equation of state. Comparison between the approximate Oh and Persson equation of state and the data is shown in Figure 16, with a 3.7 value of c.

The proposed equation of state given in equation 3.9 was also compared to the data available, Table 4. The average of the square of the measured pressure minus the calculated pressure was 825, with an average error of 1.64 Gpa. This represents a better fit to the data than the Mie-Gruneissen, Oh and Persson, or the approximate Oh and Persson equations of state. Comparison between the proposed equation and the data is shown in Figures 27 and 28.

The proposed equation of state appears to be a considerable improvement over both of the Oh and Persson equations of state. It has the great advantage, in addition, that it provides for much faster numerical treatment of the hydrodynamic computation problem.

CHAPTER 4

DESIGN OF THE SHAPED CHARGE

4.1 Liner Design

4.1.1 Tungsten as a Shaped Charge Liner Material

From the earlier development, the penetration of a shaped charge jet into a target material is given by:

$$\frac{Penetration}{Unit\ \text{Length of Jet}} = \sqrt{\frac{\rho_{jet}}{\rho_{target}}} \qquad (4.1)$$

Materials with higher densities will provide deeper penetration. Copper, the most commonly used material for shaped charge liners, has a density of 8.930 gm/cc, Ref. (2). Tungsten has a density of 19.224 gm/cc, Ref. (2). From the above equation tungsten could provide a 47% deeper penetration.

The speed of the jet penetrating the target also affects the ultimate penetration. Higher collapse speeds will provide faster jets. However the speed of collapse must not exceed the speed of sound in the liner material by a large factor. When the collapse speed exceeds the sound speed, standing shock waves cause the jet to disintegrate. The speed of sound of the liner material is the ultimate controlling factor. Copper has a linear u_s-u_p fit speed of sound of 3.940 km/sec, Ref. (2). Tungsten has a slightly higher linear u_s-u_p equation of state speed of sound, 4.029 km/sec, Ref. (2). A similar relation holds true for

the ambient speed of sound for tungsten, 5.22 km/sec and for copper, 4.76 km/sec. Ref. (3). Thus a tungsten jet can be driven to a higher jet speed than a copper jet.

The ideal shaped charge jet material undergoes large plastic deformation at high strain rates before failure. This assures long continuous jets. The oxygen free copper used in most shaped charge jets is able to undergo extreme deformation before failure. In contrast, tungsten is a very brittle material. Tungsten's high density and high speed of sound make its consideration as a shaped charge liner worthwhile.

Some efforts have been made to use tungsten in shaped charge liners. Jamet and Lichtenberger Ref. (46) and Fu et. al. Ref. (47) have investigated the use of a copper tungsten mixture for shaped charges. Both reported delayed breakup times. The breakup in both cases formed small particles. The break-up of the typical copper lined shaped charge, by contrast, forms large approximately oval shaped pieces.

Lassila Ref. (48) reported that tungsten shaped charge liners are most likely damaged during the shock loading and release process. Lassila believed the tungsten reconsolidates when the opposite sides if the liner collide during the collapse. Problems with high temperature embrittlement were noted.

4.1.2 Design of the Liners

Because of the long lead time required in procuring porous tungsten shaped charge liners the design was completed before the modeling. This required making estimates of the oblique shock pressure. The pressures were reduced from the shock pressure and temperatures were calculated after shocking and release using equations 2.51 and 2.53,

outlined earlier. Liner porosities were selected to assure that the tungsten would not melt after the initial shock and isotropic release process, as melted jets would not be coherent.

The final state of these materials would be solid, as tungsten has a melting point of 3,410 +/- 20 degrees centigrade, Ref. (49). The above approximation ignores the increase in energy caused by the material recompresion and release during the collapse process. A 65 % initial density liner was selected in the belief that it would remain solid throughout the collapse process and jet consolidation.

Tungsten's properties are highly variable. Its strength and brittleness are highly dependent upon temperature and manufacturing process. The shocked material would not easily fit into any of the mentioned processes of Yih and Wang, Ref. (49). Powder metallurgy, while not at the same extreme strain rates or internal energies, is estimated to be the most similar process. Figures 29 and 30 indicate that the greatest plastic behavior should be expected at about 1000^{o}C.

A shaped charge geometry was selected. It was based upon an existing research liner with a 42 degree angle. The charge is small, allowing it to be tested less expensively. The thickness of the liner was selected to provide sufficient mass for the explosive to propel, assuring the wall velocity is equal to or less than that of a known and well operating copper lined shaped charge, to assure the shaped charge is not overdriven.

Procuring liners became a difficult problem. It was desired to test at least two densities of liner material for comparison. The first liner selected had a density of 65% of the solid material. This liner was provided by Astro Met. of Cincinnati Ohio. The processing methods are proprietary. All that could be found out was that the liner

material was formed to shape, with minor finishing cuts. The material has 2 μm pore size, uniformly distributed. Inspection of the liners showed that liner wall thickness variations exceeded specification, Table 4 and Figure 31. Curved jet formation was expected. The liners received were extremely brittle. One was dropped in handling and shattered, with no visible plastic deformation.

Because of funding limitations only one other porosity could be attempted. Astro Met.'s process could not provide the higher density tungsten required. Sylvania Metals in Towanda, Pennsylvania. could provide 80% porous tungsten in bar stock, but would not provide the machined pieces. The stock was purchased. The materials were extremely brittle and hard. Ferromatic in Totawa, New Jersey, was selected to do the machining. The initial design was to have equal weight liners of both 65% and 80% initial density liners. The liners were to be of identical dimensions, except for the liner thickness. In this manner the two tests would have approximately equal jet characteristics with materials at different energy levels, see Figure 32. Because of the brittle nature of the material, this design was not feasible. Half of the bar stock was lost in the first efforts of machining the parts. Modifications where made in the tip region to allow the lathe to hold a thickened portion of the liner. As the tip region generally does not have the time to accelerate to full velocity, its contribution to the jet formation is small. This modification was the least intrusive, see Figure 33. In fabrication the thickened end broke off. A cap was machined from aluminum to prevent the detonation products from interfering with the shaped charge jet formation. The final tested liner is shown in Figures 34 and 35. A direct comparison between the two liners densities is not possible because of the large number of modifications.

4.1.3 Heat Transfer Within the Shocked Material

For shock compaction considerations the porous material is generally assumed to be homogeneous. For this assumption to be valid the heat transfer throughout the material must be rapid. A heat transfer estimate was made for the 65% porous material with a 2 μ m pore size. Assuming a spherical pore, a hot spot of tungsten of equal size within an infinite mass of tungsten the following heat transfer equation applies:

$$\frac{1}{r}\frac{\partial^2}{\partial r^2}(rT) = \frac{1}{\alpha}\frac{\partial T}{\partial t} \qquad \alpha = \frac{k}{\rho c}, \text{ assumed constant} \tag{4.2}$$

For the Initial Conditions:

T=3000 °C at r=0 to 2 μm

T=298 °C at r=2 μm to infinity

The above approximation was solved numerically. After 0.4 μ seconds the temperature at the core was 322.27 °C. Even with this crude approximation, because of the extremely quick heat transfer from the pores, the material is near equilibrium at the collapse point.

4.2 Explosive Loading

Proper explosive loading is required for optimal performance of a shaped charge. If the liner is tilted in relation to the charge, the collapse will be non uniform, and the jet will be tilted. The jet will also be tilted if the detonation wave is not uniform. A booster charge and alignment fixture, Figures 36 and 37 is used to assure proper initiation. Proper alignment of the liner was troublesome because of the poor quality of the liner edges. A loading fixture was made to hold the liner in the body during loading, Figures 38 and 39.

CHAPTER 5

EXPLOSIVE TESTING AND ANALYSIS

5.1 Explosive Testing

The loaded shaped charges where tested at ARDEC, Picatinny Arsenal, NJ, at the 1600 explosive test site. Flash radiography was selected to observe the shaped charge jets and the collapse process.

The flash radiograph provides a 30 ns exposure of radiation. The x-ray heads are each powered by a capacitor bank. Because of the limitations of the x-ray tubes, a separate head is used for each exposure. The x-ray film is located behind the event, so a shadowgraph is formed. The separate heads cause multiple exposure to be offset from each other. Kodak 8" x 10" XAR-5 film was used with a 3M brand Trimax T-12 intensifier screen. The relatively large anode in flash radiograph machines causes some image blurring. By maximizing the distance between the tube head and the event, and minimizing the distance between the event and film, the blur is minimized. Protecting the film is critical in explosive testing. A half inch thick aluminum plate and 2" of foam are used in front of the film. Behind the film 2" of foam and a half inch of plywood are used, as the film is ejected from the test area by the detonation product.

A witness plate is located beyond the film to record penetration. The relatively large distance between the shaped charge and the witness plate allows a long time for curvature of the jet to develop from radial velocity components. With the variations

measured in the liner contour the curvature should be large, and little penetration was anticipated.

The shaped charge, film cassette, and the witness plate were placed on a wooden stand, which was destroyed in each test. The charge was supported on the extreme ends, away from the liner area, with the opening of the liner pointed horizontally at the witness plates. This prevents reflected shock waves from the supports interfering with a uniform liner collapse, which would contribute to a curved jet formation.

An exploding bridge wire detonator, EBW, was used to initiate the charge. These detonators require large voltages for initiation, and specially constructed firing units. The use of these detonators greatly increase the safety of explosive testing. The test set up is shown in Figures 40-46.

5.2 Test Results

A cast TNT explosive fill was used in the shaped charge. This was a poor choice, as cast TNT is difficult to initiate, particularly in small sizes. The charge did not detonate, but was smashed by the shock from the booster pellet. The next effort was to use cast TNT with 5% by weight RDX. RDX is a high detonation velocity powder explosive almost insoluble in molten TNT, that would provide ignition points for the TNT. The small amount of RDX assure that the energy of the fill and its detonation velocity would not be greatly increased.

Since the explosive used was not standard, the data for the equation of state was not available. The Cheetah Thermodynamic detonation code, Ref. (50), was used to compute the JWL equation of state coefficients.

The test formed cohesive jets, as shown in Figures 47 and 48. The shaped charge jets were curved, as was anticipated from the inspection data on the liners. The other striking aspect of the jets was the lack of visible particles as the jet stretched. The jets maintain the same diameter while they stretched. The jets must be increasing their porosity as they stretch, instead of necking down and particulating. This is only possible if the material has near zero strength after the collapse process.

A jet that is stretching in this manner would have some peculiar penetration characteristics. For a conventional jet, the diameter reduces as the jet stretches. If the length of the jet is doubled, each element of the jet would also double in length and provide approximately twice the penetration, assuming a linear jet velocity profile. For this jet a doubling of the length would decrease the density by half. The increase in penetration from each element would only be 41%, see equation 4.1.

Examination of the witness plate and the test chamber after the test showed another interesting feature of the porous liner. No slug was discovered, nor any evidence of one found on the witness plate. It is surmised that the slug also had very little strength and broke up prior to or upon hitting the witness plate.

The 80% density liner was also tested. The radiograph, Figure 49, shows that the jet was not cohesive. Because of the large changes from the desired liner no further attempts were made.

CHAPTER 6

COMPUTER MODELING OF THE DETONATION AND COMPARISON TO TEST RESULTS

6.1 Computer Modeling

The problem was computer modeled utilizing Lawrence Livermore National Laboratories CALE, 2 -D ALE (arbitrary Lagrangian -Eurlerian hydrocode), Ref. (33). This code was selected for several reasons. It has a very good reputation in modeling shaped charges. The ALE modeling routine can handle the severe mesh distortions associated with the collapse of a shaped charge liner. The code has routines to add back energy lost due to the approximation of a shock front as a non-discontinuous surface.

The version of the TEPLA-F equation of state in the CALE code was used. The data for the fit was not available, so a fit was created utilizing the data in Table 1. To eliminate the effects of incomplete compaction only the higher pressure data, where complete compaction has occurred, was utilized. The crush curve, equations 2.101 and 2.102, can then be ignored as it is assumed the material is completely densified in the compaction process. The data for low initial density materials was also eliminated to reduce the effects of their very high internal energies which are not be experienced in the modeling. The mean square difference was determined for each set of coefficients and a fit was determined by trial and error which provided the least mean square error between the measured and fitted pressure. The form of the equations used in CALE is:

$$P_s = A0 + A1 * mu + A2 * mu^2 + A3 * mu^3 + (B0 + B1 * mu + B2 * mu^2) * e \quad (6.1)$$

$$P = (1 - POR) * P_s(DENs) \quad (6.2)$$

$$DENs = DEN / (1 - POR) \quad (6.3)$$

$$mu = DENs / REFD - 1 \quad (6.4)$$

$$Pc = -P0 * \ln(POR) \quad (6.5)$$

where: P_s = The solid pressure

A0, A1, A2, A3, B0, B1, B2 are constants

e = The energy

POR = The porosity

DENs = The density of the solid

Pc = The compaction pressure (pressure at which the porosity begins to squeezes out

The values used were:

A0	0
A1	3.313
A2	1.64
A3	0.165
B0	2.585
B1	.2965
B2	-.01255

6.2 Comparison Between Model and Testing

The initial configuration is shown in Figure 50. The results of the model are shown in Figures 51 through 59. The film results were measured with a Gaerdner film analyzer, with a resolution of .001 mm. This resolution is greater than that of the film. The jet tip speed was measured between two flash radiographic exposures. The jet and slug diameter were determined at the exposure 20 μs after the function of the detonator. The 20 μs would correspond to 18.2 μs in the modeling due to the time delay in the functioning of the detonator. The modeling at a time of 17 μs was used to determine the jet and slug diameters. These determined values of jet velocity and jet and slug diameters are summarized as:

	CALE Modeling	Analysis of Radiographic Film
Jet Tip Velocity cm/μs	0.638	0.641
Jet Diameter cm	0.24	0.20
Slug Diameter cm	0.43	0.30

These figures agree very well. The shape of the jet in the model and on the radiograph are very similar. The fine particulation of the jet confirmed the estimation of near zero yield strength.

Figures 58 and 59 show the axial velocity and density along the jet at 20μs. The velocity at this early time did not have a linear relationship with distance from a collapse point. This is typical of shaped charges. At later times the relationship is more linear.

The virtual origin assumption, section 4.2, improves with distance from the origin. Figure 60 shows the reduction in density along the jet. The further the jet is from the collapse point (where the model indicated complete pore collapse exists) the more time the jet has to elongate.

The pressure on shocking the porous material ranged from 29.58 Gpa at the apex of the cone, which is nearly normal to the detonation, to about 7.4 GPa towards the base of the charge.

Equation 2.49 was solved numerically to determine the temperature of the shocked material. The Hugoniot curve was determined, utilizing the Oh-Persson incomplete compaction equation, equation 2.79, and the proposed gamma function given in equation 3.9. Equation 3.9 was also used to compute the value of gamma in equation 2.49. This method of computation was selected over the approximate integral in equation 2.51 because of the amount of data available on the thermal properties of tungsten.

Yih and Wang's Ref. (49) collection of properties for tungsten provided the effect of variation with temperature in the variables of: specific heat at constant pressure, bulk compressibility, and the linear expansion coefficient. From the equation relating specific heat at constant volume and pressure, Ref. (51):

$$c_v = c_p - vT * \frac{(3\alpha^2)}{K_T} \qquad (6.6)$$

where:

c_v= the specific heat at constant volume

c_p= the specific heat at constant pressure

v= the specific volume

α = the linear expansion coefficient

K_T = the isothermal bulk compressibility

The thermal expansion coefficient was calculated by modifying the equation in Yih and Wang for the thermal expansion , for temperature in °C, based upon the length at 25 °C:

$$\frac{L - L_{25^\circ C}}{L_{25^\circ C}} * 100 = A_0 + A_1 T + A_2 T^2 \qquad (6.7)$$

The values of the constants where taken as that of a powder metallurgical rod, 8.69e-3, 3.83e-4, and 7.92e-8 respectively. The values were not adjusted for the porosity of the material. The effect of porosity was not accounted for with any of the values used, it is being assumed the specific heat is not dependent upon the porosity.

The specific heat at constant pressure, for temperature in °K, was given by:

$$c_p\left(\frac{cal}{gm^\circ C}\right) = .032426\left(1 - \frac{4805}{T^2}\right) + 2.1773e-6T + 5.52461e-13T^3 \qquad (6.8)$$

The bulk compressibility, for temperature in °C, was given as:

$$K_T\left(\frac{dyne}{cm^2}\right) = 3.108e12 - 1.759e8 \times T + .344e4 \times T^2 \qquad (6.9)$$

When the variables were calculated, the value of the proposed gamma changed very little. For the pressure on the sides of the shaped charge the value was reduced to about 1.53. For the apex of the liner, which experienced the greatest shock, the value was 1.51. A constant Mie-Grüneisen equation of state would have been applicable to this problem. The initial temperature of the material was assumed to be 20 °C. The final temperatures at shock compression were determined to be about 623 °K (350 °C) at the sides of the cone and about 2,360 °K (2,087 °C) at the apex. This is well below the melting point of the tungsten.

CHAPTER 7

DISCUSSION AND CONCLUSIONS

The investigation into shaped charges using porous tungsten liners necessitated an investigation of the Mie-Grüneisen equation of state, to find the temperatures generated in the shocked material, and of the properties of the shaped charge jet.

7.1 Equations of State for Porous Materials

The Mie-Grüneisen equation of state and the relationships between the Grüneisen parameter and state properties where investigated. The Grüneisen parameter is required for the determinations of shock pressure, temperature, and the speed of sound of shocked materials. A constant Grüneisen parameter is required if the constant specific heat at constant volume is assumed to be constant. At very high internal energies and temperatures, the specific heat at constant volume changes with energy and the constant gamma assumption is therefore not valid.

The Oh-Persson equation of state, which reduces the Grüneisen parameter for high internal energy states, does not predict the larger volumes at higher shock pressures known to exist for materials of low initial porosity. The Oh-Persson equation of state requires a numerical integration to determine the value of gamma. This increases the computer time required to model a problem. An approximate Oh-Persson equation of state was developed that eliminates the numeric integration, but does not allow for the

progressively larger volumes at higher shock pressures seen in materials with high initial porosities.

A proposed equation of state for shocked porous tungsten was developed. The new equation of state has a minimum value of the Grüneisen parameter at high energies and adds a component based upon the internal energy:

$$\gamma = \frac{c}{\sqrt{\left(2e + \left(\frac{c}{\gamma_0}\right)^2\right)}} + 0.5 \qquad (3.9)$$

The term added, a constant equal to 0.5, is equivalent to the approximate Oh-Persson equation of state with the value of gamma reduced by one-half. This equation of state has the high and low energy asymptotes that match the known values of γ, as well as a functional relationship similar to Oh-Persson's equation of state.

7.2 Porous Tungsten Jets

Tungsten shaped charges were fabricated with an explosive charge of 95% TNT and 5% RDX. The liners where made from 65% solid density tungsten with an included cone angle of 42°. Flash radiographs of the detonating charges where used to record the jet. The measured jet velocity was 0.638 cm/μs. The jet broke up into small particles instead of necking down and breaking into beads, as do most copper lined shaped charges. No slug was recovered after the testing.

Computer modeling was conducted to investigate the breakup phenomenon noted for the porous tungsten jet. A fit was developed for the TEPLA-F equation of state for

high initial porosity tungsten. The computer model had a jet speed of 0.641 cm/μs, very close to that of the test. The porous tungsten was modeled with zero strength, in order to match the breakup phenomenon shown in the testing. The model accurately predicted the breakup seen in the test. It is concluded that the porous tungsten under these conditions has near zero strength.

The density of the jet is reduced for longer stand off distances. This reduces the penetration capability of the jet, making it suitable only as a small stand-off item. The shaped charge did not leave a solid slug after the collapse process, due to the low mechanical strength of the shocked porous tungsten.

As indicated by the modeling and the jet temperature computations, the jets in this study did not have shock pressures high enough to elevate the jet temperatures much beyond that of systems with solid liners. Shock temperature calculated for walls of the liner was about 350 °C.

CHAPTER 8

RECOMMENDATIONS

The recommendations for future study are separated into two different categories. The first relates to obtaining a solid jet that stretches with a solid density, reducing diameter instead of density. The second relates to the predicted penetration characteristics of a jet that stretches with uniform diameter, but reducing density.

8.1 Design of a Porous Lined Shaped Charge

An improved design would significantly increase the temperature of the liner material. This could be achieved in a number of ways; by utilizing a more normal impact of the detonation wave, by utilizing a much higher initial porosity, or utilizing a higher energy explosives, or a combination the above. This increased temperature may greatly increase the ductility of tungsten and eliminate the extremely fine fragmentation that is exhibited in the 65% initial density tungsten liner in this work.

8.2 Penetration by a Jet with Linear Density and Velocity Distributions

Modeling indicated that the density for the jet is approximately linear along the axis of symmetry. For a jet that remains solid equation 2.152 relates the penetration to the jet velocity for a jet with a linear velocity distribution. A similar equation can be developed for a jet with linear velocity and density distributions.

For a linear density distribution

$$\rho_j = \rho_s \left(\frac{x_{tip} - x}{x_{tip}} \right) \tag{8.1}$$

where: ρ_s = the solid density of the jet

For the linear velocity distribution assumption, for any point along the jet

$$x = vt \tag{8.2}$$

The density as a function of time is then given by

$$\rho_j = \rho_s \left(\frac{V_{Tip} - V}{V_{Tip}} \right) t \tag{8.3}$$

Substituting the above equation into equation 2.152

$$\frac{V}{\left[1 + \left(\frac{\rho_T}{\rho_s \left(\frac{V_{Tip} - V}{V_{Tip}} \right)} \right) \right]^{1/2}} = V + t \frac{dV}{dt} \tag{7.4}$$

A series of penetration velocity experiments would show if the assumption of a linear density distribution is valid. These experiments are conducted by placing thin time of arrival probes between witness plates.

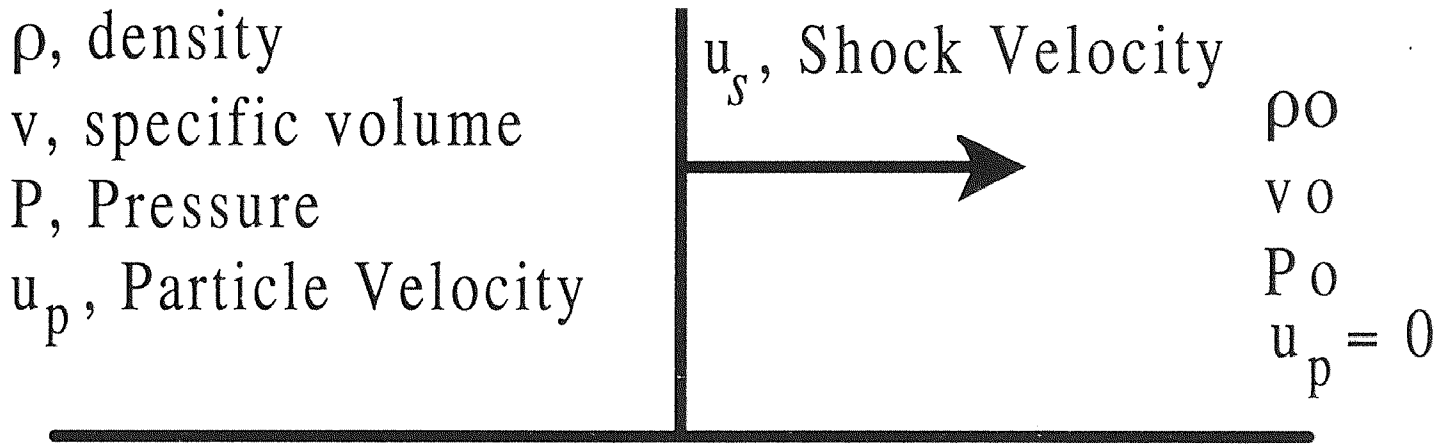

Figure 1. One Dimensional Shock Wave

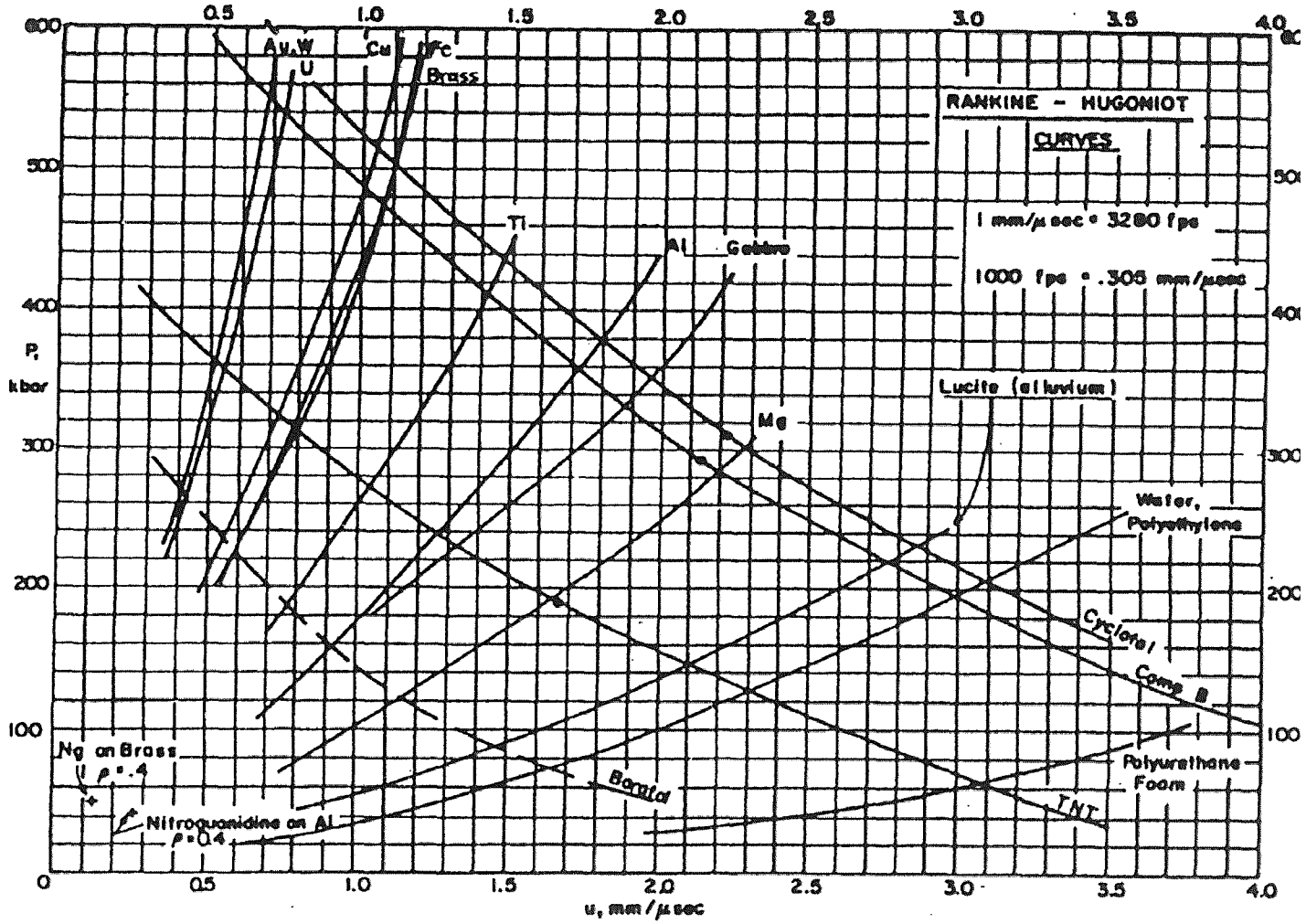

Figure 2 LASL Shock Hugoniots Ref(2)

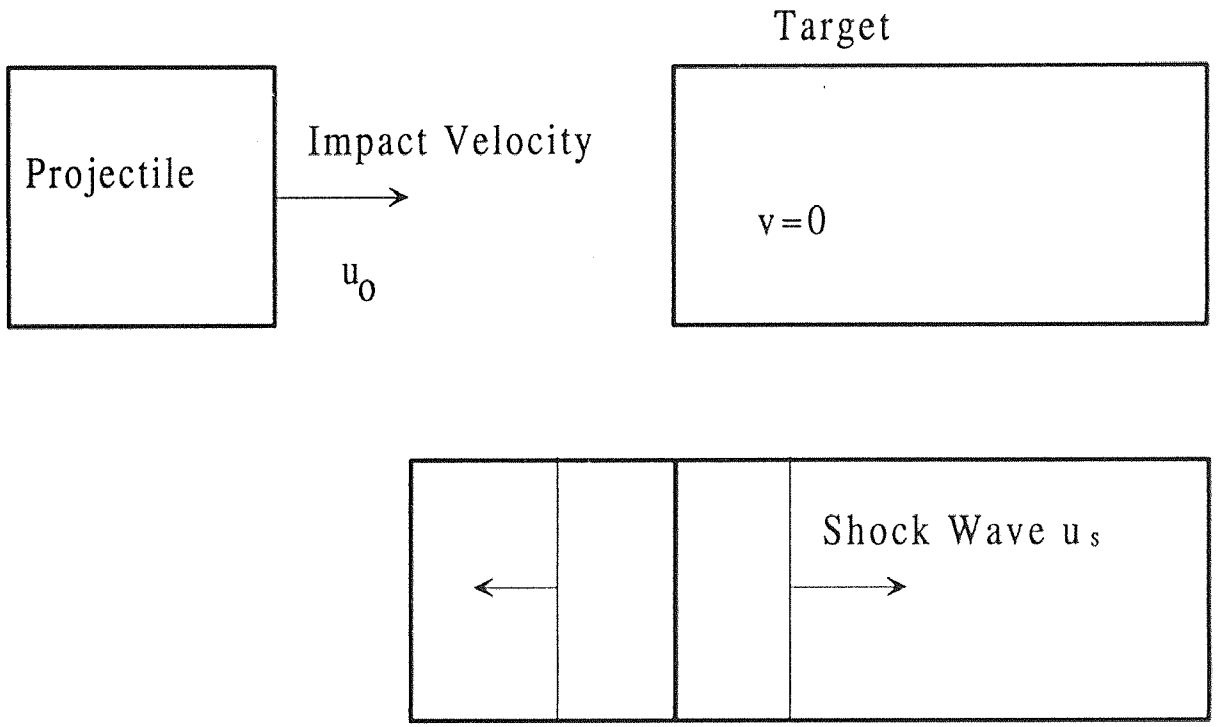

Figure 3 Shock Waves from Plate Interactions

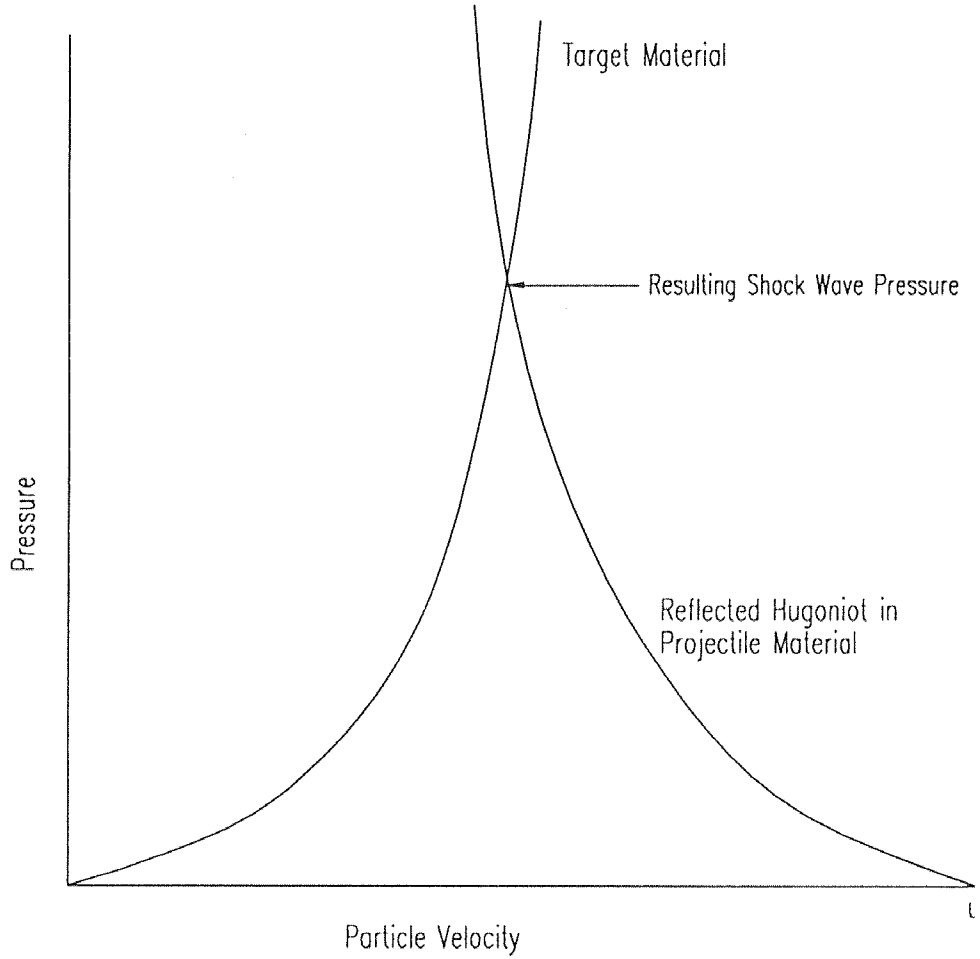

Figure 4 Graphical Solution for Shock Matching

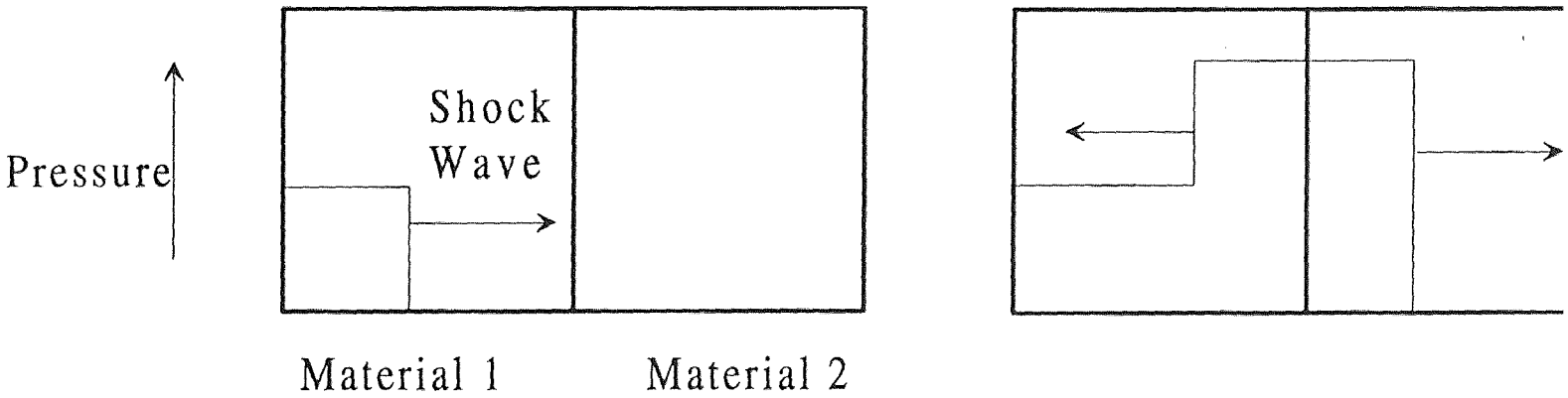

Figure 5 Shock Transfer into a Material of Higher Shock Impenance

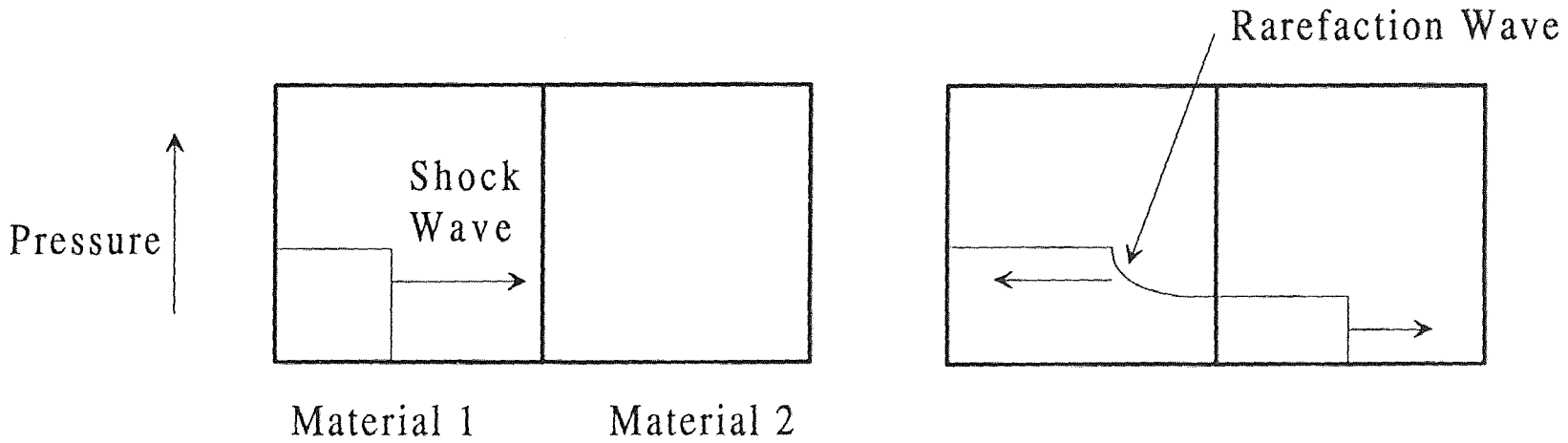

Figure 6 Shock Transfer into a Material of Lower Shock Impedance

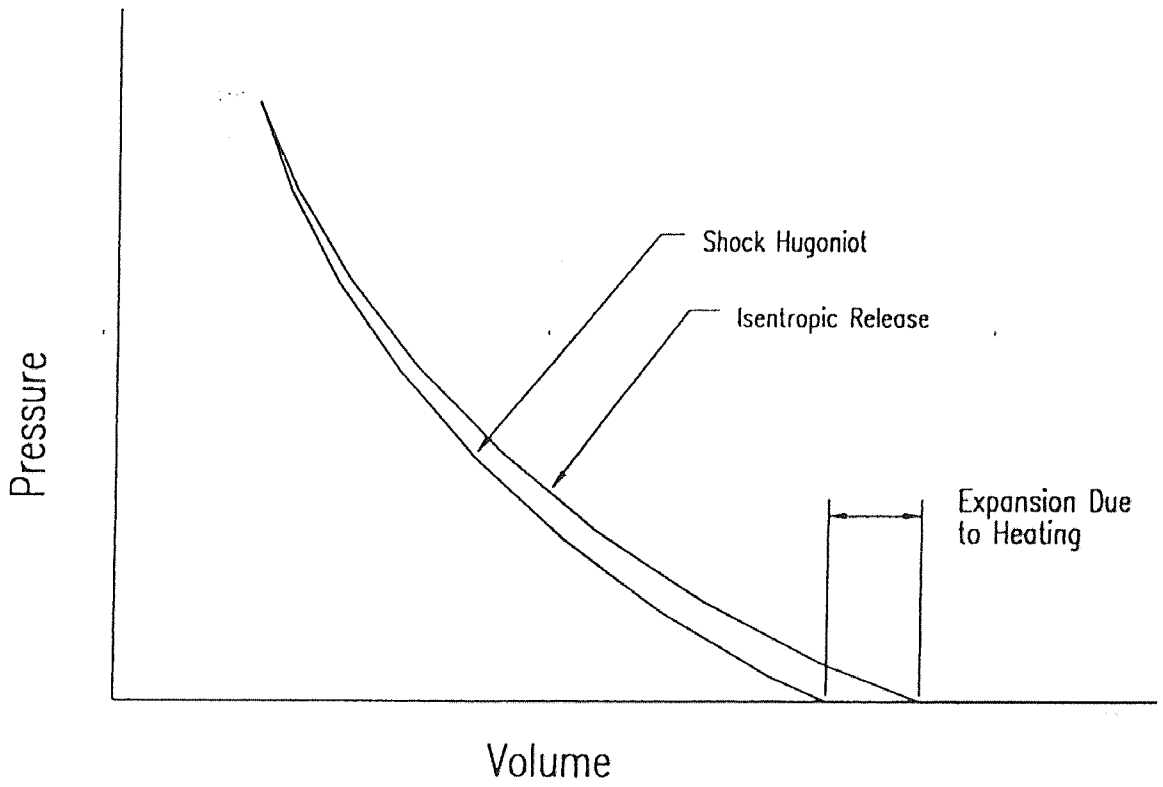

Figure 7 Isentropic Release of a Shocked Material

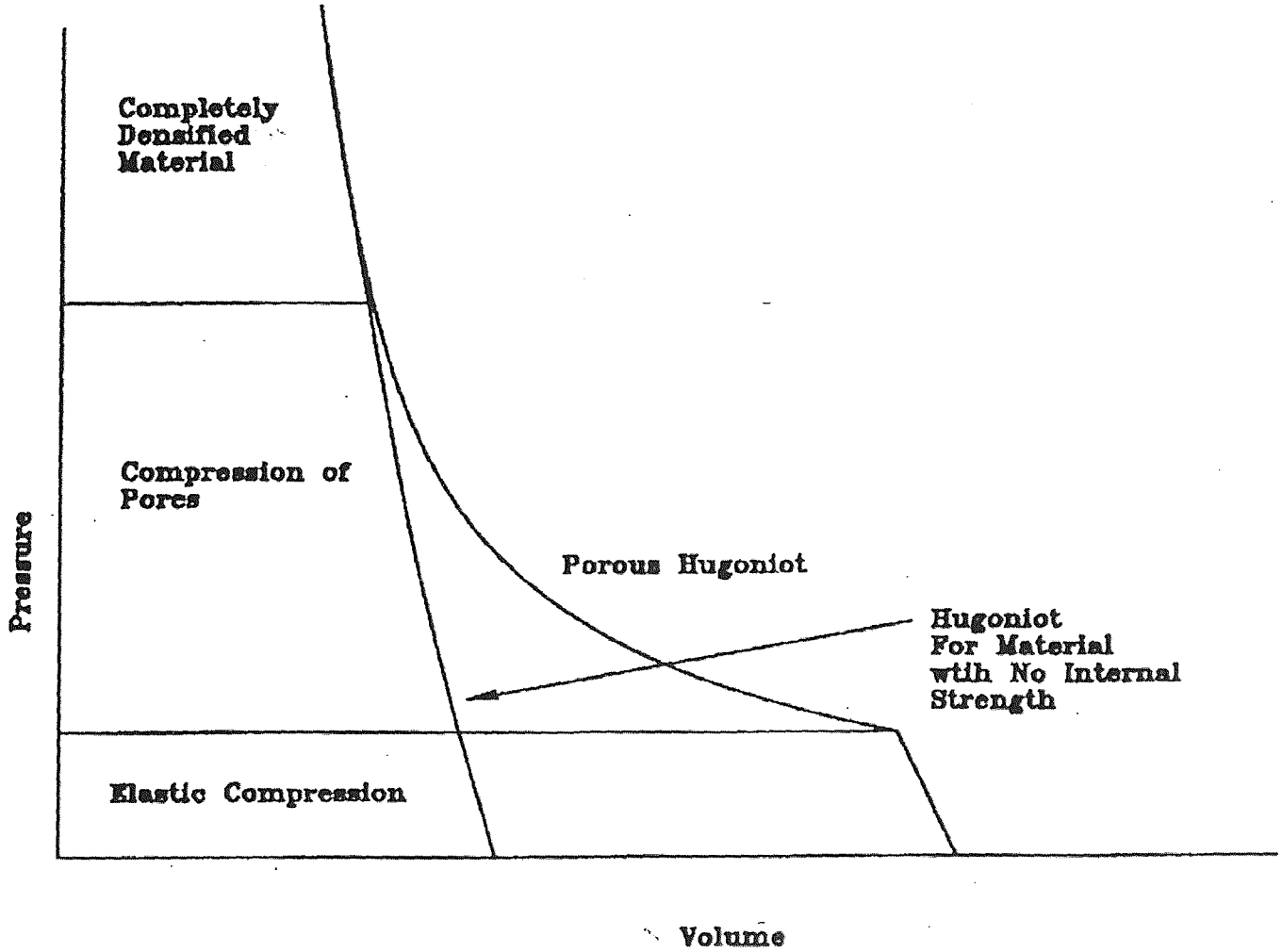

Figure 8 Shock Compression of a Porous Material

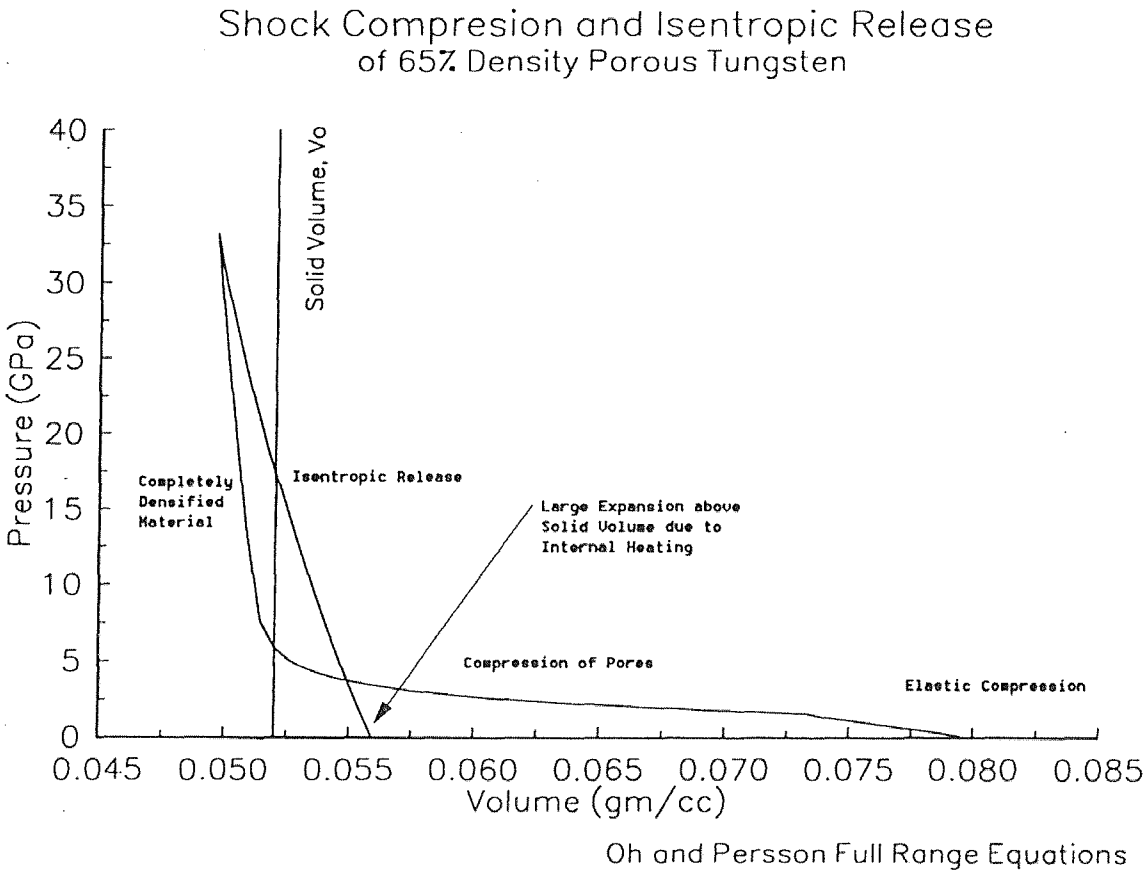

Figure 9 Isentropic Release of Initially Shocked Tungsten
Initial Density 65% of Solid Density

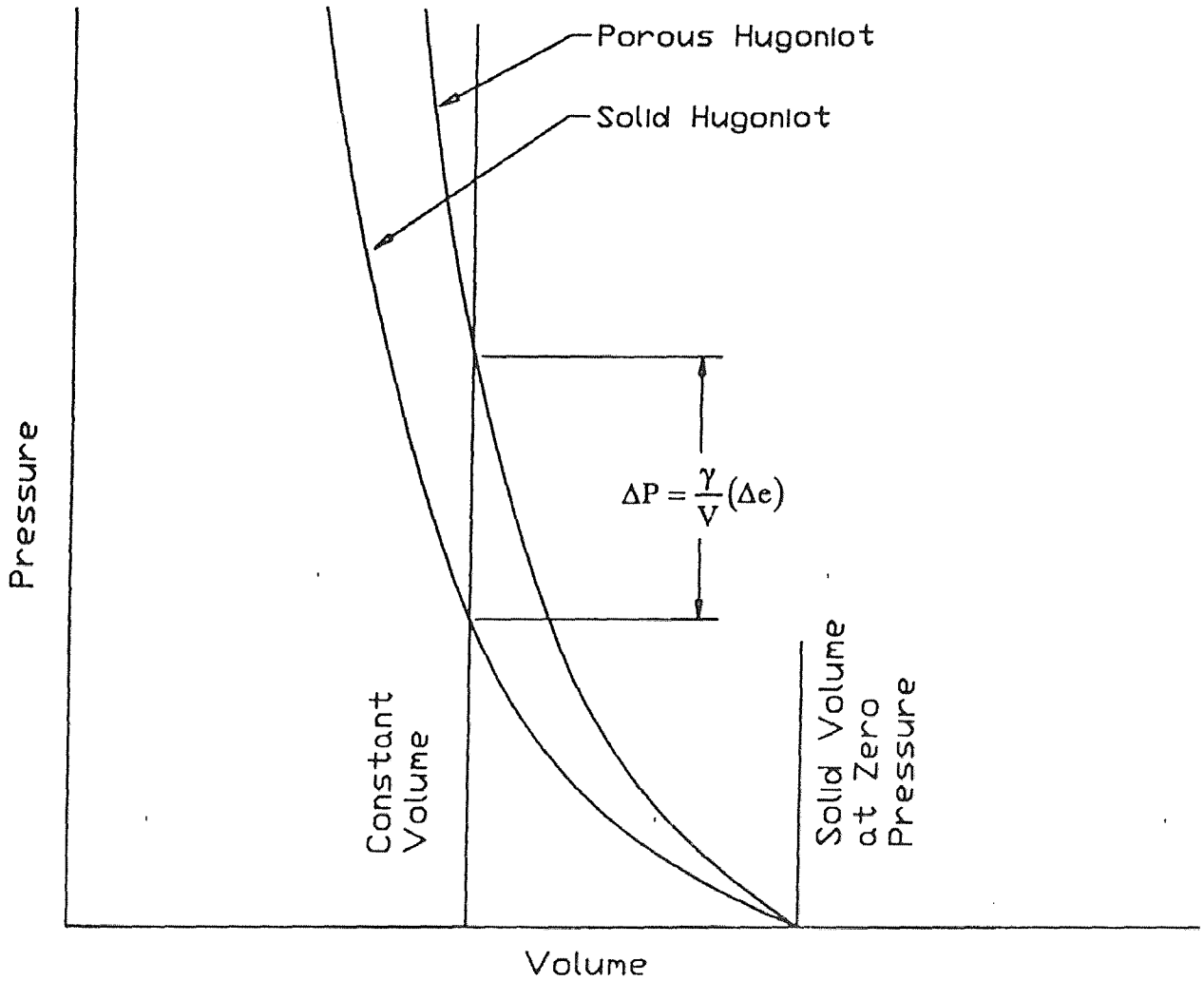

Figure 10 Pressure Computation by the Mie-Grüneisen Equation of State

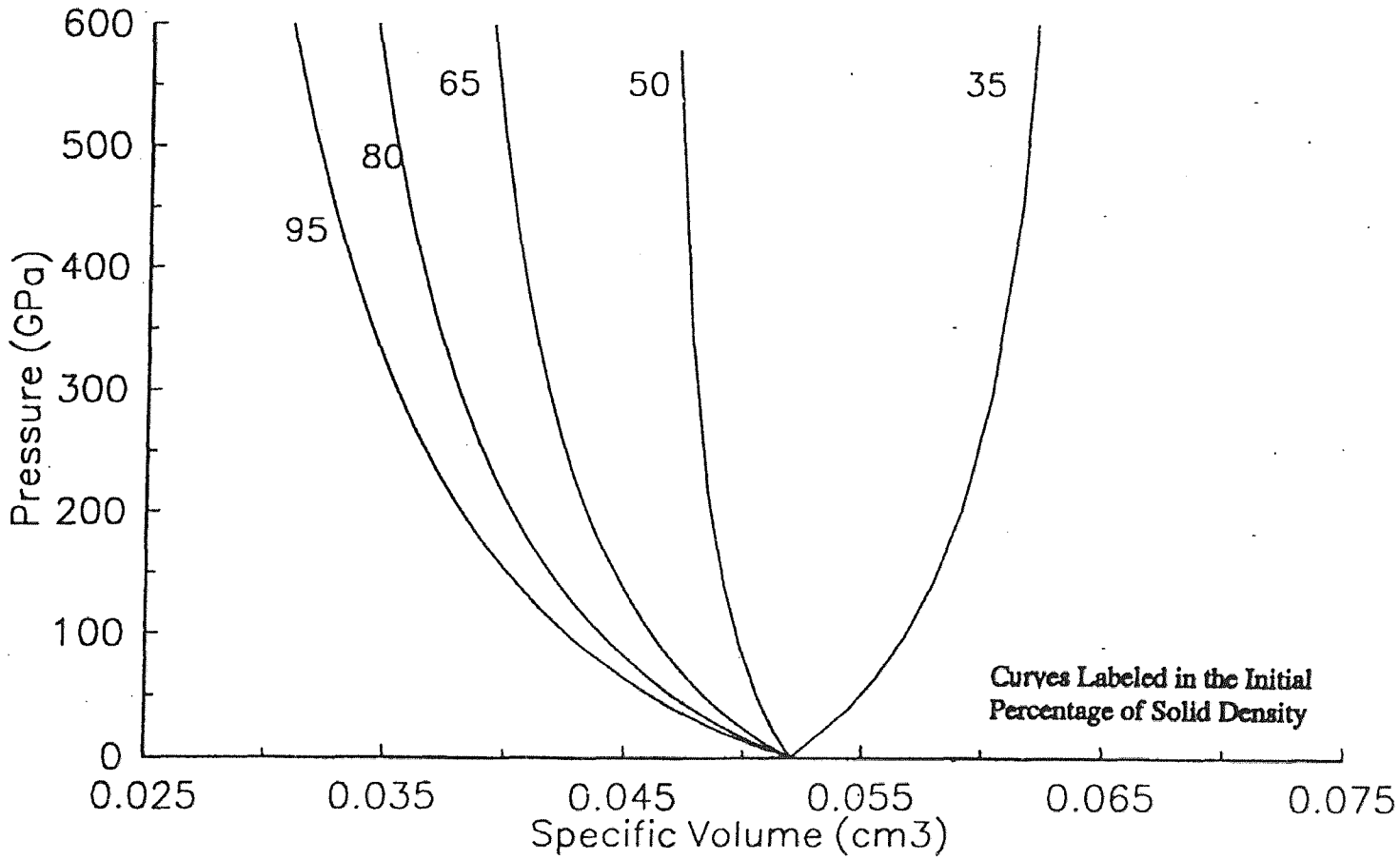

Figure 11 Shock Compaction of Porous Tungsten
Mie- Grüneisen Constant Gamma Equation of State

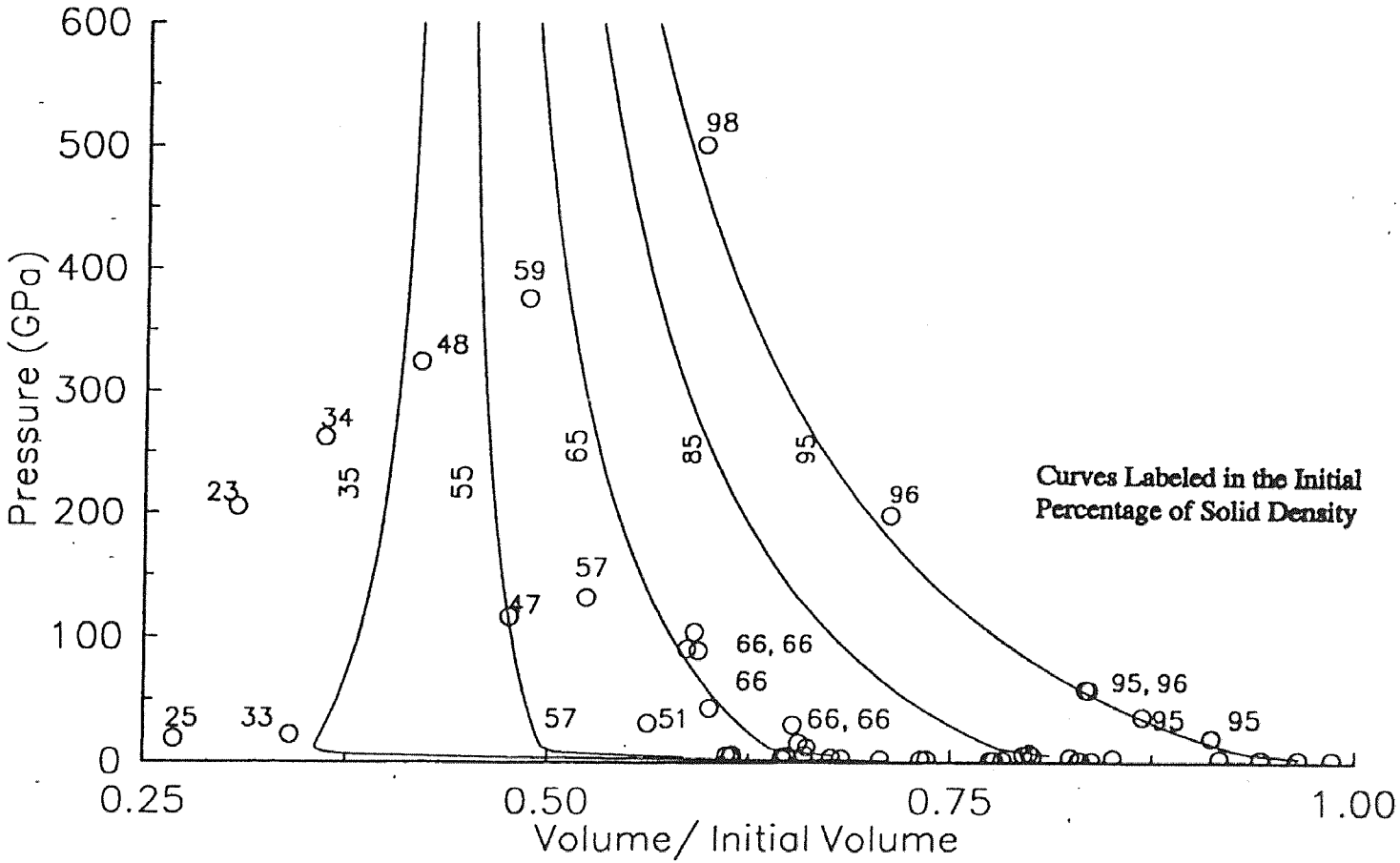

Figure 12 Shock Compaction of Porous Tungsten
Mie- Grüneisen with Oh's Compaction Compared to Data

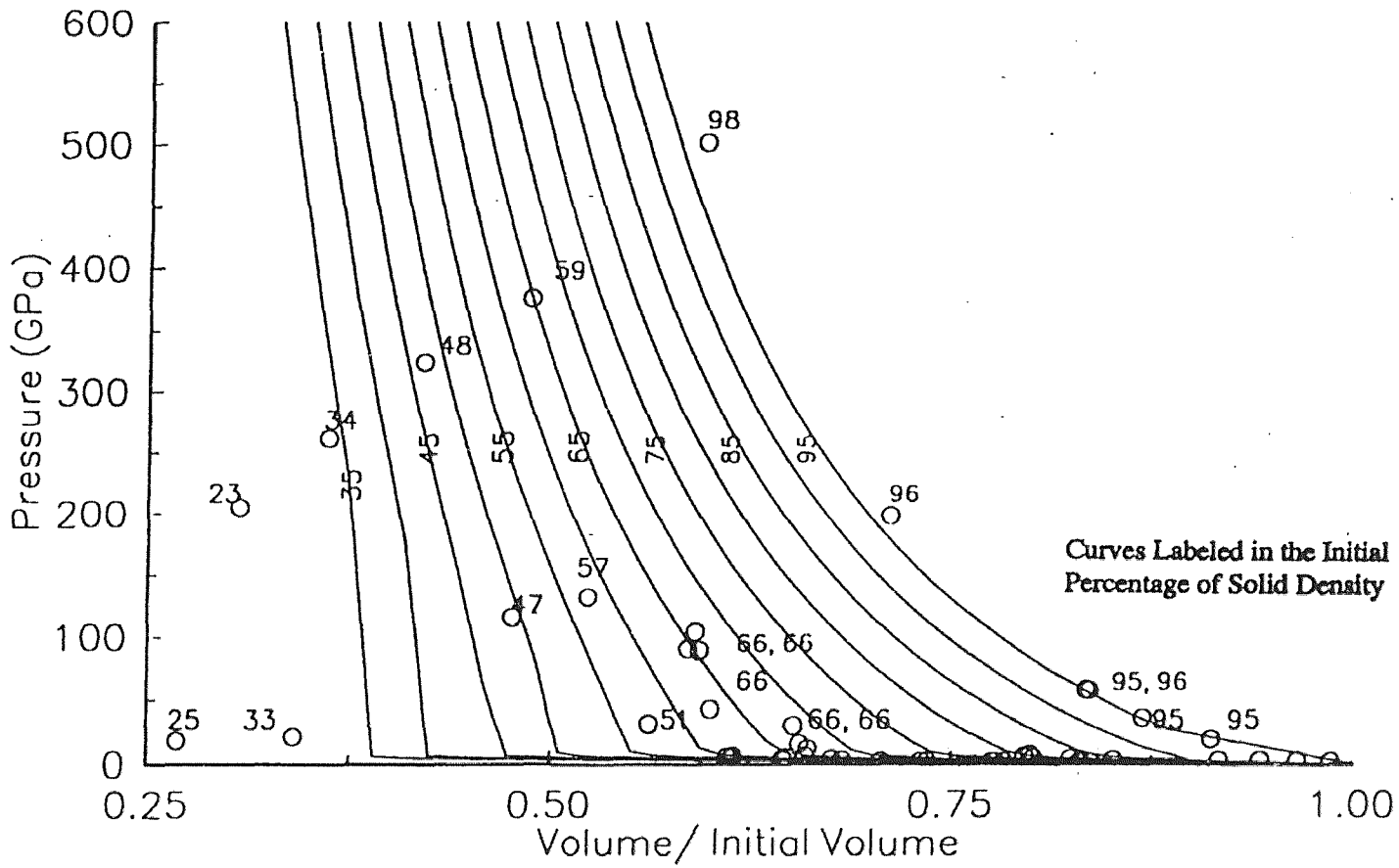

Figure 13 Shock Compaction of Porous Tungsten
Oh- Persson Equation of State Compared to Date

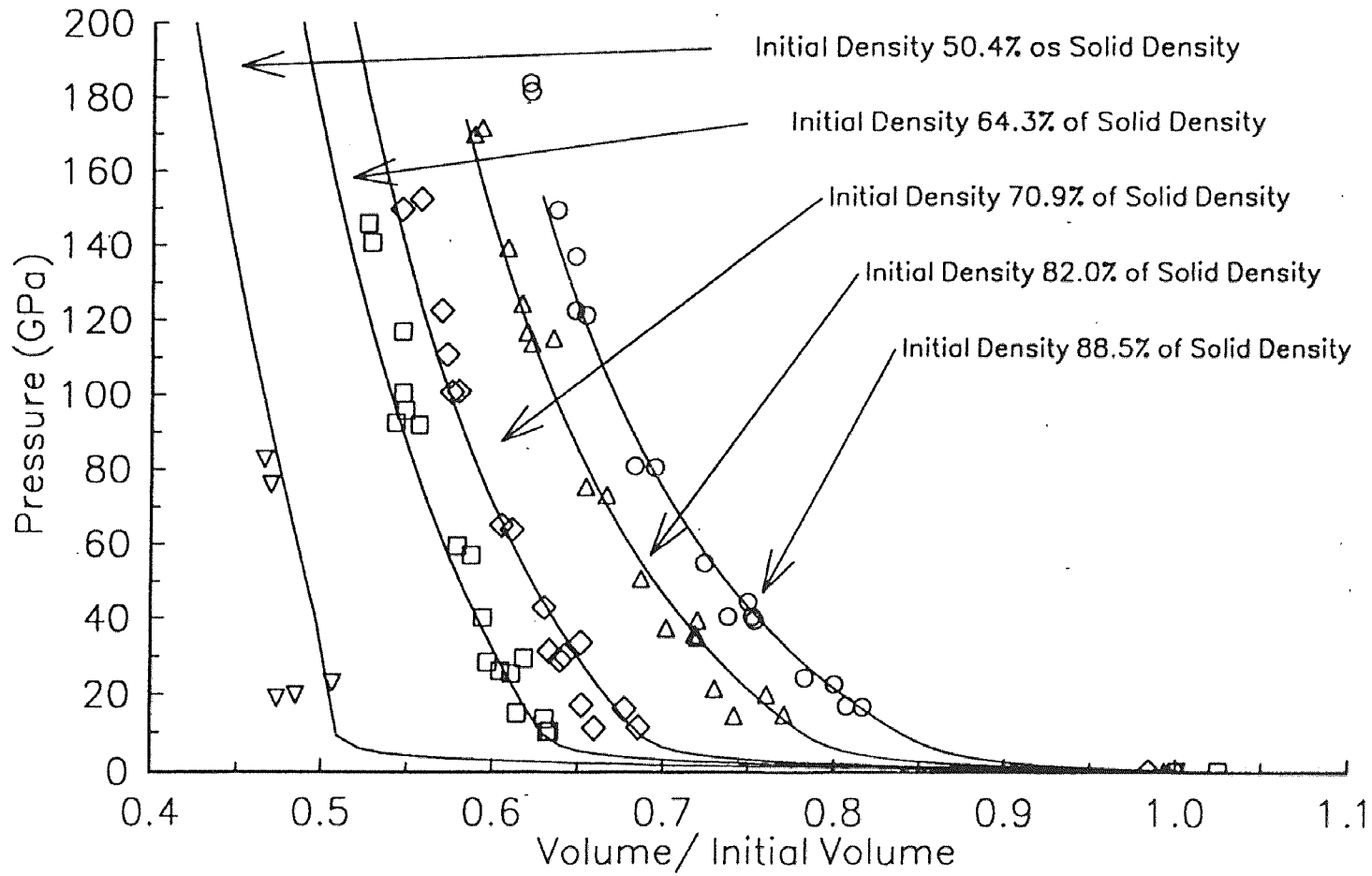

Figure 14 Shock Compaction of Porous Copper
Oh- Persson Equation of State Compared to Data

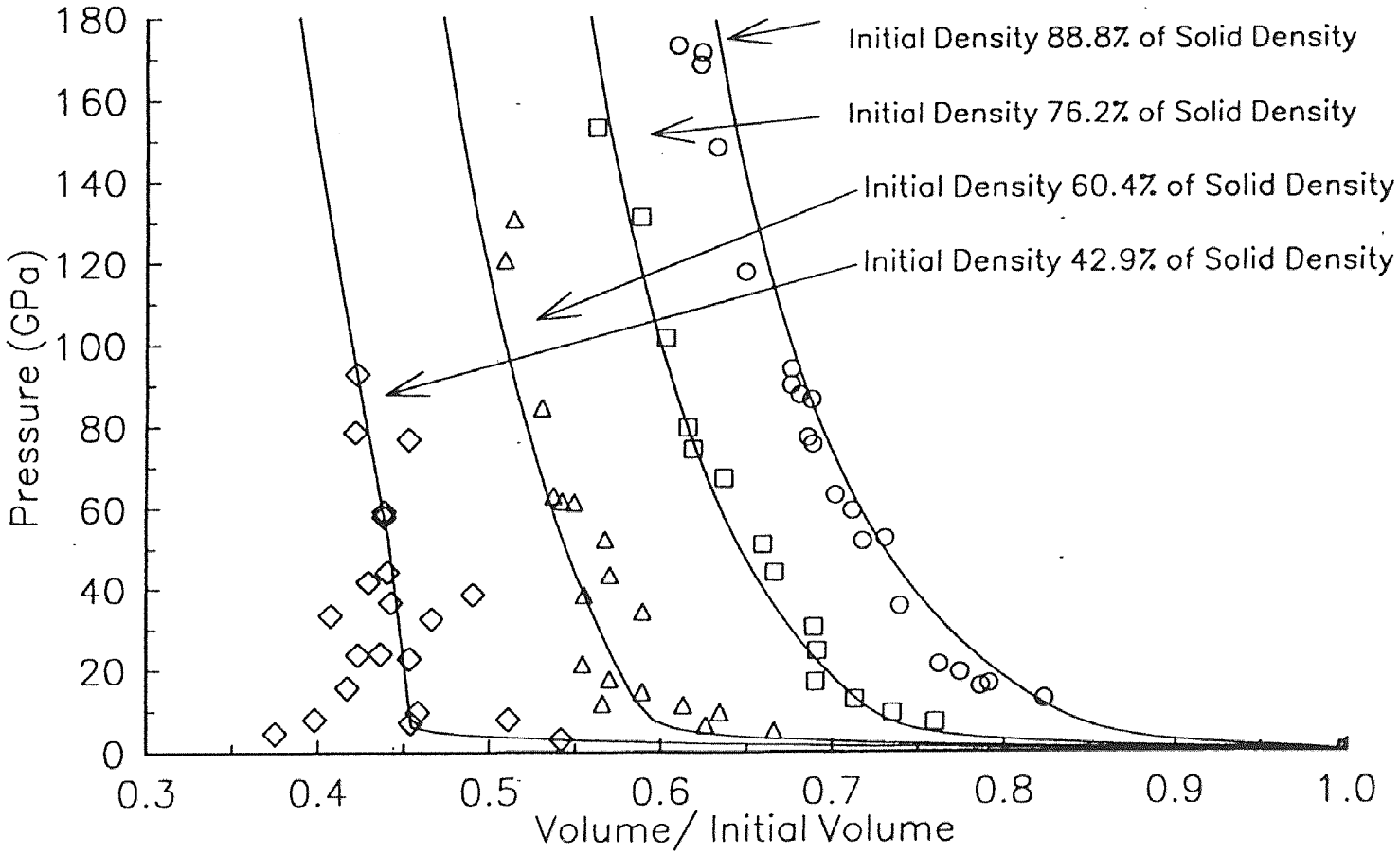

Figure 15 Shock Compaction of Porous Iron
Oh- Persson Equation of State Compared to Data

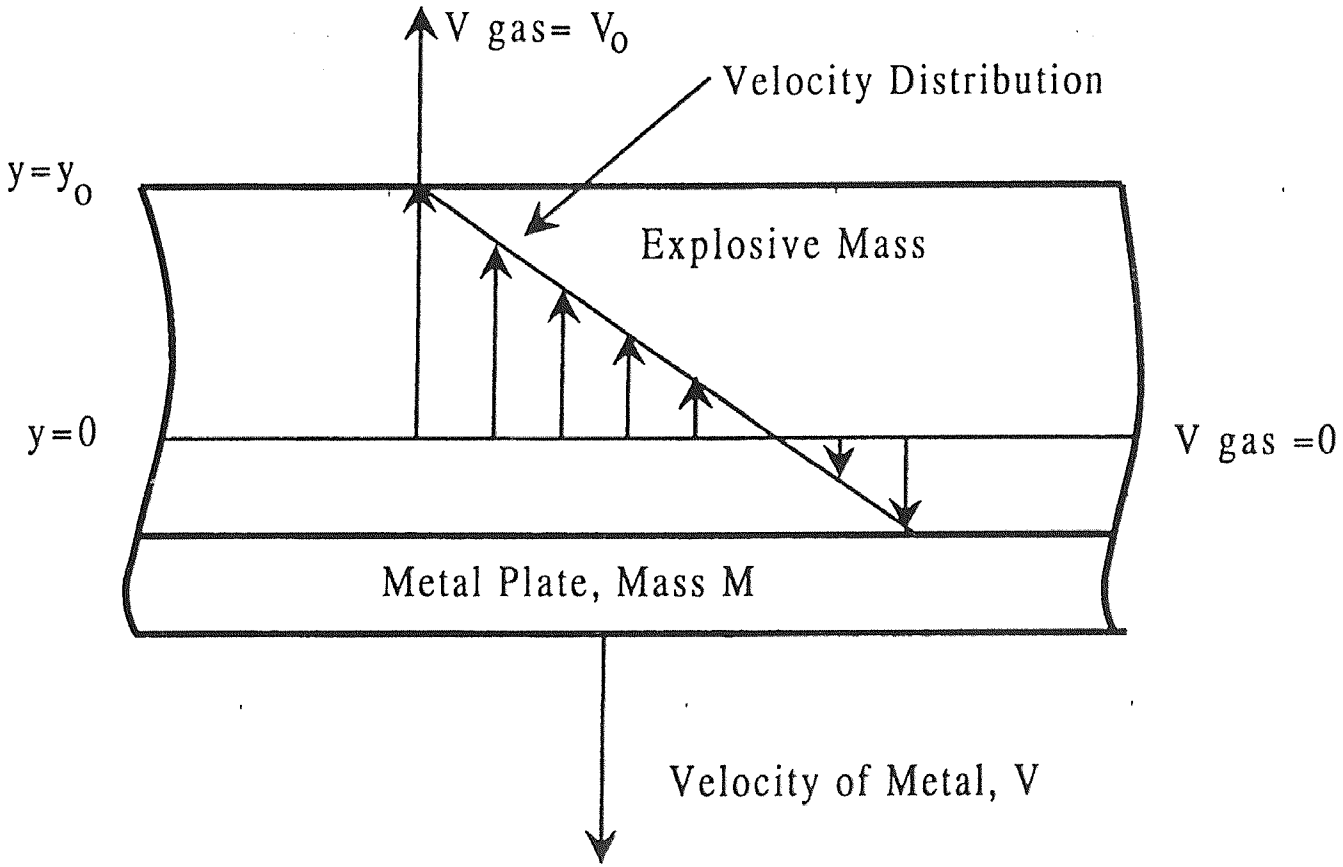

Figure 16 Gurney Method for Estimating the Velocity of Metal Driven by a Detonation

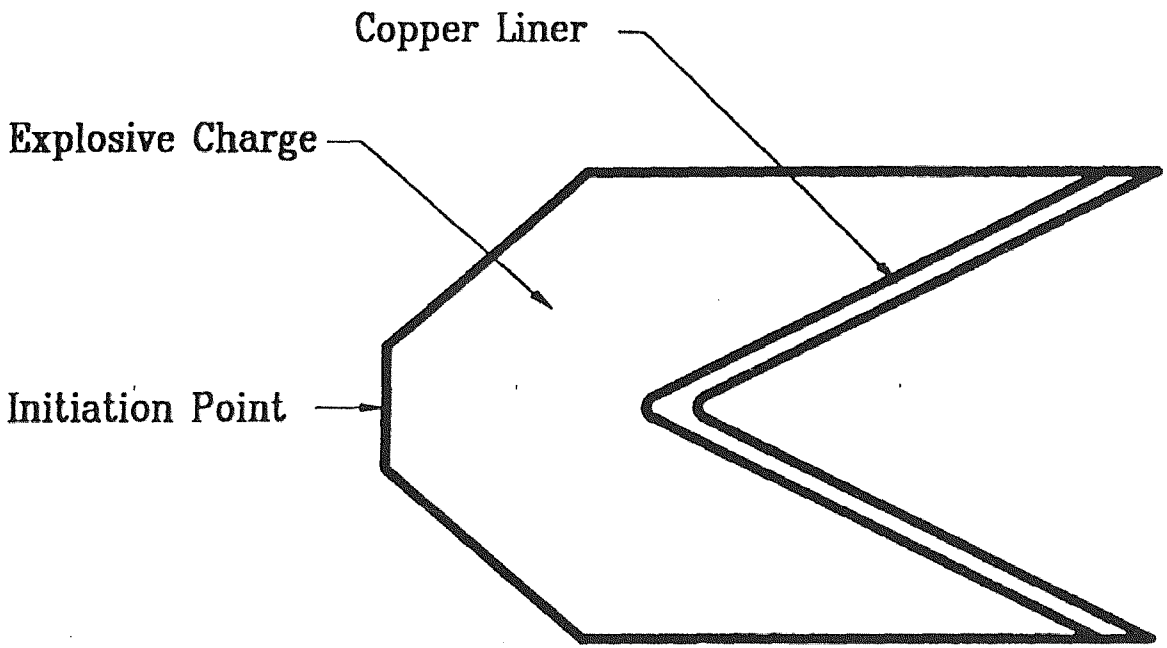

Figure 17 Typical Conical Shaped Charge Configuration

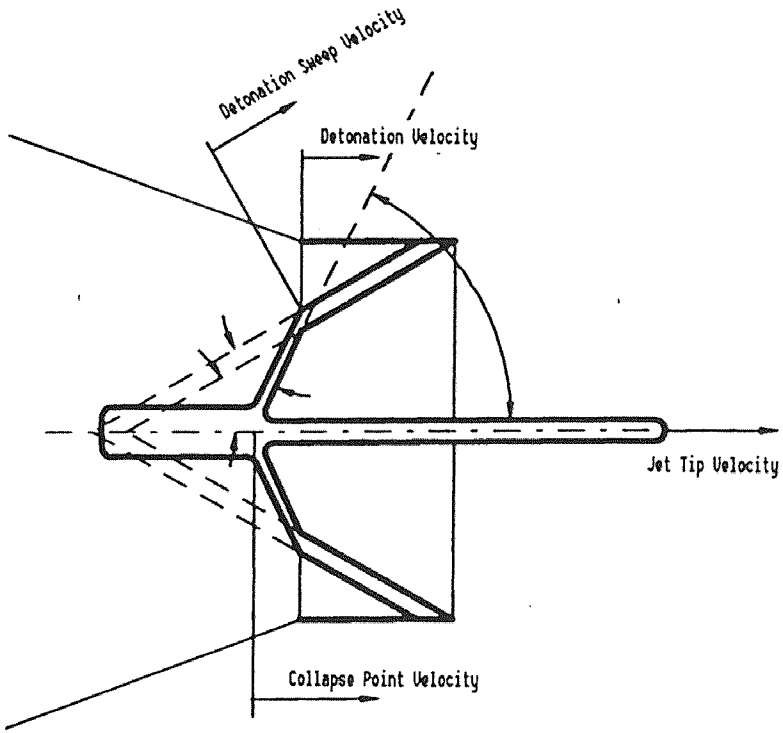

Geomerty of a Collpasing Shaped Charge

Figure 18 Typical Conical Shaped Charge Collapse

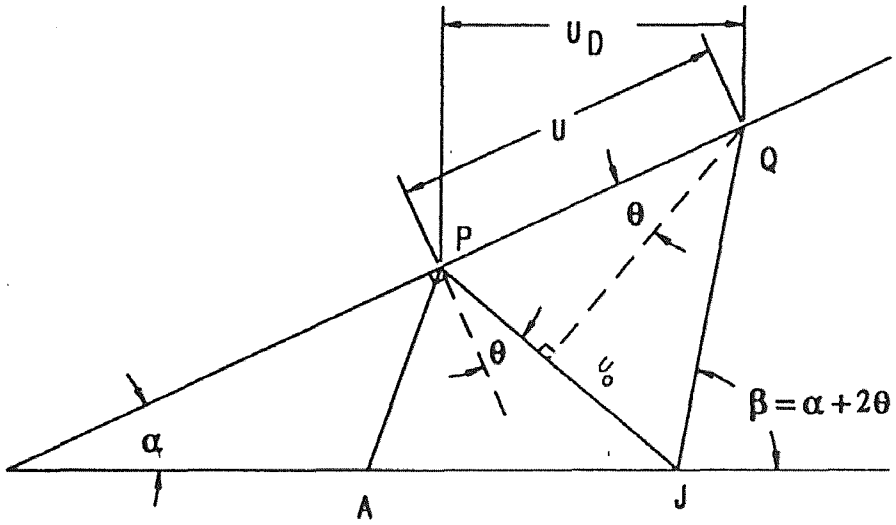

Velocity Vectors of a Collapsing Liner Element

Figure 19 Geometry of Collapsing Shaped Charge

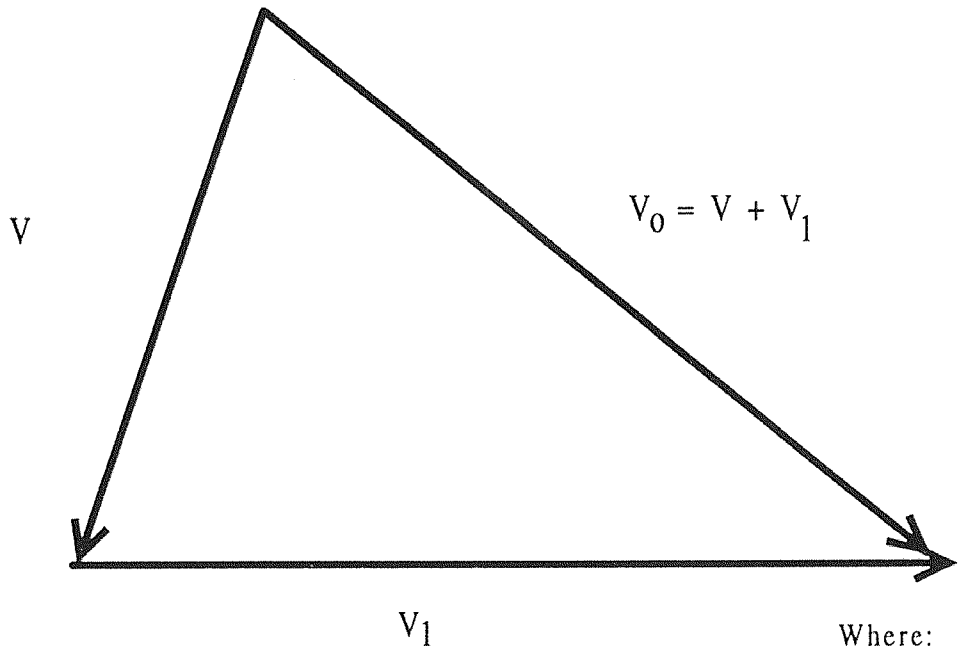

Where:

V_0 = Liner Collapse Velocity

V_1 = Collpase Velocity Relative to the Collpase Point

V = Collision Point Velocity

Figure 20 Vector Diagram at the Collapse Point

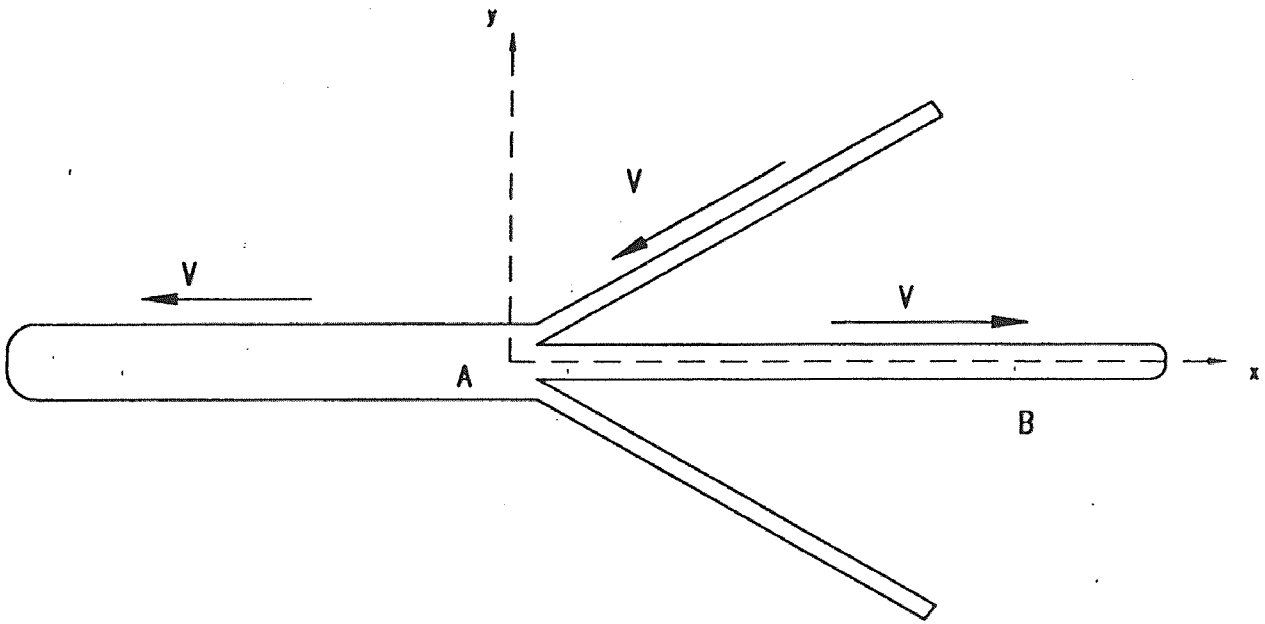

Figure 21 Formation of the Jet and Slug in Relation to the Collapse Point

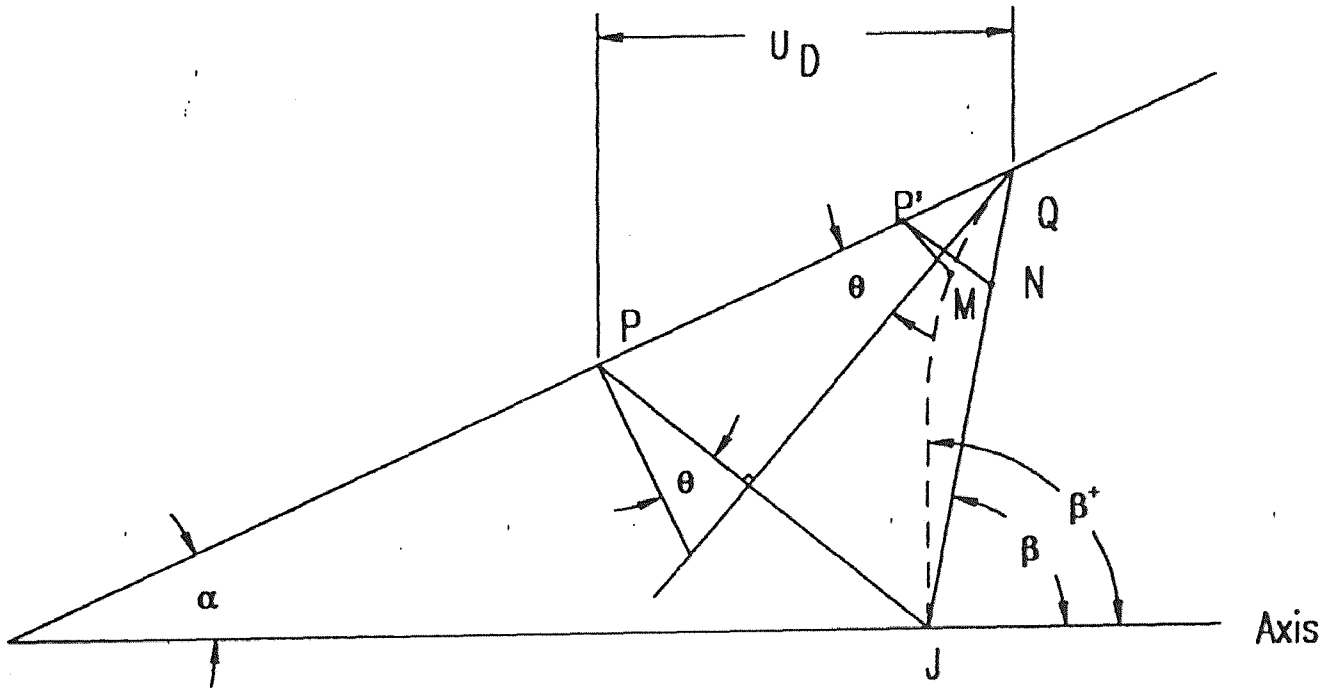

Figure 22 Geometry of Collapsing Shaped Charge for Variable Collapse Velocities

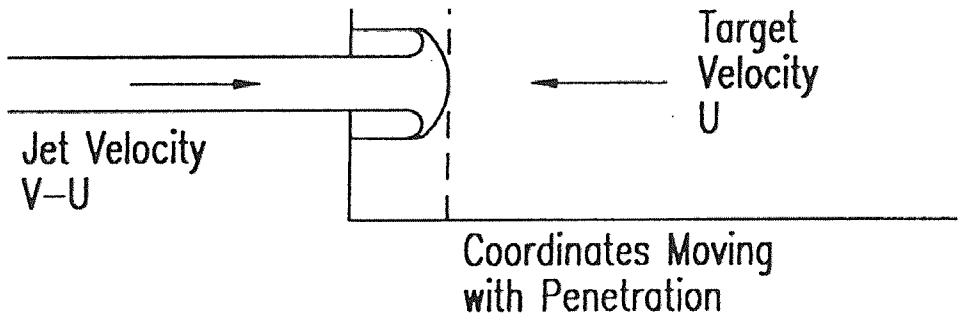

Figure 23 Jet Penetration for Jet Velocity V and Penetration Velocity U

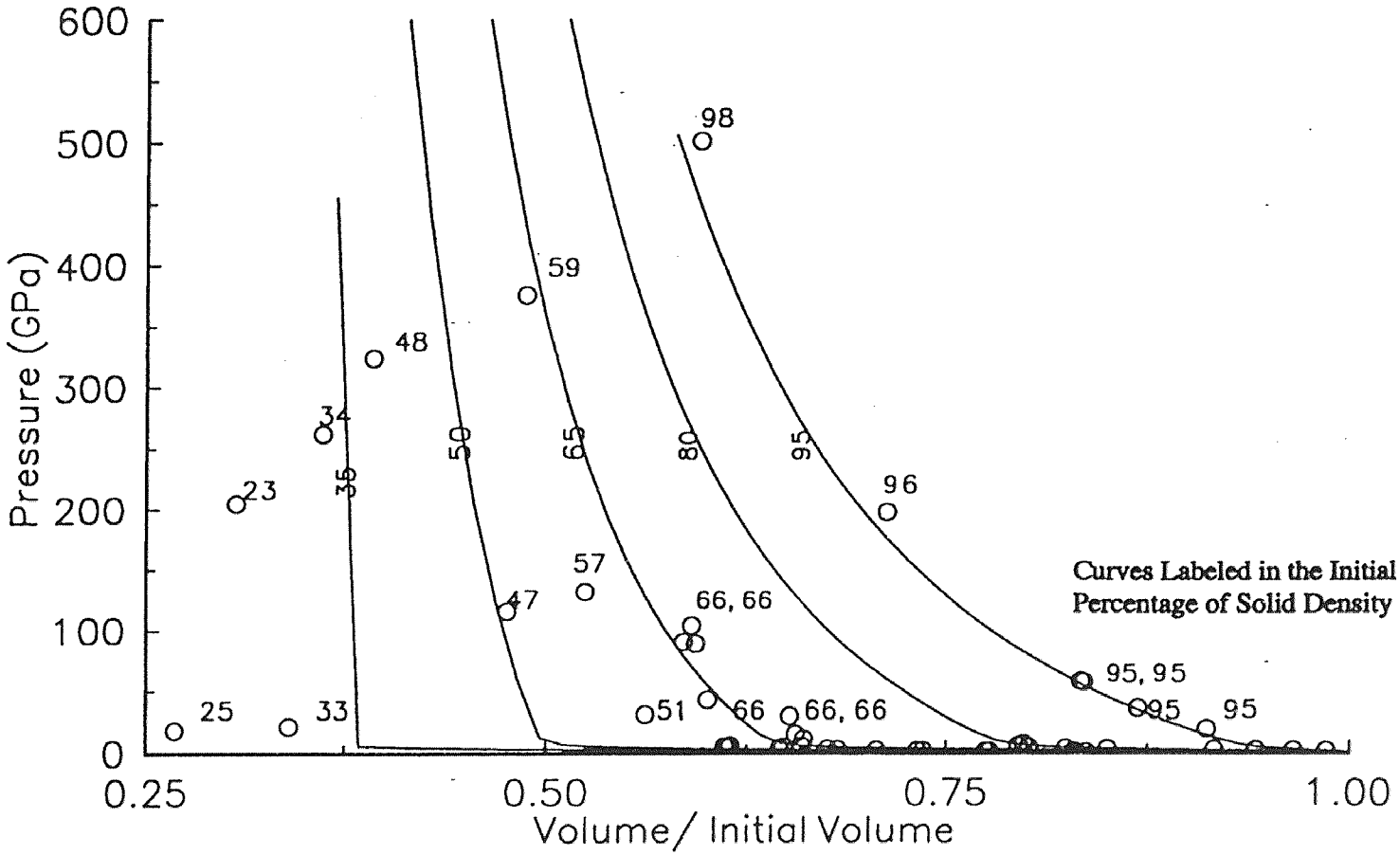

Figure 24 Shock Compaction of Porous Tungsten

Approximate Oh- Persson Equation of State

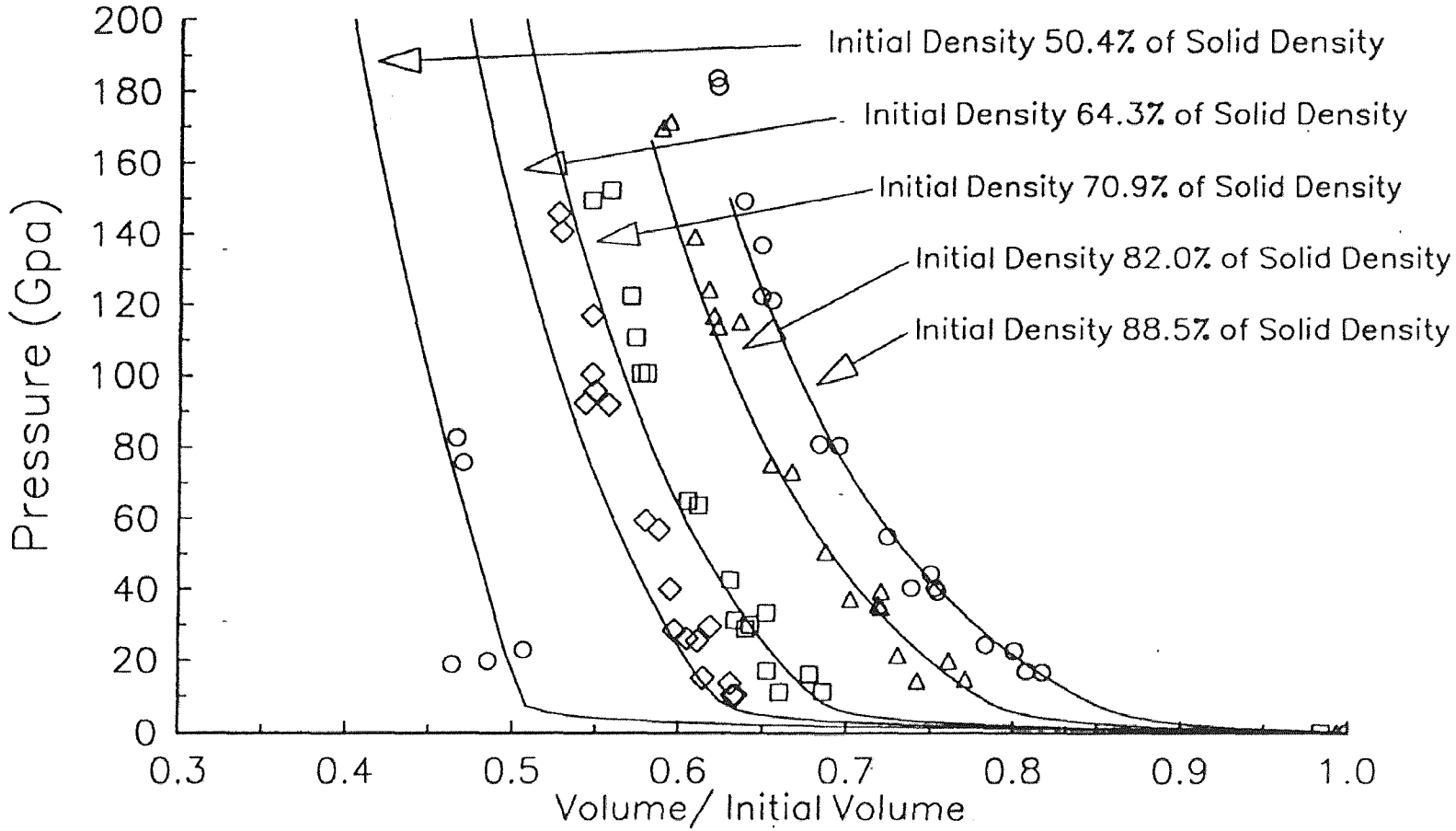

Figure 25 Shock Compaction of Porous Copper
Approximate Oh- Persson Equation of State

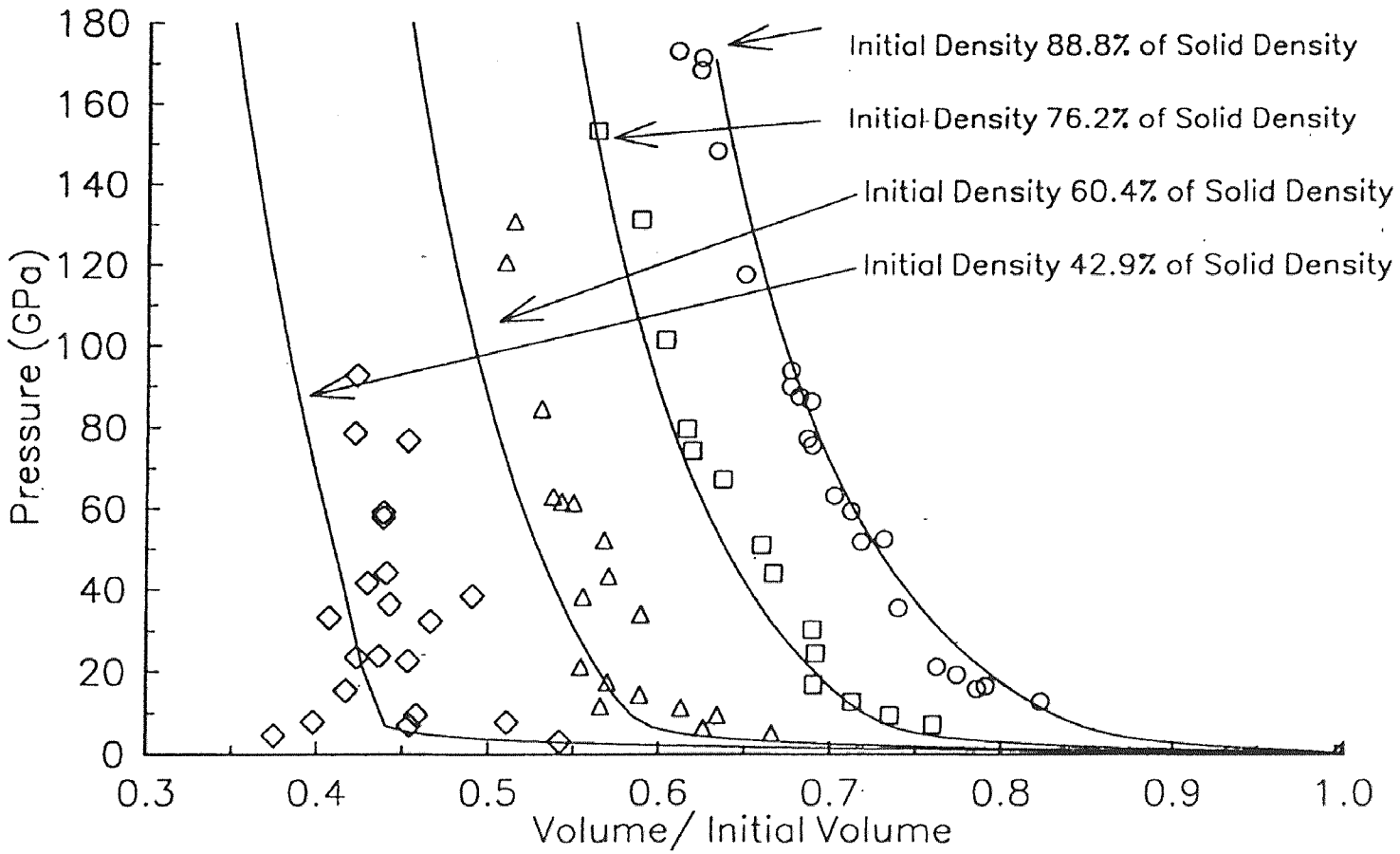

Figure 26 Shock Compaction of Porous Iron
Approximate Oh- Persson Equation of State

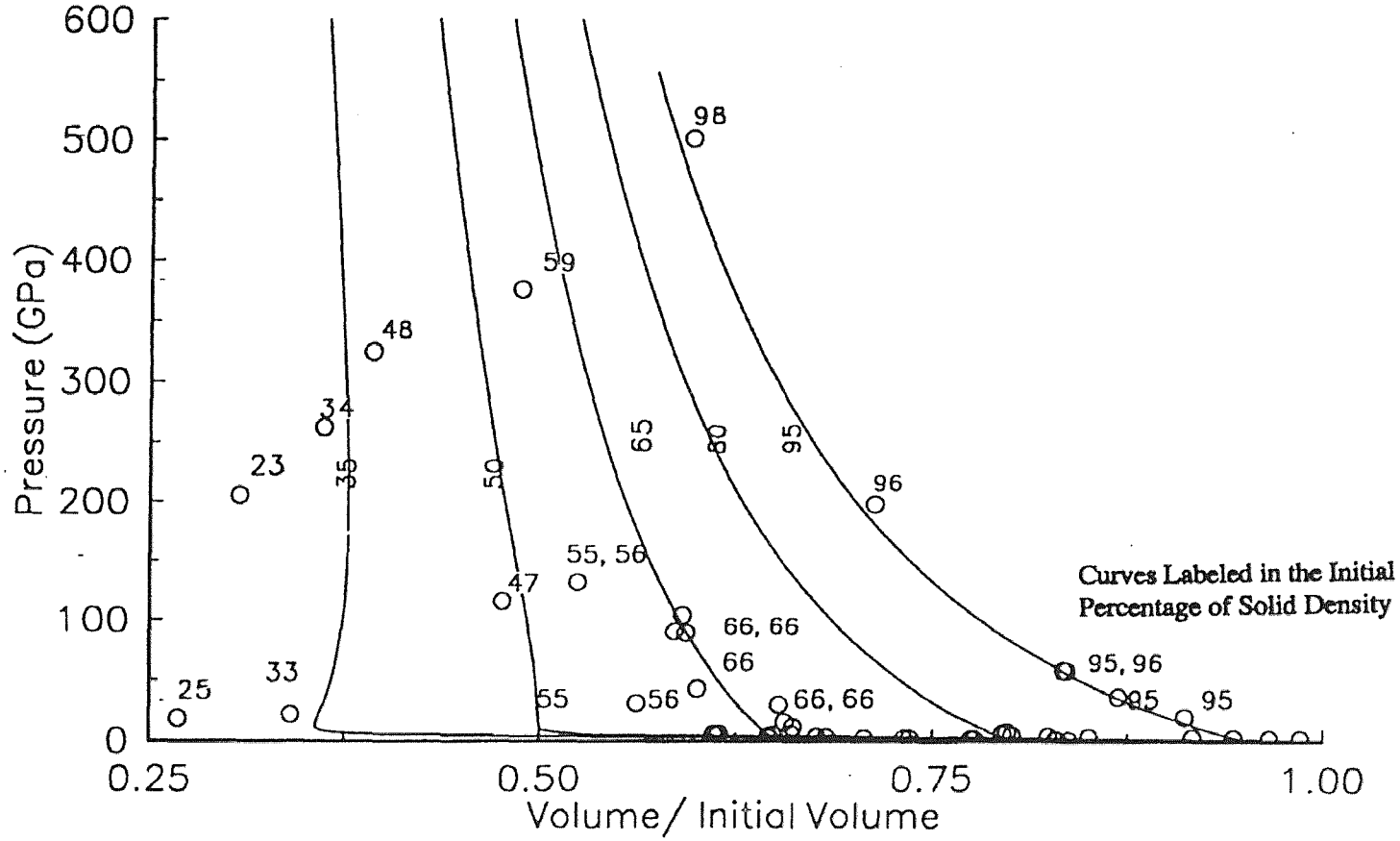

Figure 27 Shock Compaction of Porous Tungsten

Proposed Equation of State Compared to Shock Data

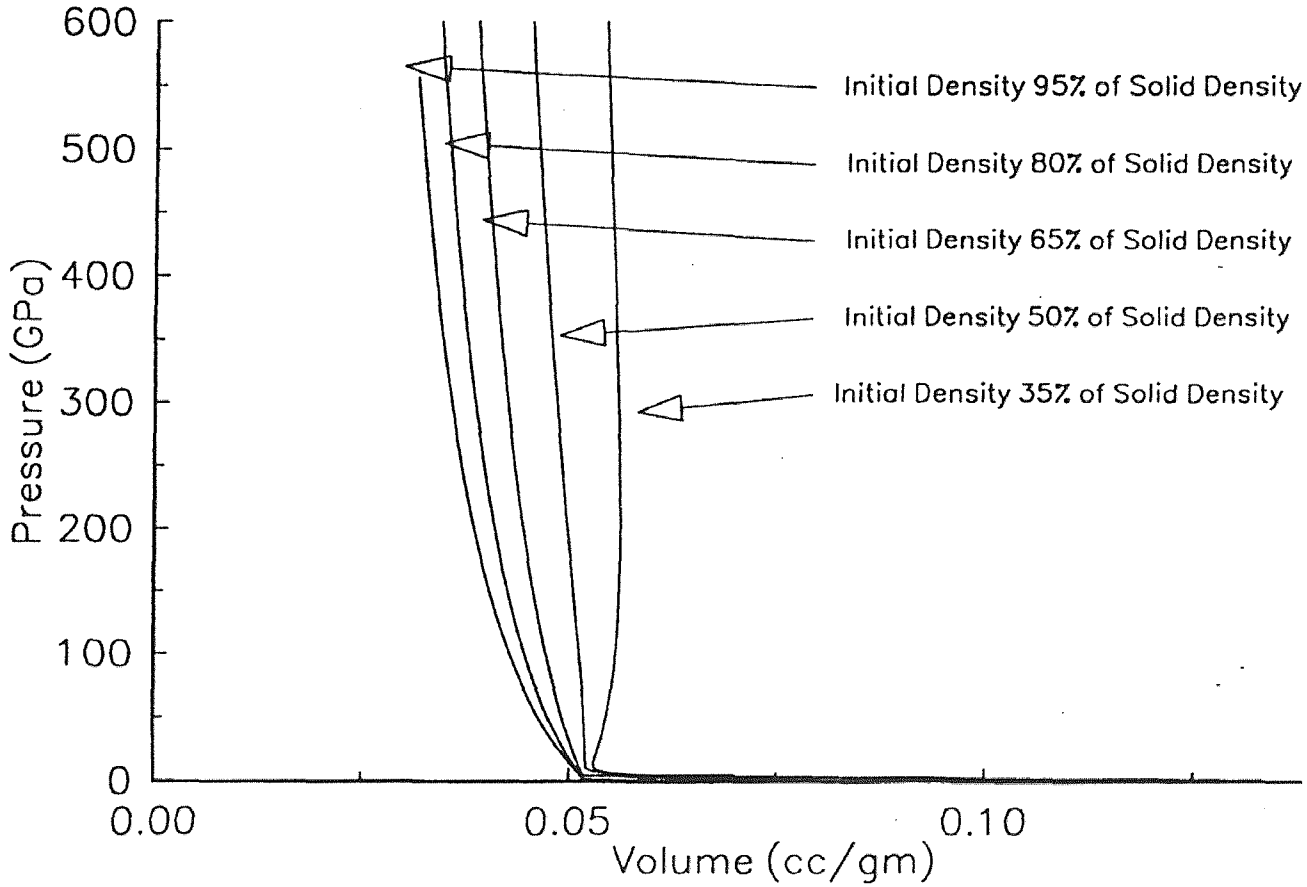

Figure 28 Shock Compaction of Porous Tungsten
Proposed Equation of State on the Pressure Volume Plane

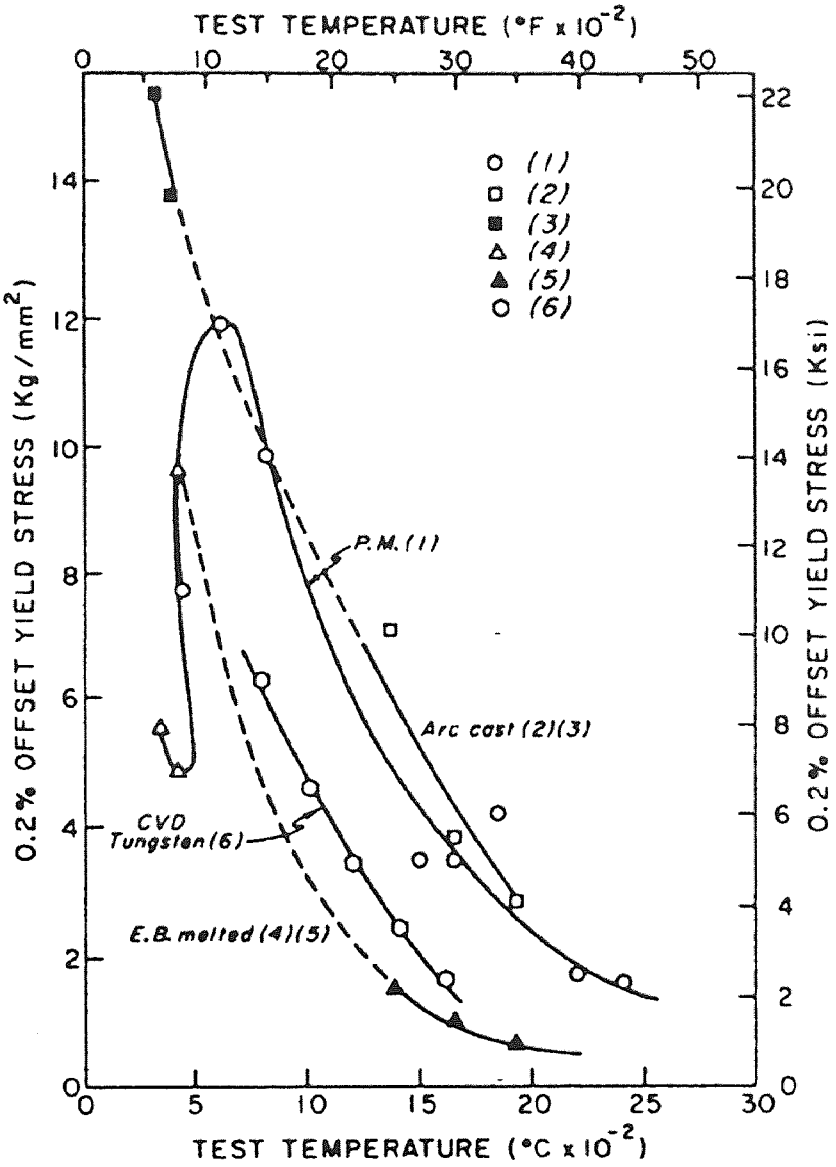

Figure 29 Yield Stress of Tungsten
from Ref. (49)

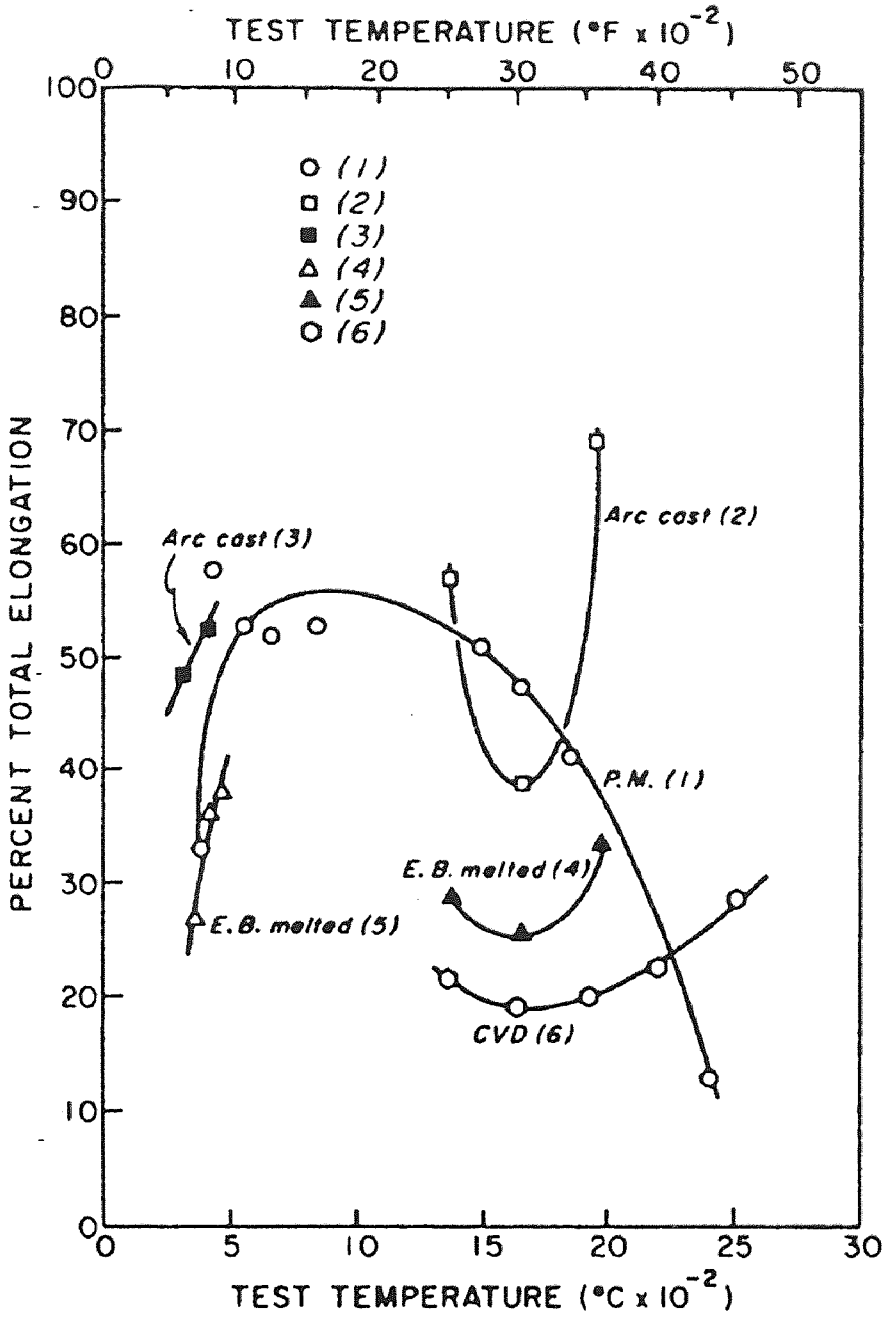

Figure 30 Percent Total Elongation of Tungsten from Ref. (49)

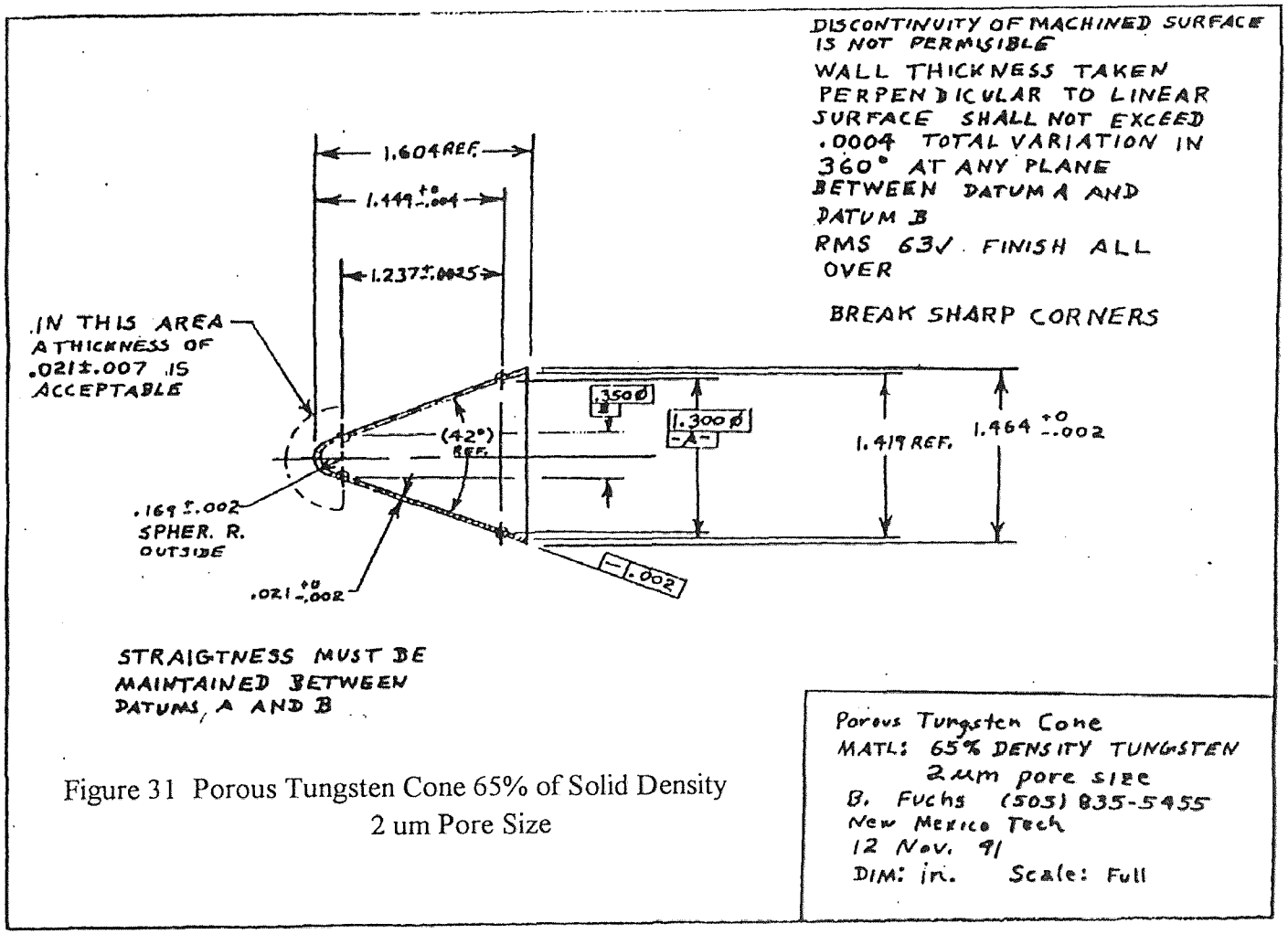

Figure 31 Porous Tungsten Cone 65% of Solid Density
2 um Pore Size

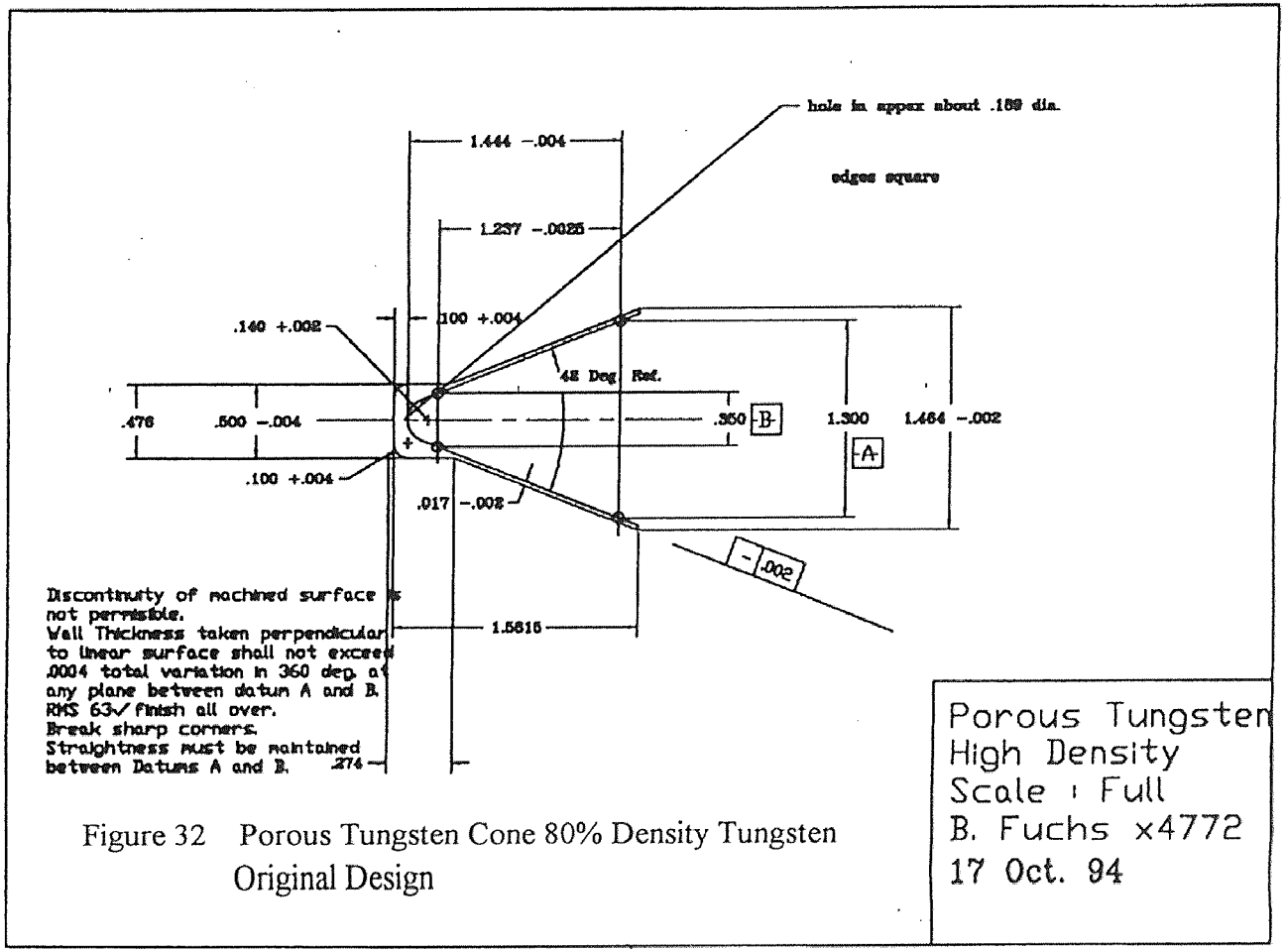

Figure 32 Porous Tungsten Cone 80% Density Tungsten Original Design

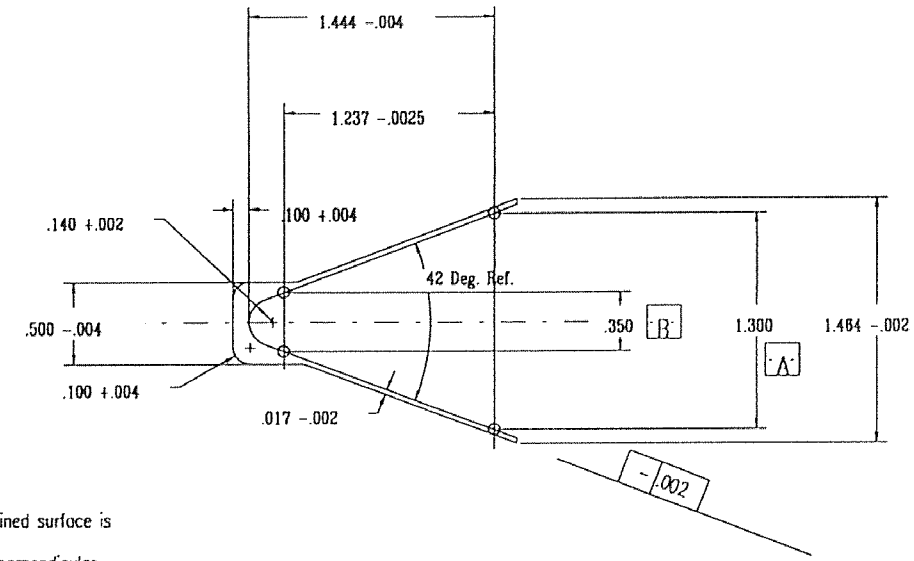

Discontinuity of machined surface is not permisible.
Wall Thickness taken perpendicular to linear surface shall not exceed .0004 total variation in 360 deg. at any plane between datum A and B.
RMS 63 finish all over.
Break sharp corners.
Straightness must be maintained between Datums A and B.

Figure 33 Porous Tungsten Cone 80% Density Modified Design

Porous Tungsten
High Density
Scale : Full
B. Fuchs x4772
17 Oct. 94

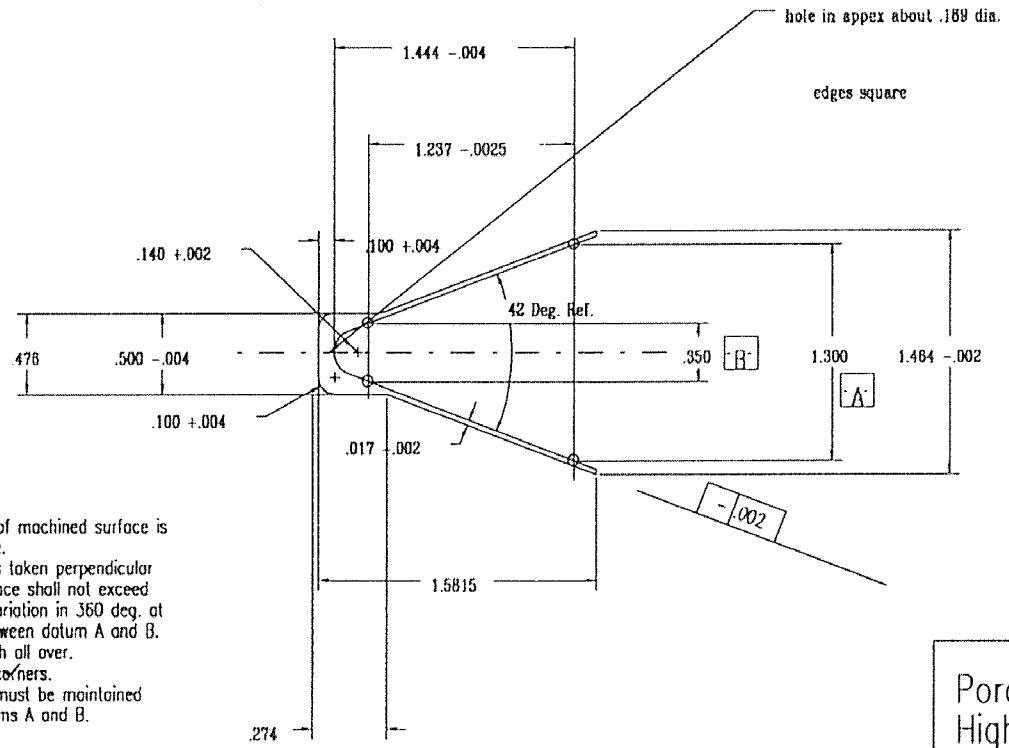

Discontinuity of machined surface is not permisible.
Wall Thickness taken perpendicular to linear surface shall not exceed .0004 total variation in 360 deg. at any plane between datum A and B.
RMS 63 finish all over.
Break sharp corners.
Straightness must be maintained between Datums A and B.

Porous Tungsten
High Density
Scale : Full
B. Fuchs x4772
17 Oct. 94

Figure 34 Porous Tungsten Cone 80% Density Final Design

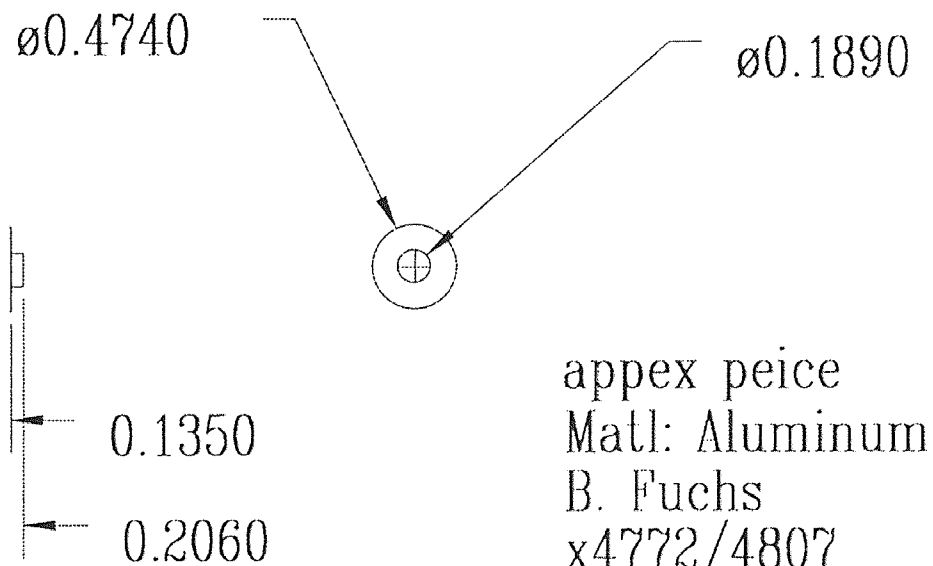

Figure 35 Aluminum Apex Cap

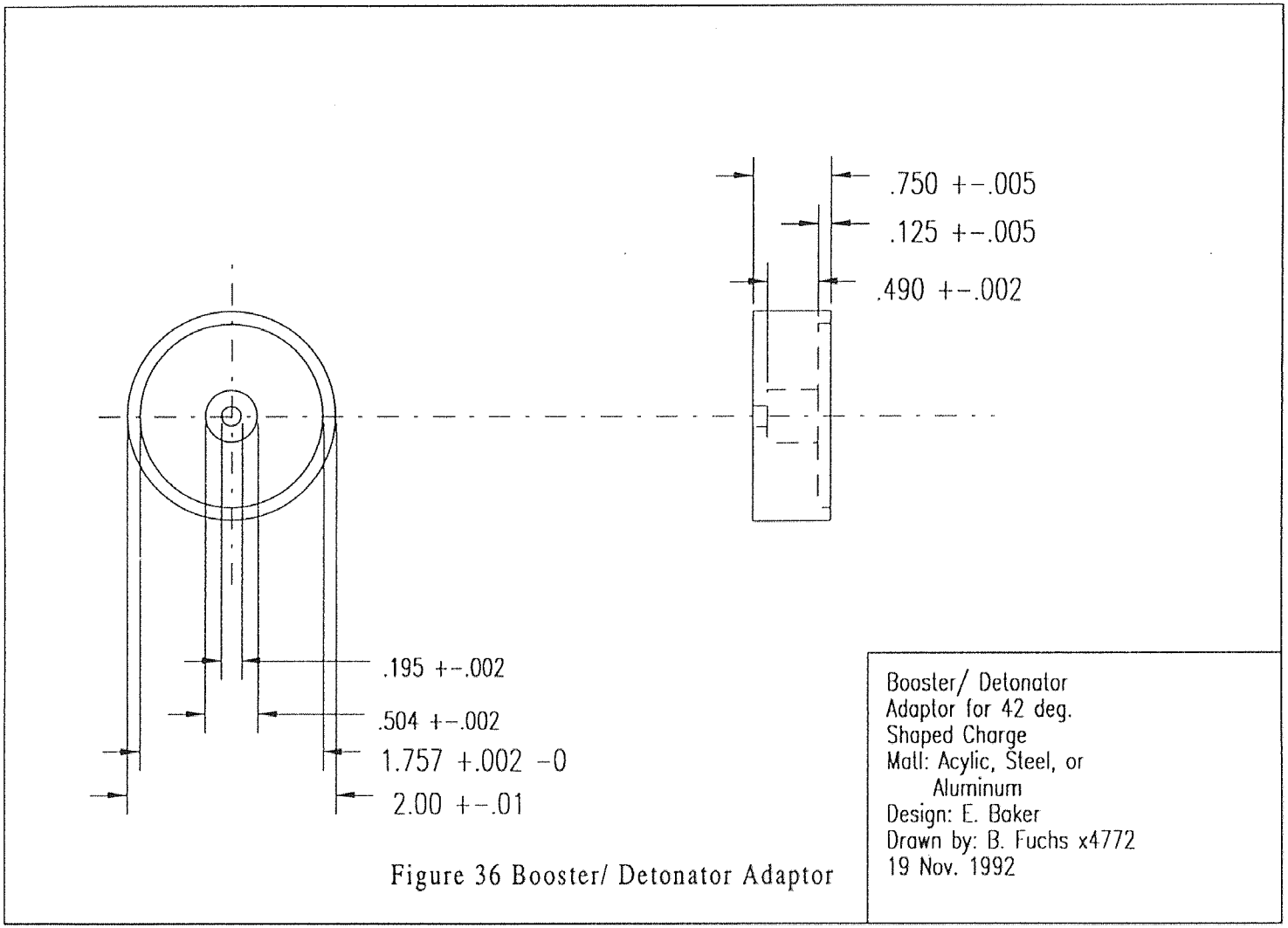

Figure 36 Booster/ Detonator Adaptor

Booster/ Detonator
Adaptor for 42 deg.
Shaped Charge
Matl: Acylic, Steel, or
Aluminum
Design: E. Baker
Drawn by: B. Fuchs x4772
19 Nov. 1992

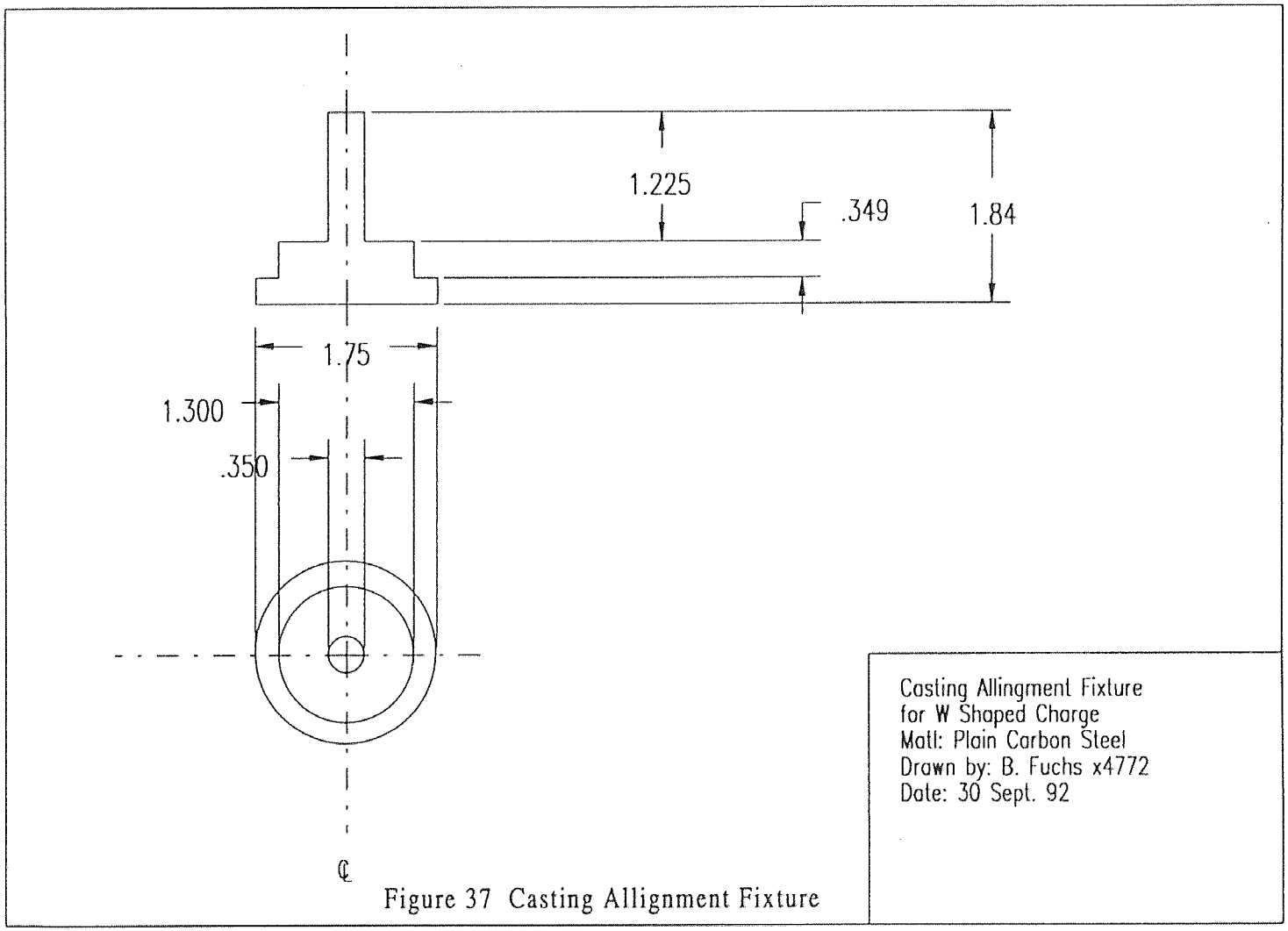

Figure 37 Casting Allignment Fixture

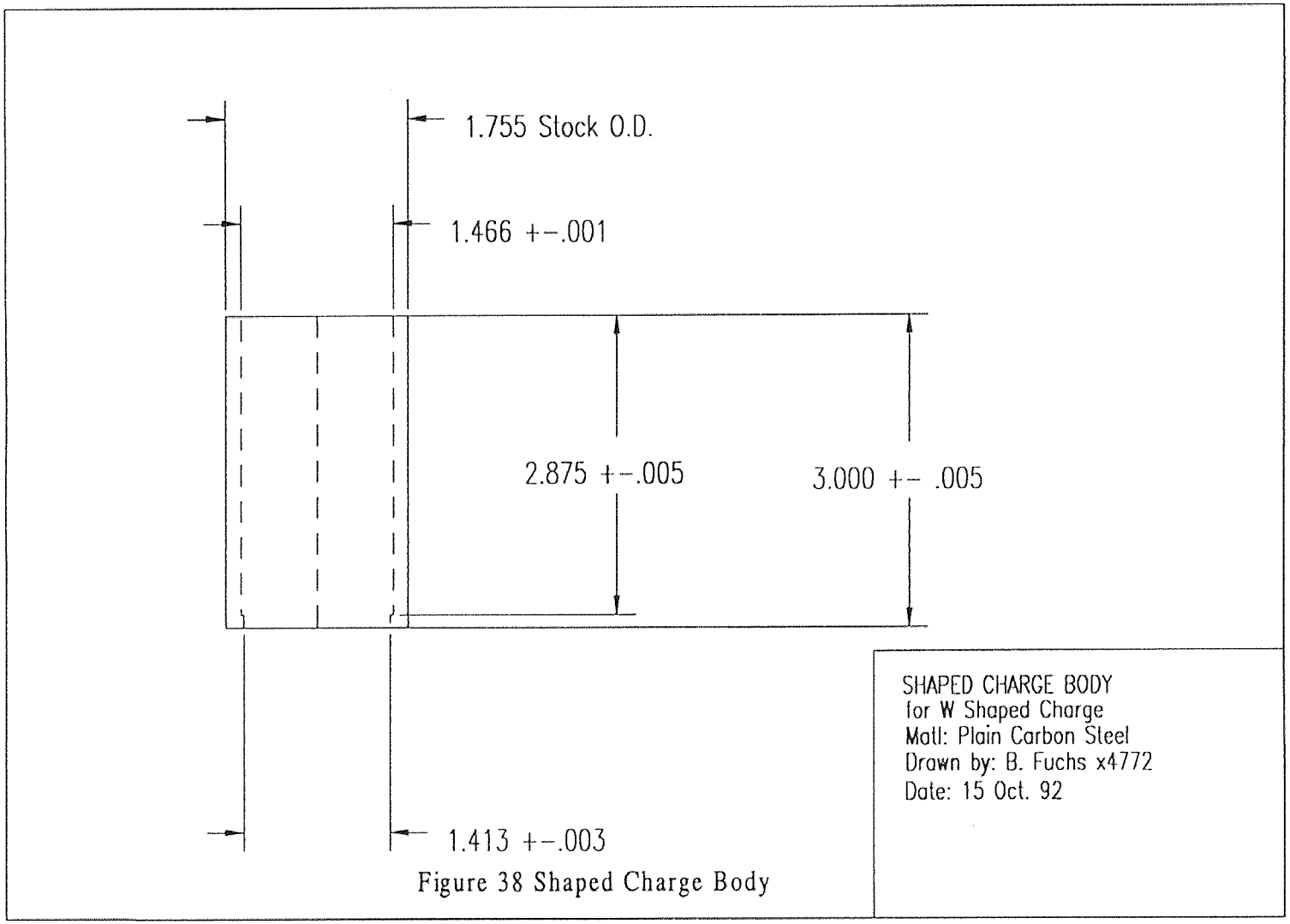

Figure 38 Shaped Charge Body

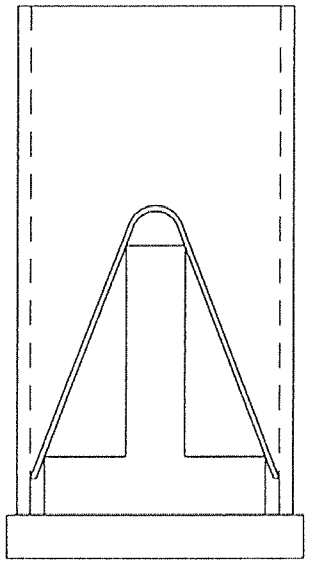

Figure 39 Assembly of Charge for Casting

Assembly of
Charge for Casting
B. Fuchs x4772
23 Sept. 92

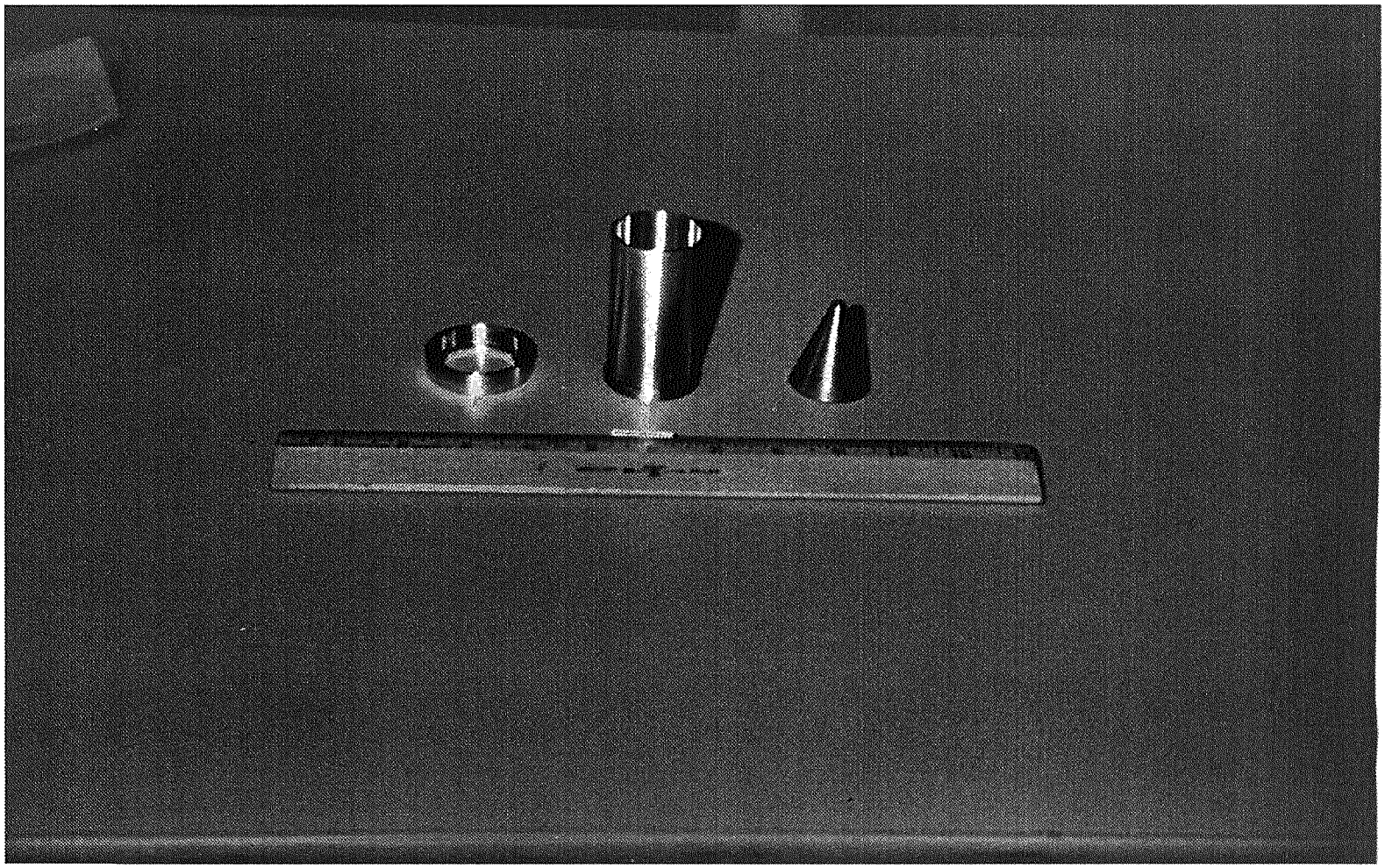

Figure 40 Shaped Charge Parts for 65% Liner

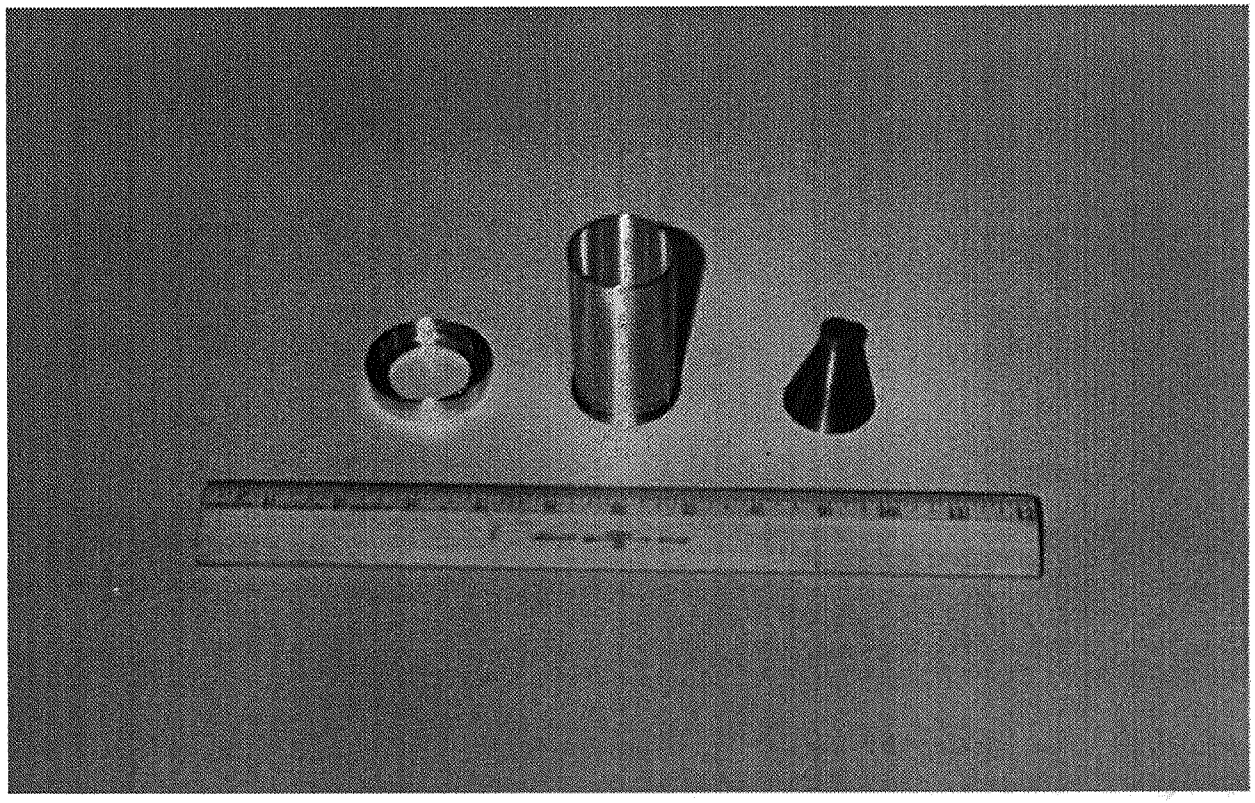

Figure 41 Shape Charge Parts for 80% Liner

Figure 42 Explosive Test Setup

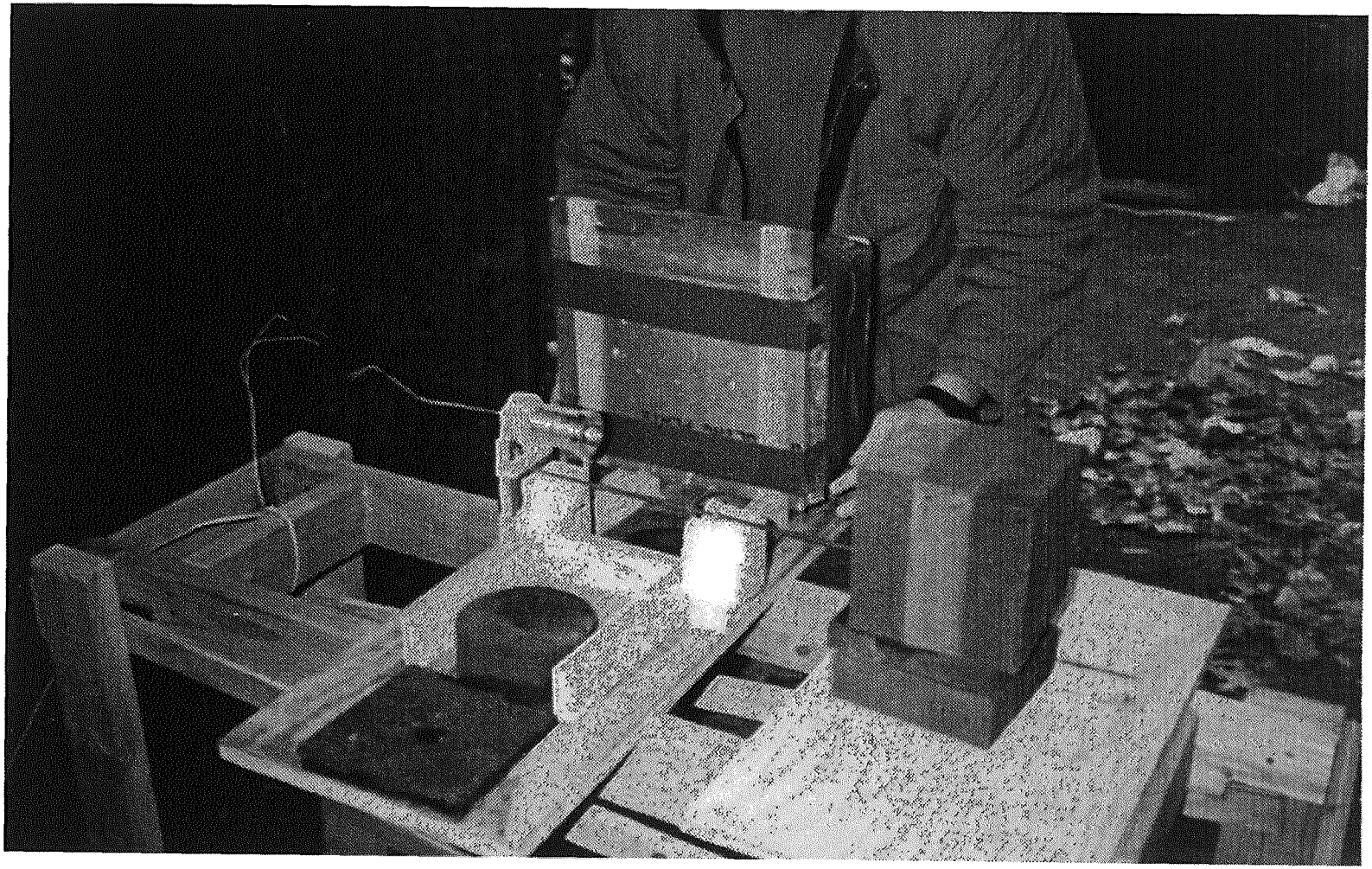

Figure 43 Placement of Radiographic Film

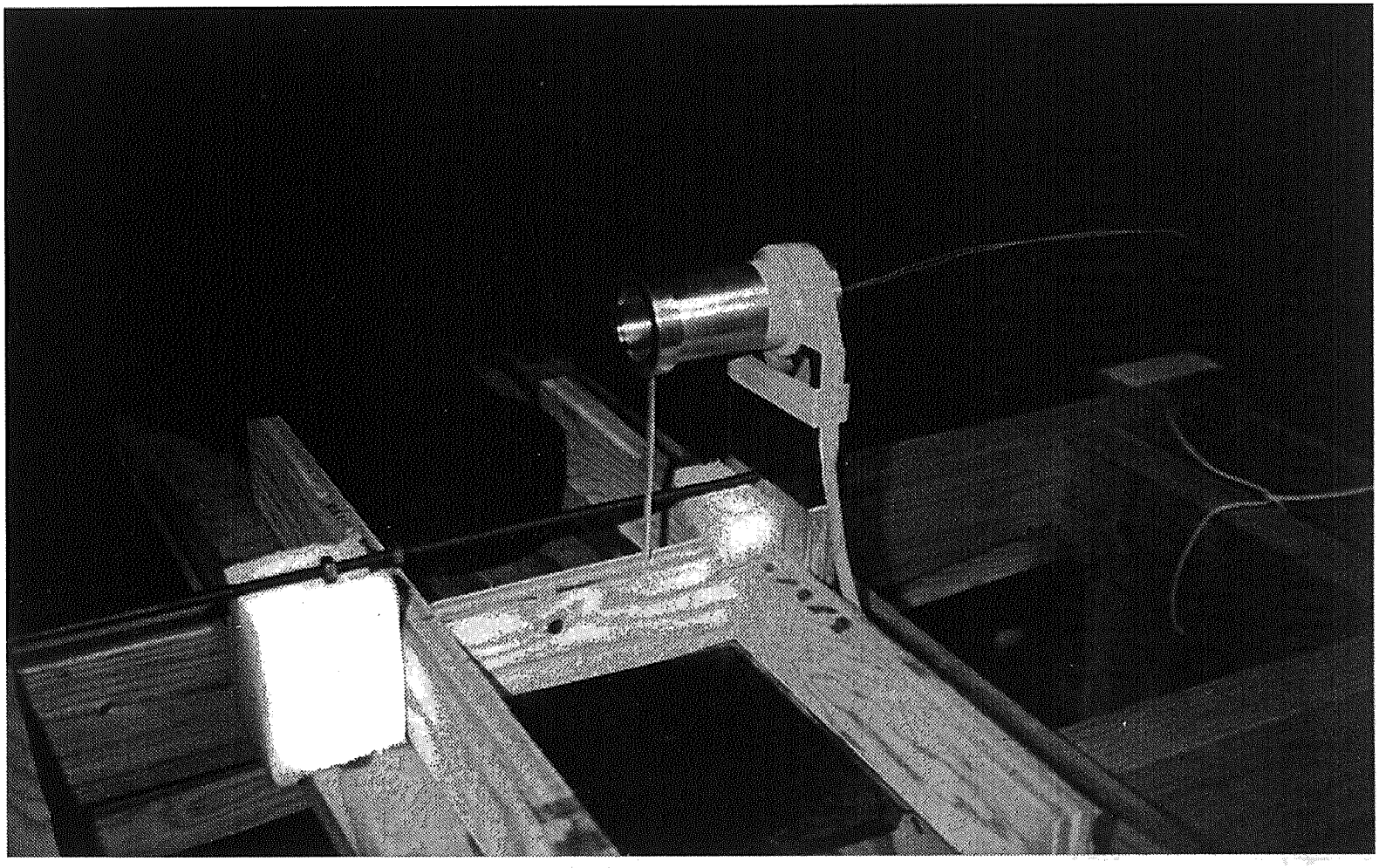

Figure 44 Shaped Charge Prior to Explosive Test

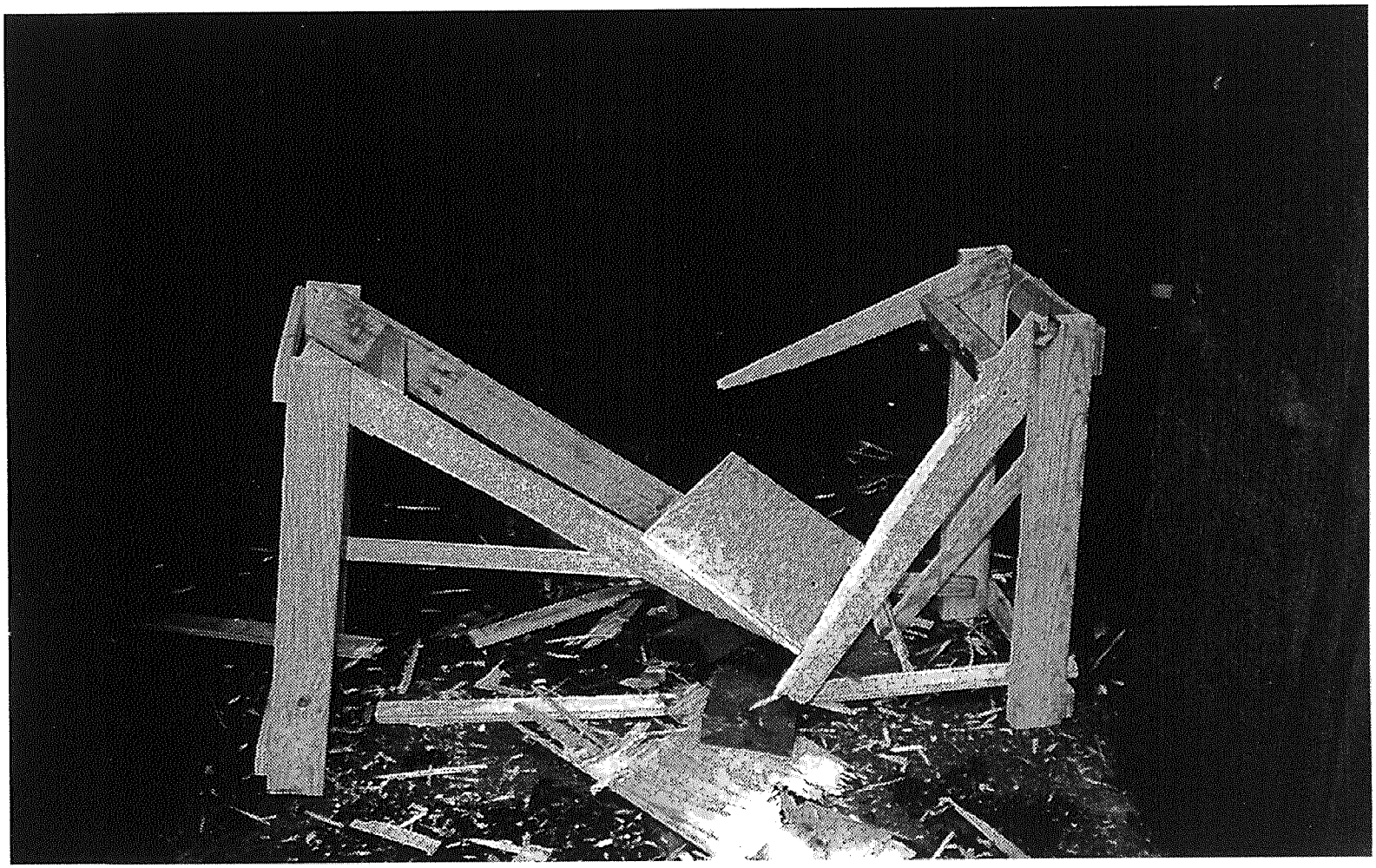

Figure 45 Test Stand After Explosive Test

Figure 46 Witness Plate After Explosive Test

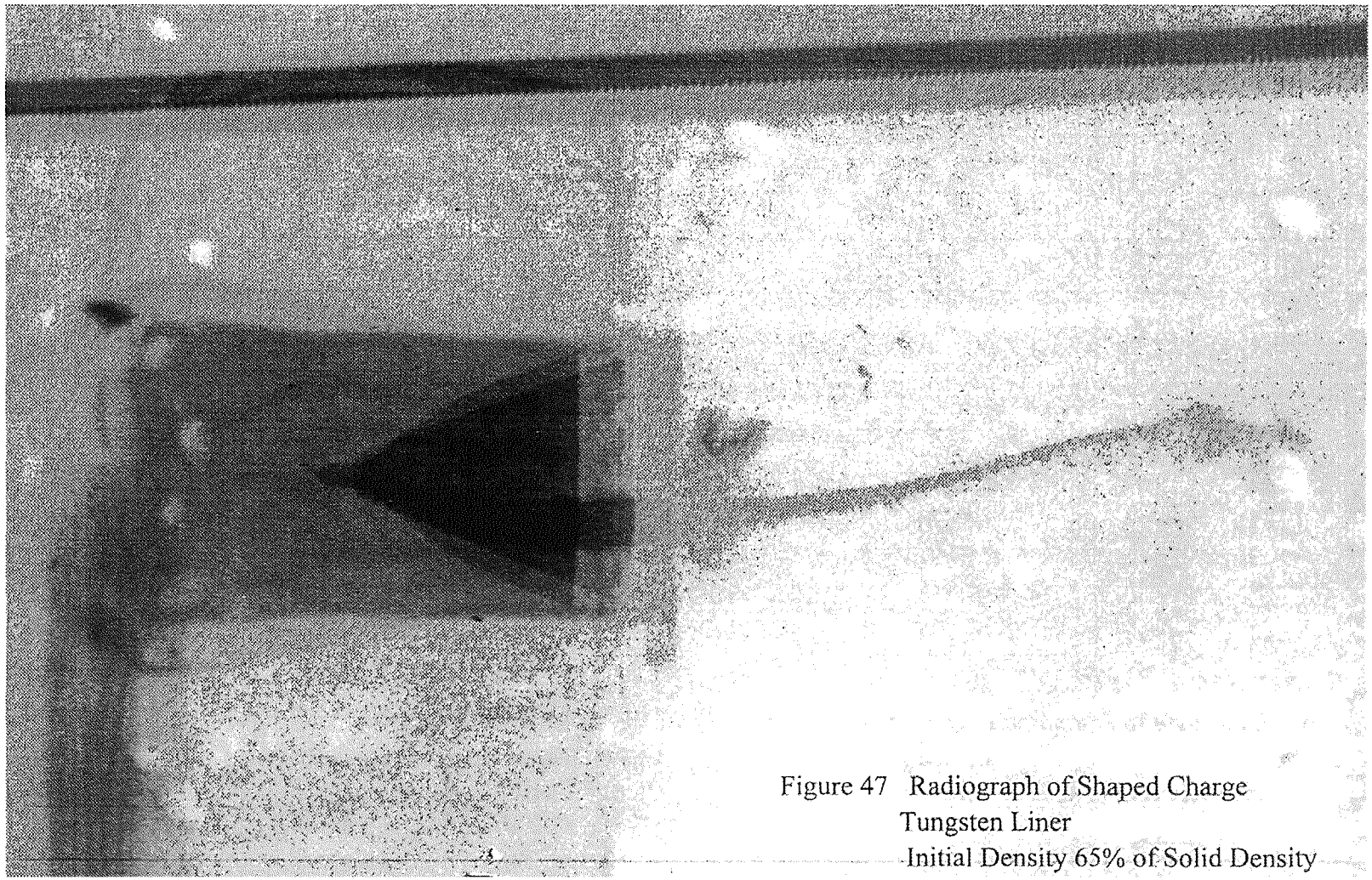

Figure 47 Radiograph of Shaped Charge
Tungsten Liner
Initial Density 65% of Solid Density

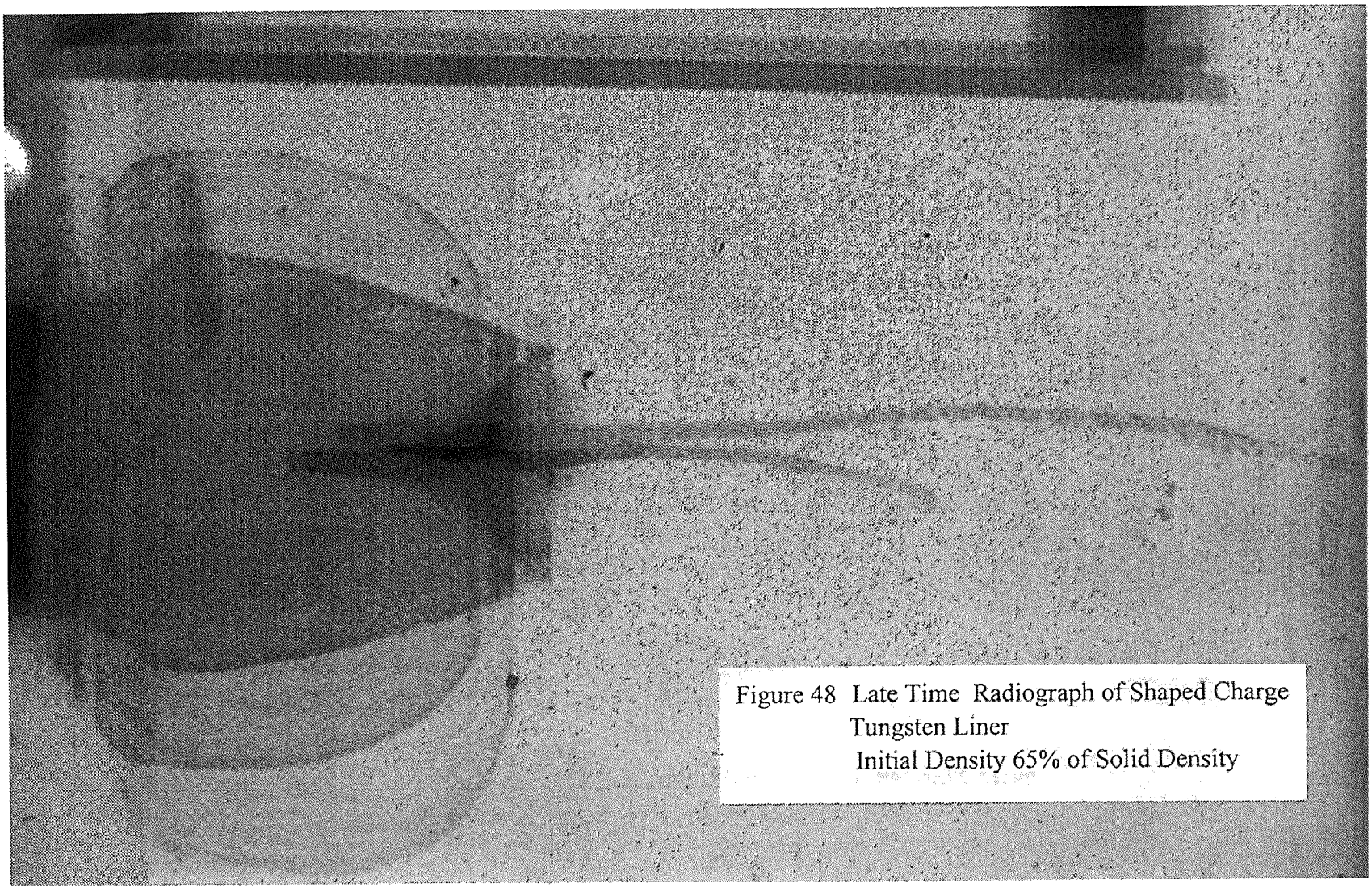

Figure 48 Late Time Radiograph of Shaped Charge
Tungsten Liner
Initial Density 65% of Solid Density

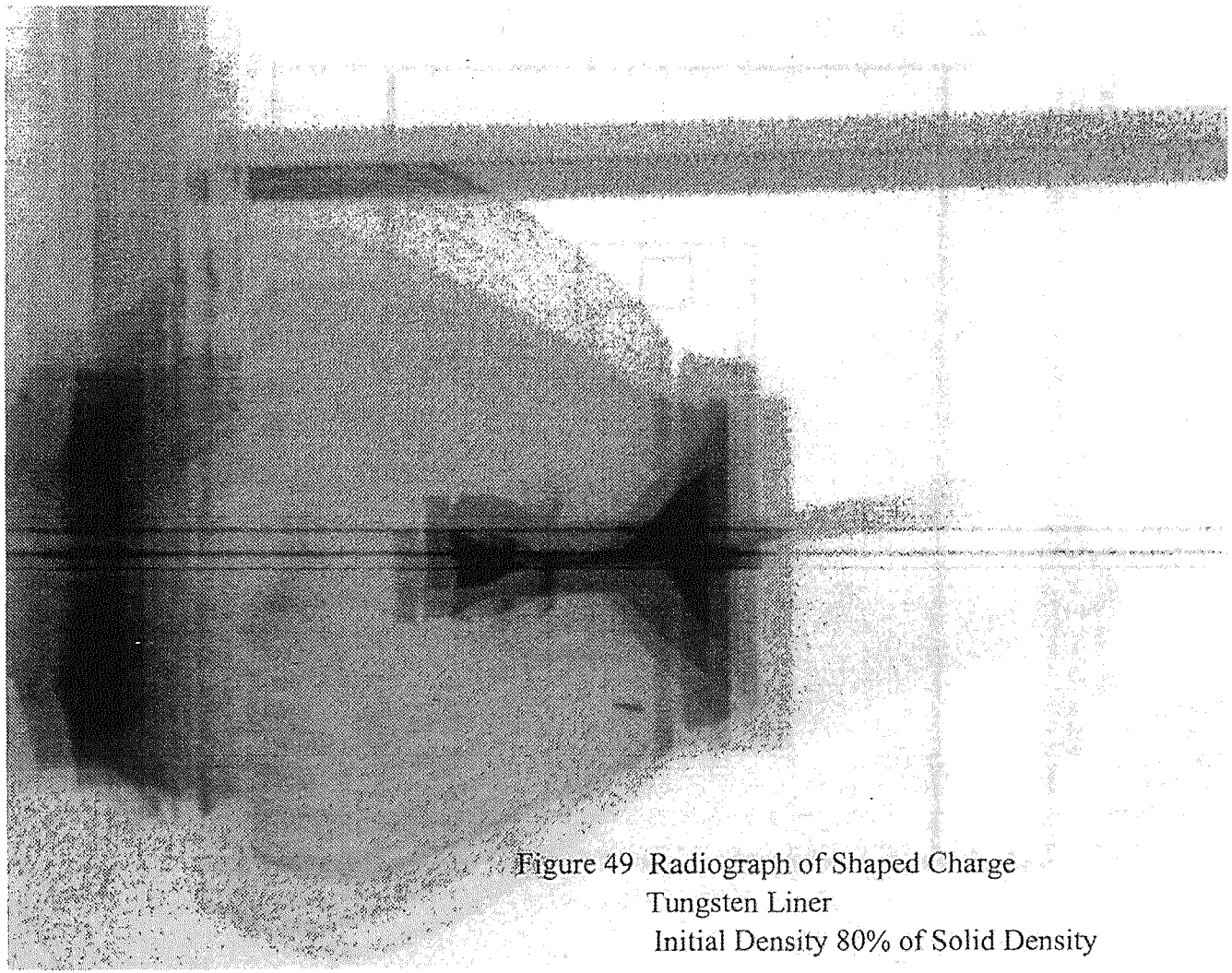

Figure 49 Radiograph of Shaped Charge
Tungsten Liner
Initial Density 80% of Solid Density

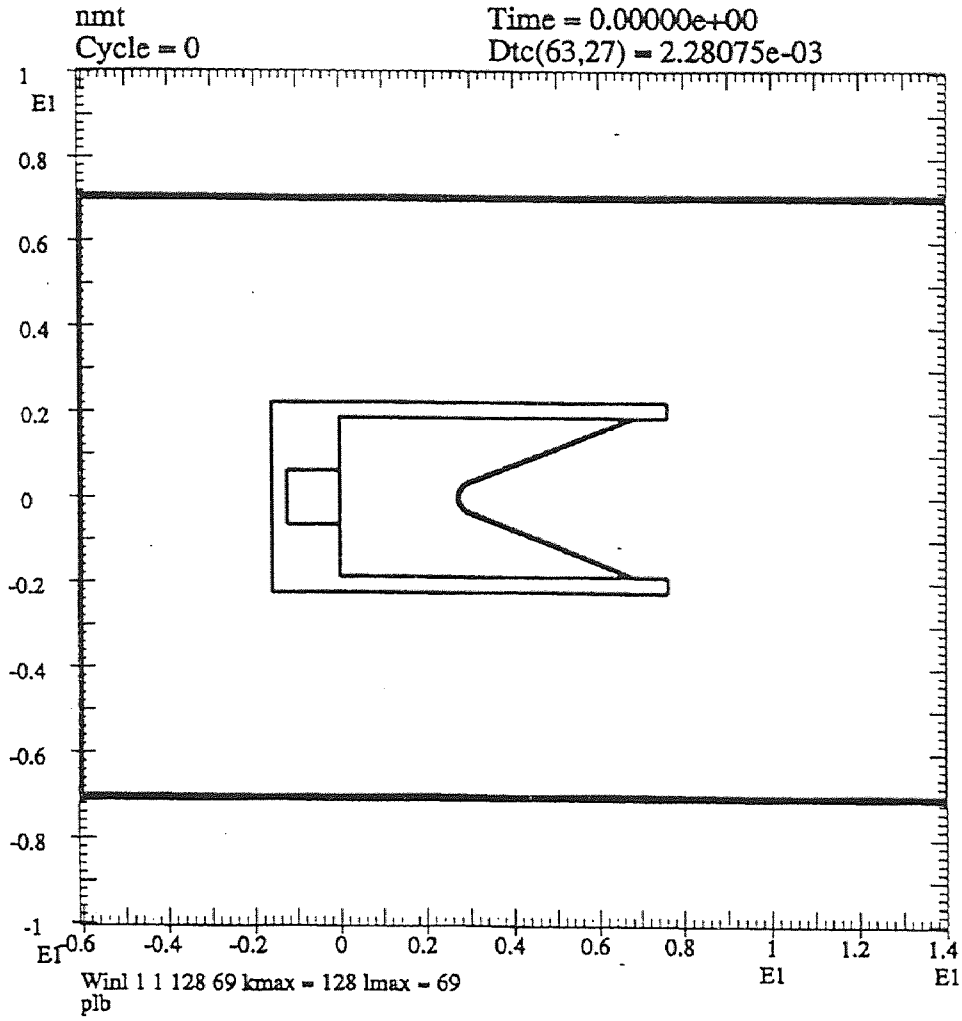

Figure 50 CALE Model Initial Configuration

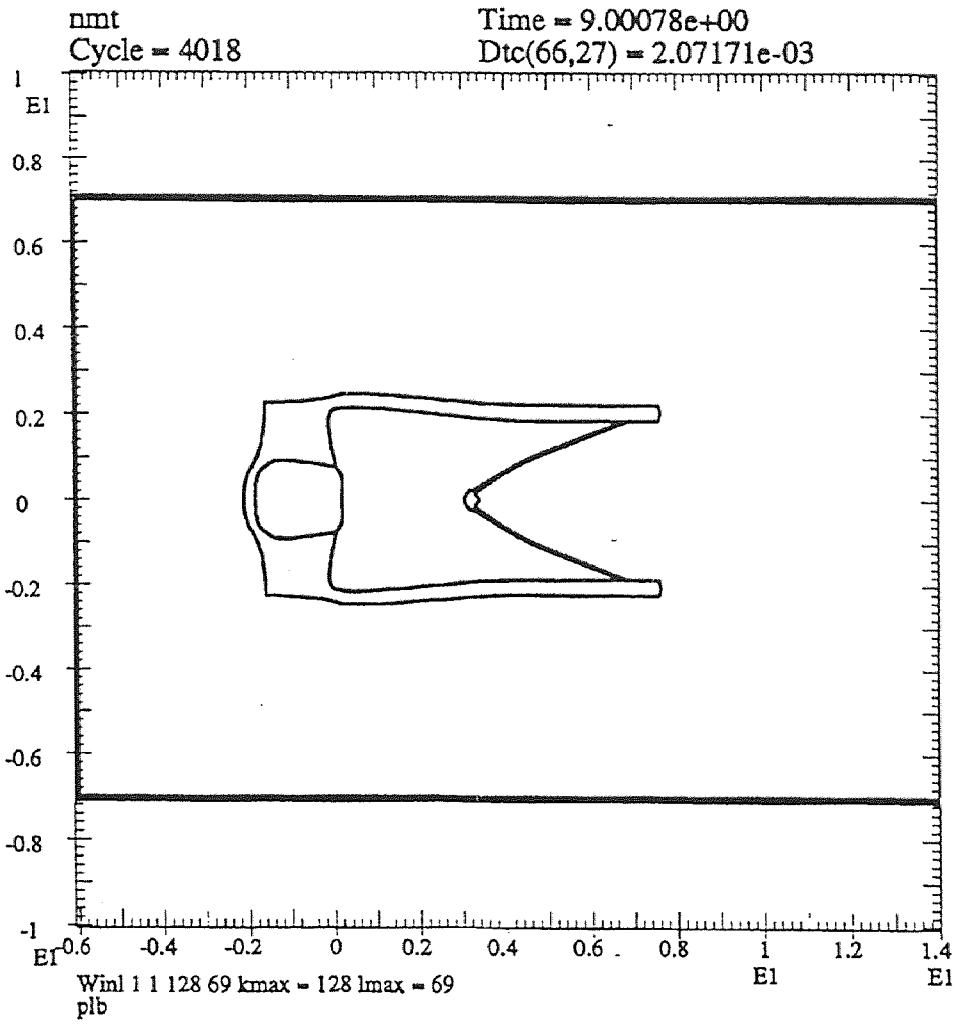

Figure 51 CALE Model at 9 μs

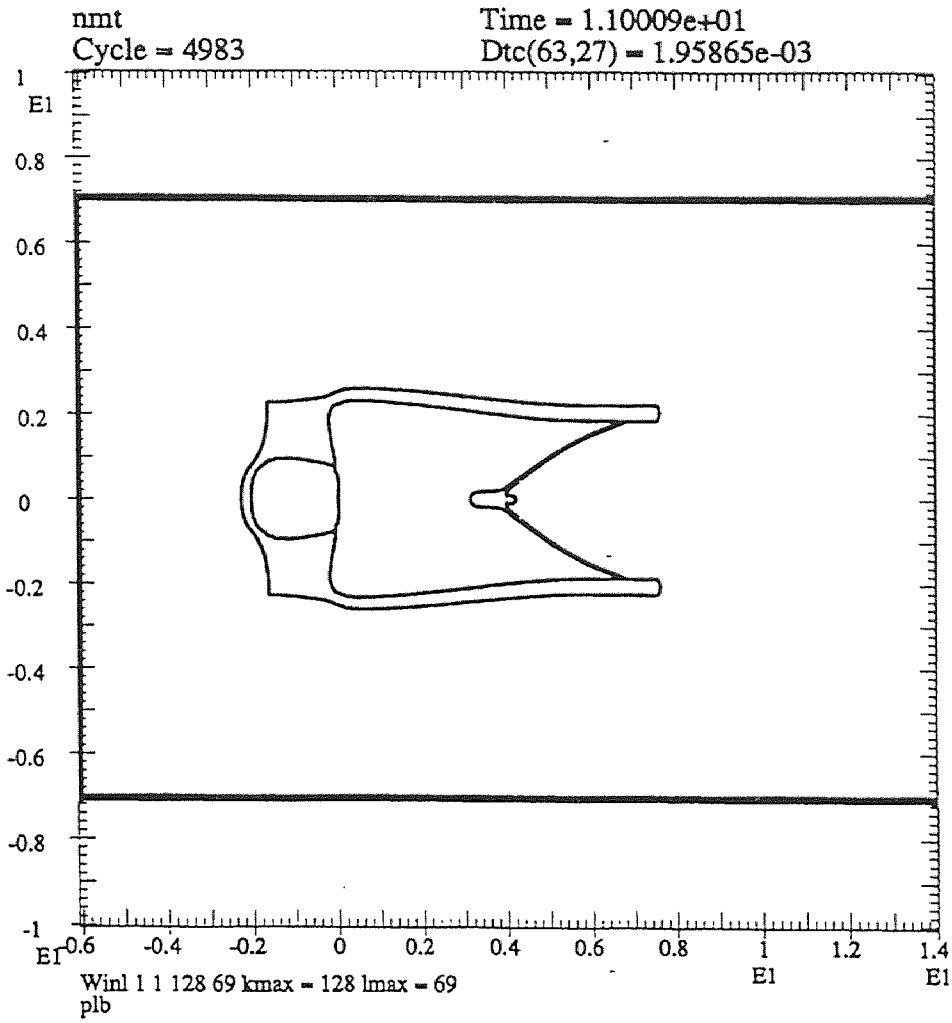

Figure 52 CALE Model at 11μs

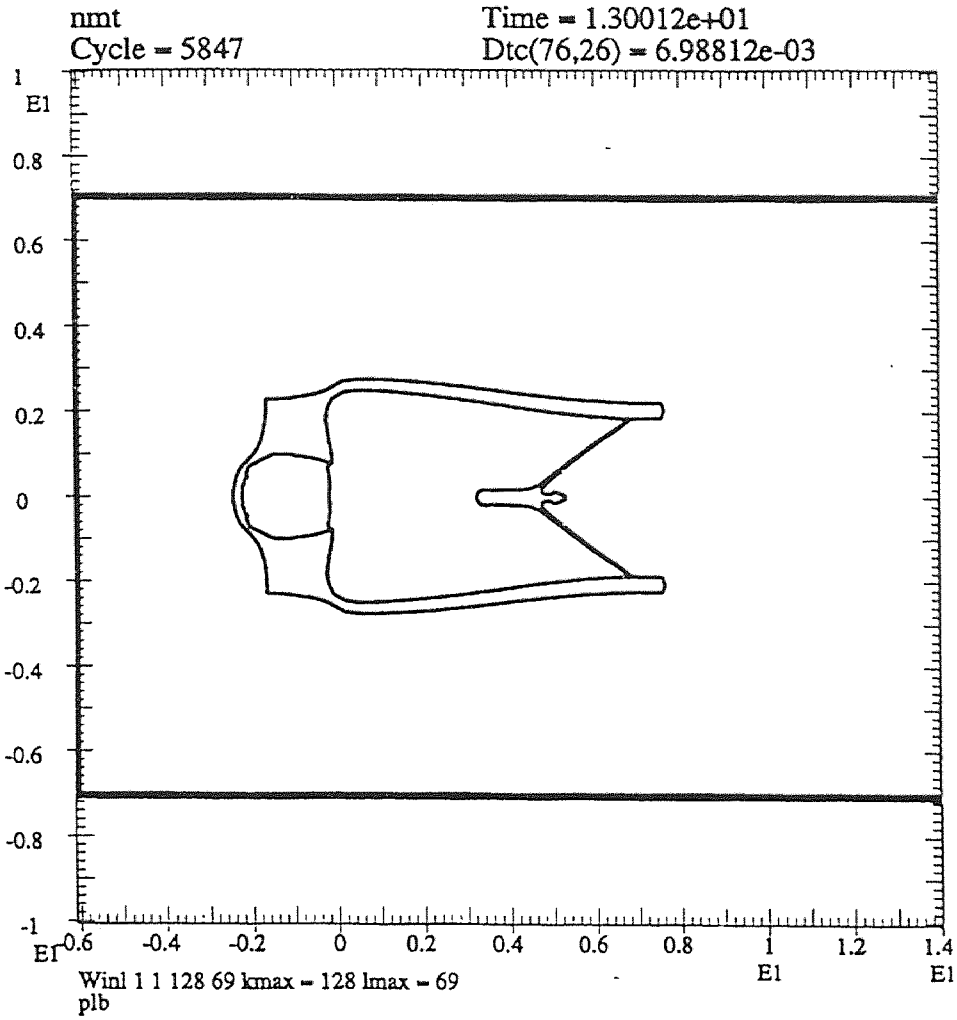

Figure 53 CALE Model at 13 μs

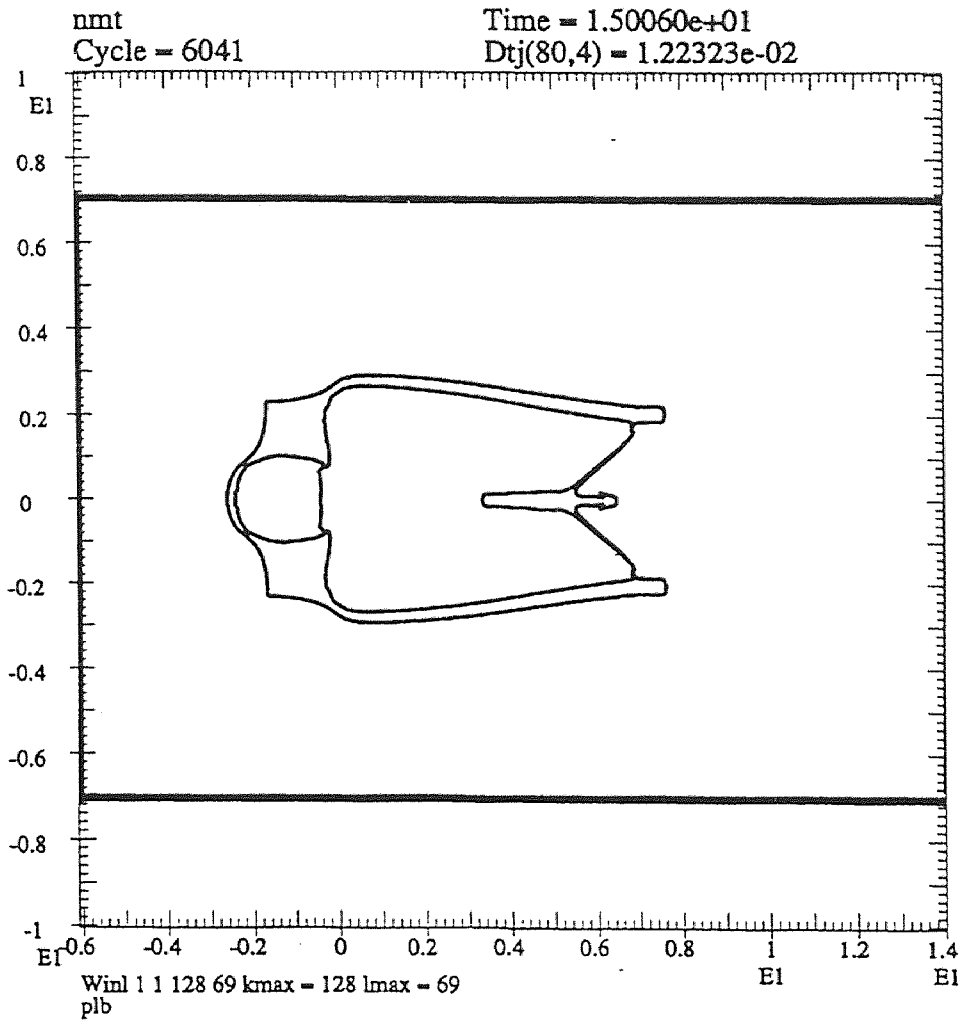

Figure 54 CALE Model at 15 μs

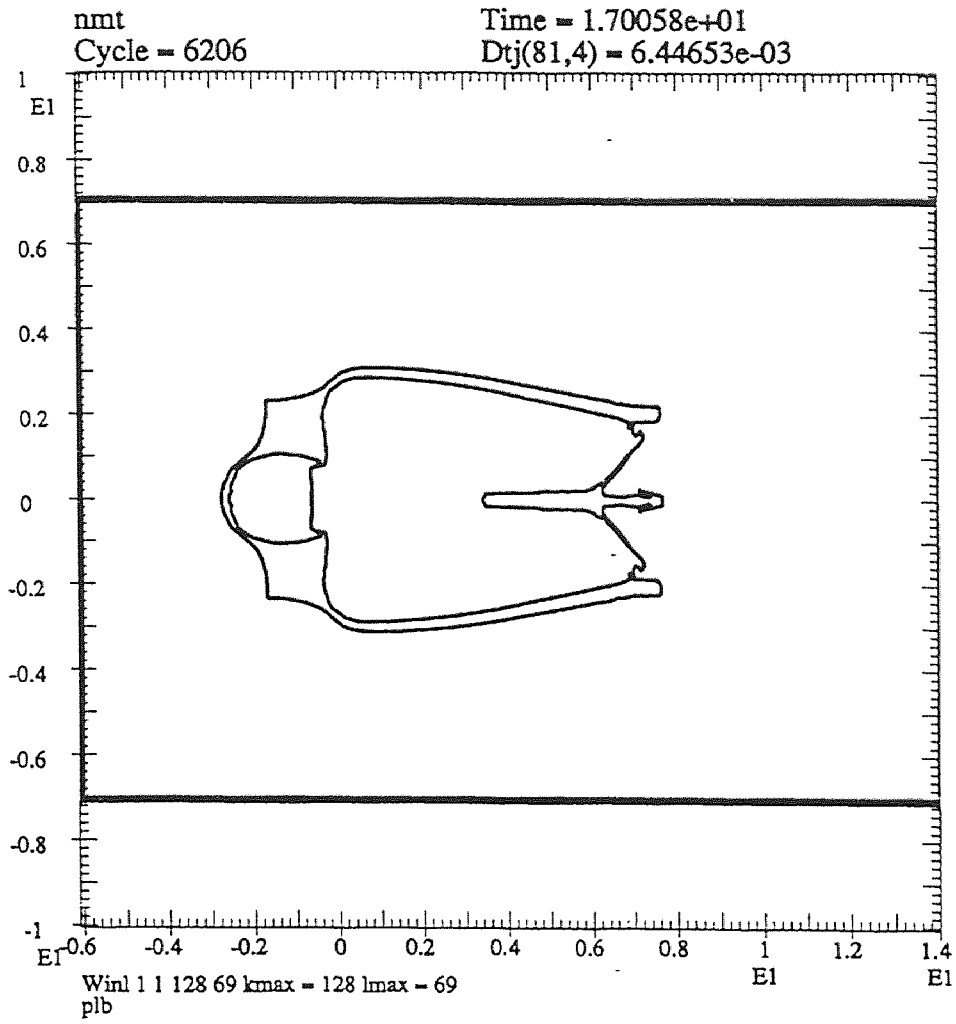

Figure 55 CALE Model at 17 μs

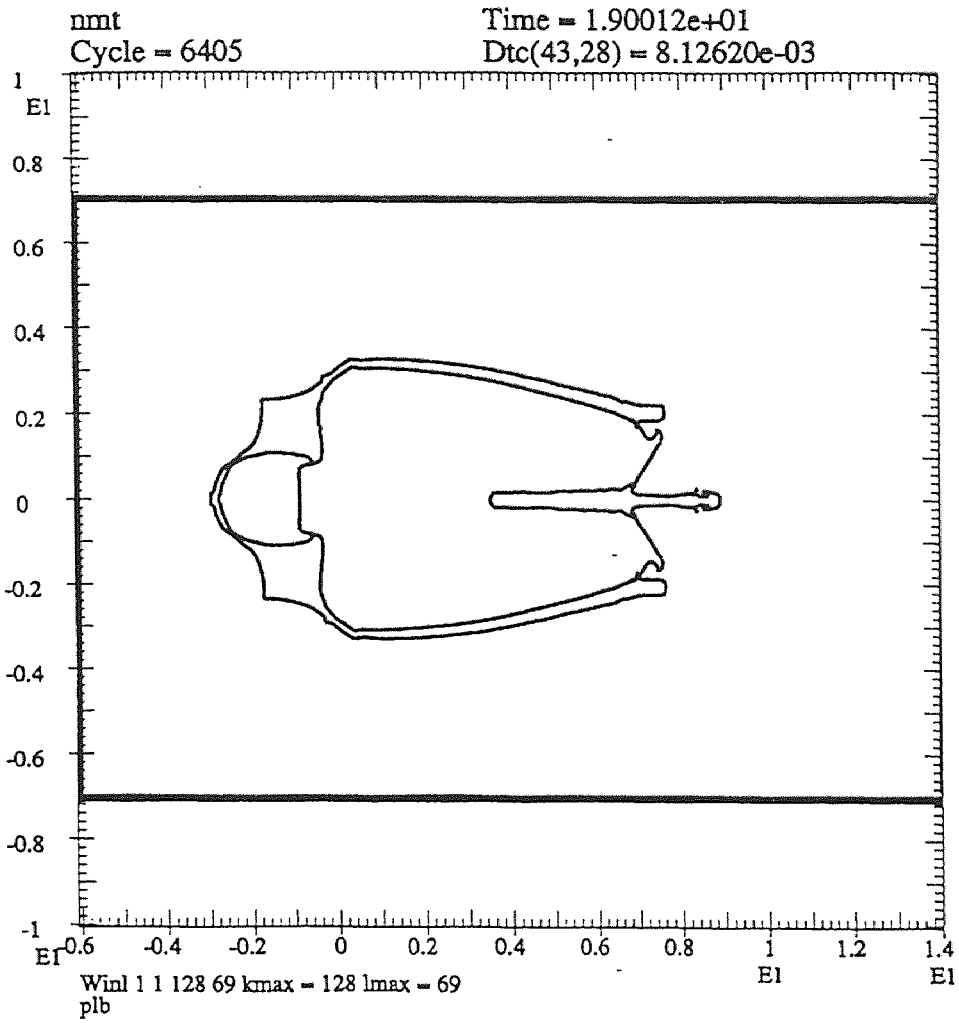

Figure 56 CALE Model at 19 μs

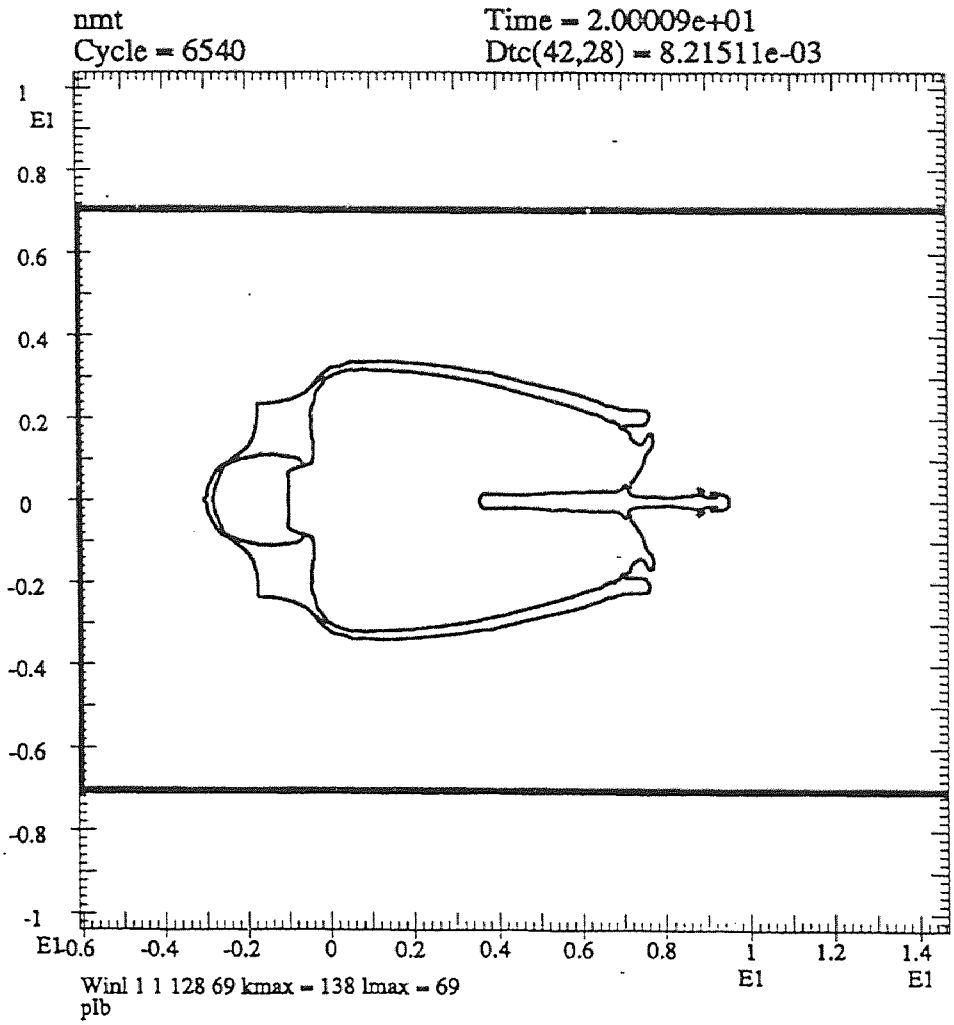

Figure 57 CALE Model at 20 μs

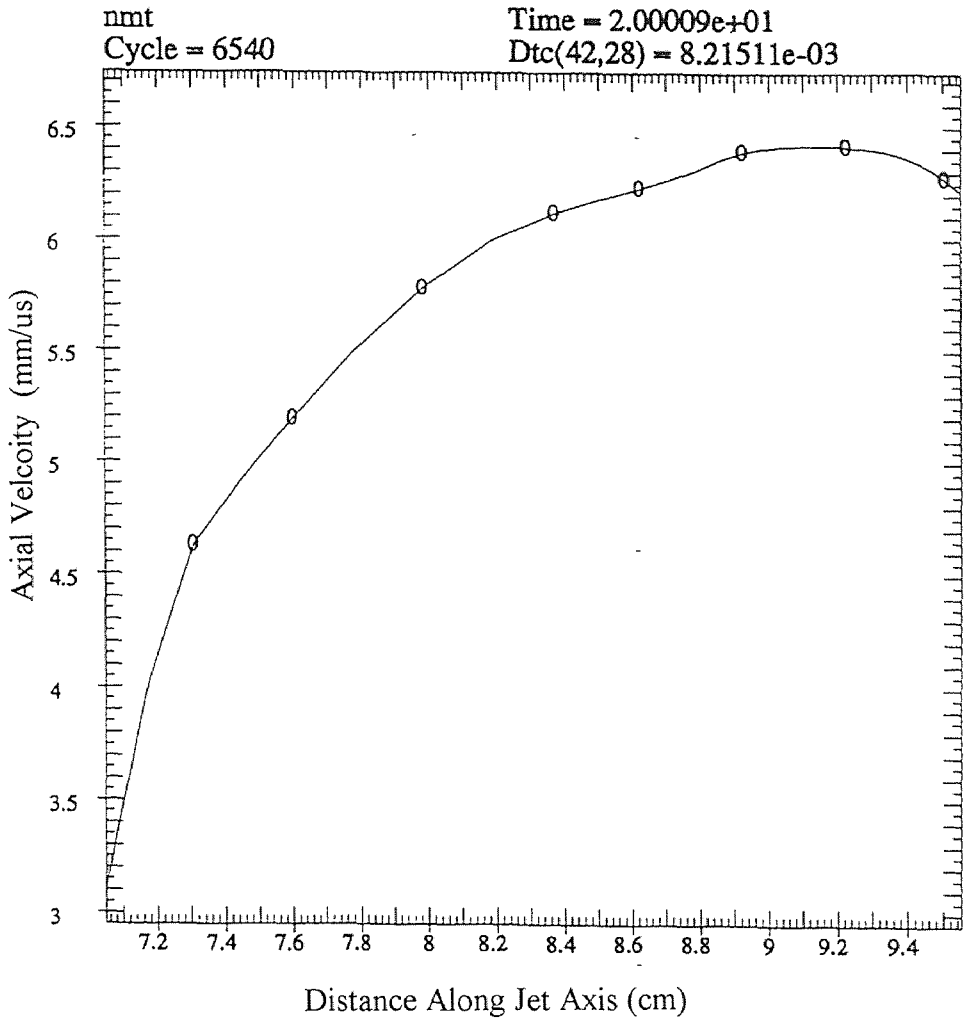

Figure 58 CALE Model, Axial Velocity along Jet

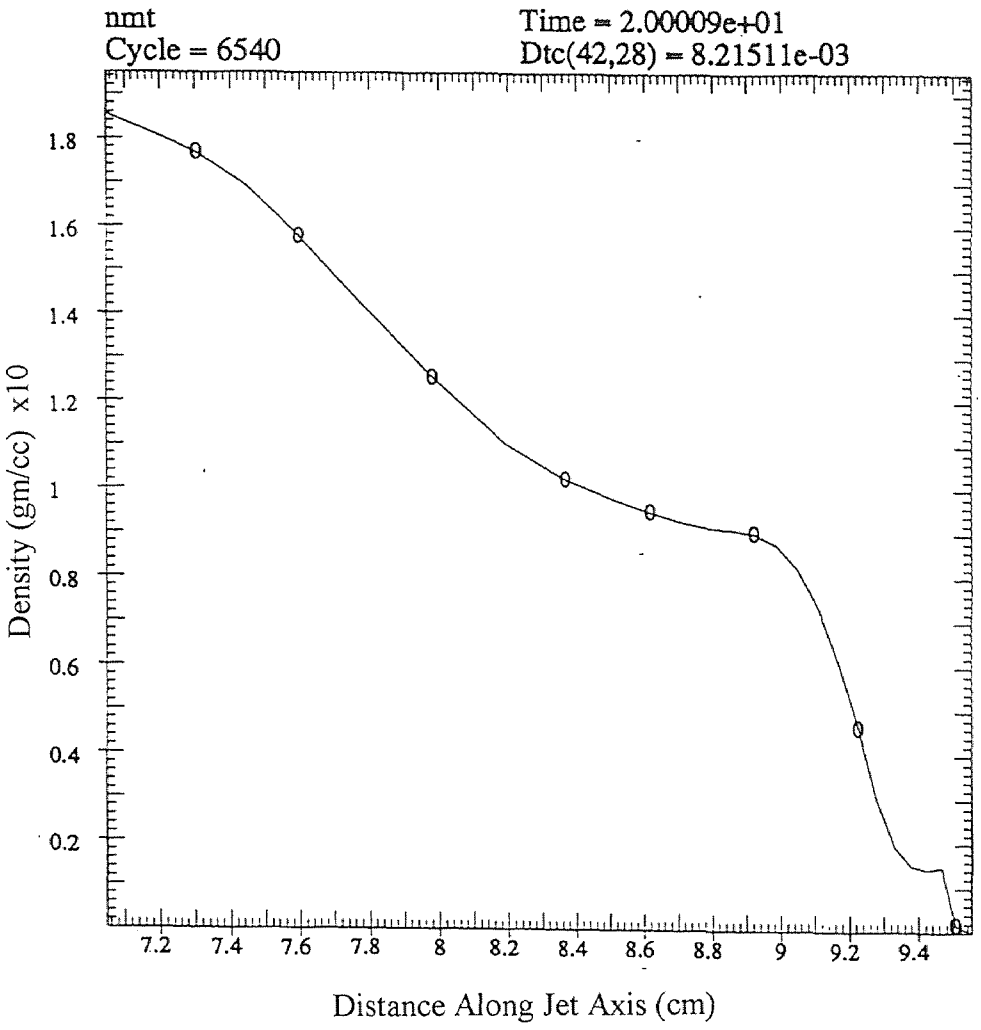

Figure 59 CALE Model, Density along Jet

Table 2 Shock Compression Data for Porous Tungsten

Percent Initial Density	Pressure Gpa	Volume cm^3/gm	Reference
97.00	19.71	.0489	8
97.00	36.61	.0466	8
97.00	57.99	.0448	8
97.00	58.54	.0447	8
97.72	501	.0316	7
97.72	198	.0379	7
80.00	1.99	.0628	9
80.00	1.98	.0628	9
80.00	2.71	.0596	9
80.00	2.33	.0613	9
80.00	1.71	.0641	9
80.00	4.89	.0521	9
80.00	5.89	.0517	9
80.00	7.63	.0519	9
80.00	6.16	.0517	9
80.00	3.42	.0553	9
80.00	3.86	.0536	9
65.75	1.19	.0656	10
65.75	1.21	.0657	10
65.75	1.62	.0613	10
65.75	1.62	.0656	10
65.75	1.63	.0615	10
65.75	2.15	.0579	10
65.75	2.15	.0579	10
65.75	2.17	.0582	10
65.75	2.55	.0559	10
65.75	3.14	.0540	10
65.75	3.77	.0535	10
65.75	4.39	.0511	10
65.75	5.27	.0513	10
65.75	6.14	.0522	10
65.75	11.8	.0523	10
65.75	15.7	.0519	10
65.75	30.2	.0516	10
65.75	43.4	.0475	10
65.75	89.2	.0469	10
65.75	104.5	.0467	10
60.00	.82	.0726	11

Table 2 Shock Compression Data for Porous Tungsten (Continued)

Percent Initial Density	Pressure Gpa	Volume cm^3/gm	Reference
60.00	2.33	.0560	11
60.00	4.26	.0532	11
60.00	5.55	.0530	11
60.00	5.90	.0533	11
60.00	6.24	.0533	11
59.20	376	.0427	7
57.19	132	.0476	7
57.19	31.5	.0511	7
51.35	91	.0593	7
47.70	324	.0427	7
46.82	116	.0528	7
33.67	262	.0557	7
32.89	21.9	.0538	7
25.23	18.5	.0553	7
23.41	205	.0681	7

Percent initial density calculated with a density of solid tungsten of 19.224 gm/cc

Table 3 **Mie-Grüneisen Pressure Calculations**

Percent Initial Density	Measured Pressure	Volume	Calculated Pressure Equation 2.20	Calculated Pressure with Energy Calculated from Data and Equation 2.19
	Gpa	cm^3/gm	Gpa	Gpa
97.00	19.71	0.049	20.751	21.666
97.00	36.61	0.047	38.995	42.109
97.00	57.99	0.045	55.278	62.332
97.00	58.54	0.045	56.238	63.458
97.72	501.00	0.032	232.533	482.95
97.72	198.00	0.038	136.883	193.83
80.00	1.99	0.063	-11.508	-8.140
80.00	1.98	0.063	-11.117	-7.848
80.00	2.71	0.060	-15.516	-11.673
80.00	2.33	0.061	-15.011	-11.251
80.00	1.71	0.064	-5.893	-3.984
80.00	4.89	0.052	4.027	4.146
80.00	5.89	0.052	3.884	4.281
80.00	7.63	0.052	1.149	2.413
80.00	6.16	0.052	3.480	4.015
80.00	3.42	0.055	-4.053	-2.678
80.00	3.86	0.054	1.178	1.580
65.75	1.19	0.066	138.579	32.635
65.75	1.21	0.066	130.899	31.945
65.75	1.62	0.061	83.284	27.554
65.75	1.62	0.066	44.114	16.796
65.75	1.63	0.062	79.582	26.782
65.75	2.15	0.058	47.781	20.522
65.75	2.15	0.058	47.781	20.522
65.75	2.17	0.058	43.514	19.100
65.75	2.55	0.056	34.666	16.876
65.75	3.14	0.054	22.589	12.693
65.75	3.77	0.054	10.608	7.296
65.75	4.39	0.051	18.201	11.801
65.75	5.27	0.051	10.115	7.926
65.75	6.14	0.052	1.462	3.323
65.75	11.80	0.052	-1.654	3.662
65.75	15.70	0.052	0.713	6.765

Table 3 **Mie-Grüneisen Pressure Calculations (Continued)**

Percent Initial Density	Measured Pressure	Volume	Calculated Pressure Equation 2.20	Calculated Pressure with Energy Calculated from Data and Equation 2.19
	Gpa	cm^3/gm	Gpa	Gpa
65.75	30.20	0.052	2.544	13.909
65.75	43.40	0.048	31.531	38.829
65.75	89.20	0.047	36.459	65.930
65.75	104.50	0.047	38.144	75.317
60.00	0.82	0.073	383.997	8.115
60.00	2.33	0.056	64.729	18.488
60.00	4.26	0.053	7.808	5.660
60.00	5.55	0.053	-0.983	2.284
60.00	5.90	0.053	-3.954	0.928
60.00	6.24	0.053	-4.824	0.638
59.20	376.00	0.043	76.752	323.37
57.19	132.00	0.048	30.728	102.46
57.19	31.50	0.051	5.678	21.22
51.35	91.00	0.059	-34.740	35.54
47.70	324.00	0.043	76.752	369.54
46.82	116.00	0.053	-4.571	97.952
33.67	262.00	0.056	-19.624	364.65
32.89	21.90	0.054	-10.088	37.57
25.23	18.50	0.055	-17.713	57.51
23.41	205.00	0.068	-59.660	394.68

Oh Persson Incomplete Compaction Equation used with all Calculated Values

Table 4 Approximate Oh-Persson Equation of State Pressure Calculations

Percent Initial Density	Measured Pressure	Volume	Calculated Pressure Approximate Oh Persson E.O.S.
	GPa	cm^3/gm	Gpa
97	19.71	0.0489	21.6674
97	36.61	0.0466	42.12541
97	57.99	0.0448	62.366
97	58.54	0.0447	63.49811
97.72	501	0.0316	474.8366
97.72	198	0.0379	193.4774
80	1.99	0.0628	-8.13248
80	1.98	0.0628	-7.84107
80	2.71	0.0596	-11.6598
80	2.33	0.0613	-11.0164
80	1.71	0.0641	-3.9813
80	4.89	0.0521	4.145771
80	5.89	0.0517	4.278804
80	7.63	0.0519	2.407003
80	6.16	0.0517	4.01198
80	3.42	0.0553	-2.67732
80	3.86	0.0536	1.578878
65.75	1.19	0.0656	40.3937
65.75	1.21	0.0657	38.83605
65.75	1.62	0.0613	31.0336
65.75	1.62	0.0656	17.5222
65.75	1.63	0.0615	29.90826
65.75	2.15	0.0579	21.75326
65.75	2.15	0.0579	21.75326
65.75	2.17	0.0582	20.09038
65.75	2.55	0.0559	17.53847
65.75	3.14	0.054	12.97067
65.75	3.77	0.0535	7.347128
65.75	4.39	0.0511	11.98667
65.75	5.27	0.0513	8.029957
65.75	6.14	0.0522	3.30643
65.75	11.8	0.0523	3.601187
65.75	15.7	0.0519	6.652299
65.75	30.2	0.0516	13.49536

Table 4 **Approximate Oh-Persson Equation of State Pressure Calculations (Continued)**

Percent Initial Density	Measured Pressure	Volume	Calculated Pressure Approximate Oh Persson E.O.S.
	GPa	cm^3/gm	Gpa
65.75	43.4	0.0475	38.38907
65.75	89.2	0.0469	62.23634
65.75	104.5	0.0467	70.07532
60	0.82	0.0726	43.39688
60	2.33	0.056	22.27697
60	4.26	0.0532	5.694991
60	5.55	0.053	2.263003
60	5.9	0.0533	0.914961
60	6.24	0.0533	0.627663
59.2	376	0.0427	232.4244
57.19	132	0.0476	87.9622
57.19	31.5	0.0511	20.32179
51.35	91	0.0593	30.06455
47.7	324	0.0427	245.9228
46.82	116	0.0528	79.11195
33.67	262	0.0557	223.4276
32.89	21.9	0.0538	35.56309
25.23	18.5	0.0553	58.85825
23.41	205	0.0681	281.6295

Table 5 **Proposed Equation of State Pressure Calculations**

Percent Initial Density	Measured Pressure	Volume	Calculated Pressure Proposed Equation of State
	GPa	cm^3/gm	Gpa
97.00	19.71	0.049	21.683
97.00	36.61	0.047	42.190
97.00	57.99	0.045	62.423
97.00	58.54	0.045	63.564
97.72	501.00	0.032	478.27
97.72	198.00	0.038	193.54
80.00	1.99	0.063	-8.116
80.00	1.98	0.063	-8.019
80.00	2.71	0.060	-11.914
80.00	2.33	0.061	-11.251
80.00	1.71	0.064	-4.079
80.00	4.89	0.052	4.132
80.00	5.89	0.052	4.239
80.00	7.63	0.052	2.275
80.00	6.16	0.052	3.958
80.00	3.42	0.055	-2.806
80.00	3.86	0.054	1.533
65.75	1.19	0.066	41.443
65.75	1.21	0.066	40.067
65.75	1.62	0.061	32.703
65.75	1.62	0.066	18.777
65.75	1.63	0.062	31.588
65.75	2.15	0.058	23.190
65.75	2.15	0.058	23.190
65.75	2.17	0.058	21.438
65.75	2.55	0.056	18.692
65.75	3.14	0.054	13.744
65.75	3.77	0.054	7.639
65.75	4.39	0.051	12.563
65.75	5.27	0.051	8.240
65.75	6.14	0.052	3.112
65.75	11.80	0.052	3.074
65.75	15.70	0.052	6.086
65.75	30.20	0.052	12.592

Table 5 **Proposed Equation of State Pressure Calculations (Continued)**

Percent Initial Density	Measured Pressure	Volume	Calculated Pressure Proposed Equation of State
	GPa	cm^3/gm	Gpa
65.75	43.40	0.048	38.212
65.75	89.20	0.047	62.240
65.75	104.50	0.047	70.446
60.00	0.82	0.073	35.031
60.00	2.33	0.056	23.812
60.00	4.26	0.053	5.884
60.00	5.55	0.053	1.927
60.00	5.90	0.053	0.404
60.00	6.24	0.053	0.0532
59.20	376.00	0.043	270.12
57.19	132.00	0.048	91.285
57.19	31.50	0.051	19.350
51.35	91.00	0.059	26.673
47.70	324.00	0.043	298.97
46.82	116.00	0.053	82.02
33.67	262.00	0.056	276.26
32.89	21.90	0.054	31.95
25.23	18.50	0.055	49.42
23.41	205.00	0.068	301.20

REFERENCES

1. Simon, J. and R. DiPersio "Jet Formation and Utilization" from Technology of Explosive Sandia Laboratories. Vol. 1, Sandia Laboratories 1974.

2. "Selected Hugoniots" Prepared by Group GMX-6, Los Alamos Scientific Laboratory, University of California, May 1, 1969.

3. Handbook of Chemistry and Physics, 68th Edition. CRC Press Inc. Boca Roca Florida.

4. Oh, H. "Shock Extrusion of Ingots from Powders or Solids" Invention Disclosure, CETR New Mexico Institute of Mining and Technology, Socorro NM, June 7 1988.

5. Meyers, M. and N. Thadhani, "Dynamic Deformation of Solids MET 567 Class Notes". New Mexico Institute of Mining and Technology Socorro, NM

6. Davis, W., "Detonation Phenomena" Class Manual from Technology of Explosives Sandia Laboratories. Vol. 1,, Sandia Laboratories 1974.

7. Hermann, W. "Constitutive Equation of the Dynamic Compaction of Ductile Porous Materials" Journal of Applied Physics Vol. 40, No. 4 ,2490, May 1969.

8. Grüneisen, E. "Zusammenhang zwischen Komressibilität, Thermischer Ausehnung, Atomvolumen und Atomwärme der Metalle" Annalen der Physik IV. Folge 26, 393.

9. Krupnikov, K. K., M. I. Brazhnik, V. P. Krupnikova "Shock Compression of Porous Tungsten" Soviet Physics JETP, Vol. 15, N0. 3, 470, Sept. 1962.

10. Marsh, Stanley P. LASL Shock Hugoniot Data, University of California Press, Berkeley, Ca. 1980.

11. Dattaraya. P. and R. M. Lamothe "Behavior of Porous Tungsten under Shock Compression at Room Temperatures" Journal of Applied Physics, Vol. 48, No. 7, 2871, July 1977

12. Boade, R. R. "Dynamic Compression of Porous Tungsten" Journal of Applied Physics vol. 40, No. 9, August 1969.

13. Gourdin, W. H. and S. L. Weinland "Dynamic Compaction of a Monosized Spherical Tungsten Powder" Proceedings of the 4th American Physical Topical Conference on Shock Waves in Condensed Mater, July 22-25, 1985 Spokane Wash.

14. Kormer, S. B., A. I. Funtikov, V. D. Urlin, and A. N. Kolesnikova "Dynamic Compression of Porous Metals and the Equation of State with Variable Specific Heat at High Temperatures", Soviet Physics JETP, Vol. 15, N0. 3, 477, Sept. 1962.

15. Zharkov, V. N. and V. A. Kalinin. "Equations of State for Solids at High Pressures and Temperatures". Consultants Bureau, New York 1971.

16. McQueen, R. G. , S. P. Marsh, J. W. Taylor, J. N. Fritz, and W. J. Carter, "The Equation of State of Solids from Shock Wave Studies". High Velocity Impact Phenomena. Edited by R. Kinslow, Academic Press, New York, 1970.

17. Steinberg, D. J. "The Temperature Dependence of Grüneisen's Gamma at High Temperature", J. Appl. Phys, 52(10) , 6415, Oct. 1981.

18. Cowperthwaite, M. "Significance of Some Equations of State Obtained from Shock-Wave Data".

19. Kormer, S. B., A. I. Funtikov, V. D. Urlin, and A. N. Kolesnikova "Dynamic Compression of Porous Metals and the Equation of State with Variable Specific Heat at High Temperatures", Soviet Physics JETP, Vol. 15, N0. 3, 477, Sept. 1962.

20. Oh, H. and P. Persson, "A Full Range Hugoniot of State for Porous Materials", American Physical Society Topical Conference on Shock Waves Albuquerque N. M. Aug. 1989.

21. Oh, H. "Calculation of Shock Hugoniots and Release Isentropes of Porous Materials" Center for Explosives Technology Research New Mexico Institute of Mining and Technology Socorro, NM, CETR Report A-08-89, July 1989.

22. Oh, H. "Thermodynamic Properties of Porous Materials under Shock Loading". New Mexico Institute of Mining and Technology, Socorro, New Mexico, 1989.

23. Johnson, J. B. "Analysis of Oh and Persson's (1989) Paper on Equation of State for Extapolation of High-Pressure Shock Hugoniot Data" Written Communication to P. Persson New Mexico Institute of Technology. 1995.

24. Hermann, W. "Constitutive Equation of the Dynamic Compaction of Ductile Porous Materials" Journal of Applied Physics Vol. 40, No. 4 ,2490, May 1969.

25. Boade, R. R. "Experimental Shock Loading Properties of Porous Materials and Analytical Methods to Describe these Properties" Shock Waves and the Mechanical Properties of Solids, Proc. of the 17th Sagamore Army Materials Conference. Raquette Lake NY Sept. 1-4 1970.

26. Oh, K. and P. Persson, "A Constitutive Model for the Shock Hugoniot of Porous Materials in the Incomplete Compaction Regime", J. Appl Phys Vol. 66 (10), 4736, 15 Nov. 1989.

27. Butcher, B. M. "The Description of Strain-Rate Effects in Shocked Porous Materials" Shock waves and the Mechanical Properties of Solids, Proc. of the 17th Sagamore Army Materials Conference. Raquette Lake NY Sept. 1-4 1970.

28. Carroll, M. M. and A. C. Holt. "Static and Dynamic Pore-Collapse Relations for Ductile Porous Materials". J. Appl. Phys., No. 4, April 1972.

29. Johnson, J, N. and F. L. Addessio "Tensile Plasticity and Ductile Fracture", J. Appl Phys 64 (12), 6699, 15 Dec. 1988

30 Johnson, J, N. , "Dynamic Fracture and Spallation in Ductile Solids" J. Appl Phys 52 (4), 2812, Apr. 1981.

31. Gurson, A. L. "Continuum Theory of Ductile Rupture by Void Nucleation and Growth: Part I- Yield Criteria and Flow Rules for Porous Ductile Media. Journal of Engineering Materials and Technology, Jan. 1977.

32. Addession, F. L. and J. N. Johnson "Rate-dependent Ductile Failure Model" J. Appl. Phys 74 (3) , 1640, 1 August 1993.

33. Tipton, Robert "CALE Users Manual" Lawrence Livermore National Laboratories 1 Oct. 1995.

34. Wright, N., J. E. Flinn, G. E. Korth, "Consolidation Methods for Rapidly Solidified Type 304 Stainless Steel" Metal Powders Report, 281, April 1986.

35. Staudhammer, K. P. and L. E. Murr "Dynamic Consolidation of Cylinders by Oblique Shock Loading", Journal of Materials Science 25 (1990) 2287-2298.

36. Gurney, R. W. "The Initial Velocity of Fragments from Bombs, Shells, and Grenades", Ballistic Research Laboratory Report No. 405, 14 Sept. 1943.

37. Jones, G. E., Kennedy, J. E. and Berthoff, L., D. "Ballistic Calculations of R. W. Gurney". An. J. Phys. 48(4) Apr. 1980.

38. Fuchs, B. "Picatinny Arsenal Cylinder Expansion Test and a Mathematical Examination of the Expanding Cylinder" U.S. Army ARDEC, Picatinny Arsenal NJ Oct. 1995.

39. Walters, W. P. and J. A. Zukas, Fundamentals of Shaped Charges, John Wiley & Sons, New York, 1989.

40. Walters, W. "Basic Principles of Hypervelocity Impact and Related Topics" Course Notes, Computational Mechanics Associates Inc. Apr. 6-10 1987 Philadelphia, PA

41. Chou, P. C. and W. J. Flis "Recent Developments in Shaped Charge Technology". Propellants, Explosives, Pyrotechnics 11, 99-114, 1986.

42. Mader, C. L.. "Numerical Modeling of Detonations" University of California Press, Berkeley Ca. 1979.

43. VonNeumann, J. and R. D. Richtmyer "A Method for the Numerical Calculation of Hydrodynamic Shocks" Journal of Applied Physics, Vol. 21, 234, Mar. 1950.

44. Al'tshuler, L. V. "Use of Shock Waves in High-Pressure Physics". Usp. Fiz. Nauk 85, 197-258, Geb. 1965.

45. Yoshida, M. "Program MY1DL" New Mexico Institute of Mining and Technology" May 1986.

46. Jamet, F. and A. Lichtenberger, "Investigation of Copper Tungsten Shaped Charges", 9TH Ballistic Symposium.

47. Fu, W. T., Z. H. Rong, Z. J. Long, and M. H. Wei, "Copper Tungsten Shaped Charge Liners and its Performance" 13th Intl. Symposium of Ballistics, 1-3 June 1992.

48. Lassila, D. H. "Mechanical Behavior of Tungsten Shaped Charge Liner Materials". 14th International Symposium on Ballistics, Québec, Canada, 26-29 Sept. 1993.

49. Yih, Stephen W. H. , Chun T. Wang. Tungsten, Plenum Press New York. 1980.

50. Freid, L. E. "Cheetah 1.0 User's Manual" Lawrence Livermore National Laboratory, UCRL-MA-117541, 1994.

51. Callen, Herbert B. Thermodynamics, John Wiley & Sons Inc. NY, 1970.

APPENDIX

A.1 Introduction

This work has covered the formation mechanics of shaped charges references to the physics of the detonation process. For clarity a summary description of the detonation process was separated from the thesis and placed in this appendix. The appendix covers the theory of ideal detonations and briefly describes the background and the equation of state used for the explosive in the computer modeling of the shaped charge.

Detonations are an extremely rapid form of combustion that may take place in a material which contain the fuel and the oxidizer, in the form of a mixture or within the molecules, required for the combustion. A detonation can convert chemical energy at an approximate rate of 10^{10} watts/cm^2, as compared to the approximate total electric energy generating capacity of the U.S., which is 4×10^{11} watts, Ref (1). In a detonation a shock wave in the material produces a rapid chemical reaction, which in turn supports the detonation. Because of the supporting combustion, a detonation shock wave travels at a constant velocity. The reaction zone behind the detonation front is typically only a few millimeters thick. Although detonations include chemical reactions, detonation phenomenona can be studied through an analysis of the physics of the event.

A.2 Detonations

A.2.1 Chapman Jouget Detonation, Simplest Theory

The simplest theory uses the following assumptions:

one dimensional flow

steady jump discontinuities to complete reaction and equilibrium states

A detonation propagating into the unreacted material at constant velocity

Steady state

For a detonation propagating at velocity D into an explosive at rest, the conditions shown in appendix Figure 1 apply.

For this system there are five unknown variables required to determine the final state of the system: density, pressure, temperature, detonation velocity and particle velocity. Some information on the relationships between these variables can be obtained from the conservation equations, ref (1).

For the conservation of mass, with a coordinate system moving with the detonation front, the unreacted material is moving with a velocity D towards the front. The variable u is the particle velocity of the reacted gases in a fixed reference frame.

$$\rho_0 D = \rho(D - u) \qquad (A.1)$$

For the conservation of momentum, a control volume expanding with the detonation front is used in a fixed reference frame. The control volume then includes all of the reacted gases. The detonation front and control volume move forward at velocity D taking in the unreacted material at p_O to a final velocity of u. The conservation of momentum becomes:

$$P - P_0 = \rho_0 u D \qquad (A.2)$$

The same equation can be developed using a reference frame moving with the shock front and the conservation of mass above, equation A.1. For this case the conservation of momentum is:

$$P + \rho(D-u)^2 = P_0 + \rho_0 D^2 \qquad (A.3)$$

From equation A.1 $\rho(D-u) = \rho_0 D$ then:

$$P - P_0 = \rho_0 D^2 - \rho_0 D^2 - \rho_0 D(D-u) \qquad (A.4)$$

Simplifying, equation A.2 is obtained:

$$P - P_0 = \rho_0 u D \qquad (A.2)$$

By eliminating the particle velocity, u, from equations A.1 and A.2 the Rayleigh line is developed:

From equation A.1

$$\rho_0 D = \rho(D-u) = \rho D - u\rho \qquad (A.1)$$

Rearranging equation A.2

$$\frac{\rho}{\rho_0}\frac{P-P_0}{D} = u\rho \qquad (A.2)$$

Adding Equation A.1 to A.2

$$\rho_0 D + \frac{\rho}{\rho_0}\frac{P-P_0}{D} = \rho D$$

Grouping terms and multiplying by D

$$(\rho_0 - \rho)D^2 + \frac{\rho}{\rho_0}(P - P_0) = 0$$

Multiplying by $\frac{\rho_0^{\,2}}{(\rho_0 - \rho)}$

$$\rho_0^{\,2}D^2 + \frac{(P - P_0)\rho_0\rho}{(\rho_0 - \rho)} = 0$$

Simplifying

$$0 = \rho_0^{\,2}D^2 + \frac{P - P_0}{\left(\frac{1}{\rho} - \frac{1}{\rho_0}\right)}$$

$$0 = \rho_0^{\,2}D^2 - \frac{P - P_0}{(v_0 - v)}$$

The Rayleigh line is then defined by:

$$R \equiv \rho_0^{\,2}D^2 - \frac{P - P_0}{(v_0 - v)} = 0 \qquad \text{(A.5)}$$

If the detonation velocity is eliminated instead, the particle velocity as a function of pressure and specific volume is obtained.

$$u^2 = \frac{P - P_0}{v_0 - v} \qquad \text{(A.6)}$$

The Rayleigh Line was developed by eliminating the particle velocity from the conservation of mass and momentum (equations A.1 & A.2). The slope of the line is dependent upon the detonation velocity. The line represents all of the possible states allowed, dependent upon the conservation of mass and momentum, for a particular

detonation velocity. These states have not accounted for the energy released from the detonation.

Application of the conservation of energy

From the conservation of energy:

$$\Delta e = P_0 v_0 - Pv + \tfrac{1}{2}\left(D^2 - (D-u)^2\right) \qquad (A.7)$$

By eliminating u and D from equations A.1, A.2, and A.7, the Hugoniot curve is developed.

$$H \equiv \Delta e - \tfrac{1}{2}(P + P_0)(v_0 - v) = 0 \qquad (A.8)$$

The Hugoniot curve was developed by eliminating the particle velocity, u, and the detonation velocity from the conservation equations for mass, momentum, and energy, equations A.1, A.2, and A.7. This curve is a description of the allowed states of the reacted gases, unlike the Rayleigh line which is applicable to the entire process. The curve's location is dependent upon the heat of detonation. The curve does not include the initial state unless the heat of detonation is set equal to zero, as for a non-reacting material.

A.2.2 Intersections between the Rayleigh Line and the Hugoniot Curve

At this point in the development there are three equations available: conservation of mass, momentum, and energy. However there are five unknown variables: the detonation velocity, the particle velocity, and three state variables: final pressure, density and temperature. Even with an applicable equation of state there are not enough equations to determine the final state. Some assumptions must be made to solve the problem. By

using both the Hugoniot curve and the Rayleigh line, a description of the process can be derived from the intersection of the two. The Rayleigh line will be used to show the variations of states for different detonation velocities, and the Hugoniot curve is used to describe the variations in final state of the reacted gases. In later development, the Hugoniot curve is also used to relate varying degrees of reaction to the final state.

With an expression for the equation of state, the state is obtained as a function of the detonation velocity by the intersection of the Rayleigh line and Hugoniot curves. The development to this point is insufficient to yield the characteristic detonation velocity, known to exist from experimentation.

The Hugoniot curve follows the possible states of the reacted gases for all detonations, and is unique for each material and its degree of reaction, assumed complete for the simplest theory. The Hugoniot curve is a rectangular hyperbola in the P-v plane. The Rayleigh line is dependent upon the detonation velocity, see appendix Figure 2.

From the chart it can be seen that three types of conditions may exist: two, one, and no intersections between the Rayleigh line and Hugoniot curves. For slow detonations, $D < D_{cj}$, no intersection exists, and there is no solution. For one detonation velocity, one intersection exists, the CJ point. The CJ point is named after Chapman and Jouget independent developers of the simplest theory. For higher detonation velocities, $D > D_{cj}$, two intersections exist, one at a lower or weak point and one at an upper or strong point.

A.2.3 Thermodynamics about the CJ Point

Thermodynamics can be used to determine the sonic conditions at the CJ point, Ref (2). Since the Rayleigh line and Hugoniot curves are tangent at the CJ point:

$$\left.\frac{\partial P}{\partial v}\right)_R = \left.\frac{\partial P}{\partial v}\right)_H \tag{A.9}$$

From Equation A.5

$$R \equiv \rho_0{}^2 D^2 - \frac{P - P_0}{(v_0 - v)} = 0 \tag{A.5}$$

Rearranging

$$P = P_0 + (v_0 - v)\rho_0{}^2 D^2$$

Differentiating

$$\left.\frac{\partial P}{\partial v}\right)_R = -\rho_0{}^2 D^2$$

Then from equation A.5

$$\left.\frac{\partial P}{\partial v}\right)_R = -\rho_0{}^2 D^2 = -\frac{P - P_0}{v_0 - v} \tag{A.10}$$

For the Hugoniot curve

$$H \equiv \Delta e - \tfrac{1}{2}(P + P_0)(v_0 - v) = (e - e_0) - \tfrac{1}{2}(P - P_0)(v_0 - v) = 0 \tag{A.8}$$

Solving for the pressure

$$P = \frac{2(e - e_0)}{v_0 - v} + P_0$$

Differentiating

$$\frac{\partial P}{\partial v}\Big)_H = \frac{(v - v_0)2\left(\frac{\partial e}{\partial v}\right)_H + 2(e - e_0)}{(v - v_0)^2}$$

$$= \frac{2\frac{\partial e}{\partial v}\Big)_H (v - v_0) + \tfrac{1}{2}(P + P_0)(v_0 - v)}{(v - v_0)^2}$$

Simplifying

$$\frac{\partial P}{\partial v}\Big)_H = \frac{2\frac{\partial e}{\partial v}\Big)_H + \tfrac{1}{2}(P + P_0)}{(v - v_0)} \qquad \text{(A.11)}$$

From thermodynamics between equilibrium states

$$Tds = de + Pdv \qquad \text{(A.12)}$$

Using de from the differential of the Hugoniot curve, $\frac{\partial P}{\partial v}\Big)_H$

$$de = -\tfrac{1}{2}(P_0 P)dv + \tfrac{1}{2}(v_0 - v)dP \qquad \text{(A.13)}$$

Then from equations A.12 and A.13

$$Tds = -\tfrac{1}{2}(P_0 + P)dv + \tfrac{1}{2}(v_0 - v)dP + Pdv$$

$$= -\tfrac{1}{2}(P_0 - P)dv + \tfrac{1}{2}(v_0 - v)dP$$

Dividing by dv

$$T\frac{\partial s}{\partial v}\Big)_H = \frac{\left((P - P_0) + (v_0 - v)\frac{\partial P}{\partial v}\Big)_H\right)}{2}$$

$$= \frac{(v_0 - v)\left((P - P_0) + (v_0 - v)\frac{\partial P}{\partial v}\right)_H}{2} \qquad (A.14)$$

Then solving for $\left(\frac{\partial P}{\partial v}\right)_H$

$$\left(\frac{\partial P}{\partial v}\right)_H = \frac{2}{(v_0 - v)} T\left(\frac{\partial s}{\partial v}\right)_H + \frac{P - P_0}{v_0 - v}$$

At some point the adiabatic curve passing through the CJ point has the same slope as the Hugoniot curve, Ref (3). By comparing the slope of dP/dv for the Rayleigh line, equation 10, and the Hugoniot curve, equation A.14 becomes:

$$\left(\frac{\partial P}{\partial v}\right)_R = \left(\frac{\partial P}{\partial v}\right)_H$$

$$\frac{2}{(v_0 - v)} T\left(\frac{\partial s}{\partial v}\right)_H + \frac{P - P_0}{v_0 - v} = \frac{P_0 - P}{v - v_0}$$

It can be seen that the slopes are equal only when ds = 0, then,

$$\frac{P_0 - P}{v - v_0} = \left(\frac{\partial P}{\partial v}\right)_H \qquad (A.15).$$

The curve presenting equation A.15 goes through P_o, v_o the initial conditions of the material. Since ds = 0 at the CJ point, the Rayleigh line and Hugoniot curve are not only tangent to each other, but are also tangent to the isentrope for the completely reacted material. The condition of ds = 0 can also be used to relate the flow to the speed of sound in the reacted material.

At the CJ point

$$ds = 0$$

Then

$$Tds = de + Pdv$$

becomes

$$\left.\frac{\partial e}{\partial v}\right)_H = -P$$

Since the slopes are tangent at the CJ point

$$\left.\frac{\partial P}{\partial v}\right)_s = \left.\frac{\partial P}{\partial v}\right)_R = \left.\frac{\partial P}{\partial v}\right)_H \tag{A.16}$$

From the definition of the speed of sound

$$c^2 = \left.\frac{\partial P}{\partial \rho}\right)_s \tag{A.17}$$

$$\rho = \frac{1}{v} \qquad \text{then:} \qquad d\rho = -\frac{dv}{v^2}$$

$$c^2 = -v^2 \left.\frac{\partial P}{\partial v}\right)_s$$

Then

$$\frac{-c^2}{v^2} = -{\rho_0}^2 D^2$$

$$c^2 = \frac{{\rho_0}^2 D^2}{\rho^2}$$

From the conservation of mass

$$\rho_0 D = \rho(D - u) \tag{A.1}$$

Then

$$c^2 = (D - u)^2$$

which gives:

$$D = u + c \tag{A.18}$$

Sonic conditions exist at the CJ point. The conditions at the intersections above and below the CJ point, with higher detonation velocities, remain to be determined. Since the conditions are sonic it is reasonable to assume that any rarefactions from behind will not catch up to the detonation wave. The detonation wave will behave as if it were followed only by gases at the CJ pressure.

Sonic conditions on the upper and lower intersections

From the Rayleigh line

$$R \equiv \rho_0{}^2 D^2 - \frac{P - P_0}{(v_0 - v)} = 0 \tag{A.5}$$

From the conservation of mass

$$\rho_0{}^2 D^2 = \rho^2 (D - u)^2 = \frac{P - P_0}{v_0 - v}$$

Then

$$(D - u)^2 = \frac{(P - P_0)v^2}{v_0 - v}$$

Using Equation A.17

$$c^2 = -v^2 \frac{\partial P}{\partial v}\Big)_s <>= \frac{(P - P_0)v^2}{v_0 - v} = (D - u)^2$$

At the CJ point the equation is equal, as shown earlier. On the lower intersection, flow is subsonic, $u + c > D$ and $P < P_{cj}$. On the upper intersection, the flow is supersonic, $u + c < D$ and $P > P_{cj}$. On the possible upper intersections, above the CJ point, the

velocity of sound exceeds the detonation velocity. Any rarefaction waves will catch up to the detonation front and slow it down. These solutions can therefore be disregarded as a possible steady state solution. On the lower intersections, below the CJ point, solutions are also rejected. Explanations in the literature vary, but are consistently poor or incorrect. A reason for disregarding the weak solution is covered with the ZND model, where it is much more clear.

With the assumption that the final state is at the CJ point, a complete determination of the final state can be made with a suitable equation of state. The assumption of a Chapman-Jouget detonation is used in place of a missing equation.

A.2.4 The Zeldovich-Von Neumann-Doering (ZND) Model

In the Chapman-Jouget or simplest model, the shock wave and chemical reaction are assumed to be infinitely thin and occur simultaneously. In the ZND model, a finite and irreversible reaction zone follows an infinitely thin shock wave, Ref.(1). This model replaces the single Hugoniot curve in the simplest theory a Hugoniot curve for complete reaction

($\lambda = 1$) with a Hugoniot curve that changes continually with the degree of reaction. From the equation of the Hugoniot curve, equation A.8:

$$H \equiv \Delta e - \tfrac{1}{2}(P + P_0)(v_0 - v) = 0 \qquad \text{(A.8)}$$

it can be seen that for a degree of reaction of 0 the change in energy is zero, and the Hugoniot curve passes through the initial condition, and remains below and to the left of the Hugoniot curves for higher degrees of reaction. The shifting of the Hugoniot curve

with the degree of reaction, causes the pressure and specific volume to vary throughout the reaction. The thickness of the reaction zone is a factor that effects how ideally the detonation behaves, how close to the CJ development. The detonation process in appendix Figure 1 is then replaced by that of appendix Figure 3.

The dependence of the state on the degree of reaction can be shown on a modified pressure specific volume plot, see appendix Figure 4. The shock wave initially compresses the unreacted material, and follows the Hugoniot curve for a degree of reaction of 0, to a pressure higher than in the simplest theory at the point the Rayleigh line and unreacted Hugoniot curve meet. As the material goes through the reaction, its properties follow the Rayleigh line until it intersects the Hugoniot curve. In this model, there is no path to the lower or weak intersection as the material would have to take a path through a region with a degree of reaction greater than 1. This relates well to the simplest theory where the weak intersection was discounted without a proper explanation.

A.2.5 JWL (Jones-Wilkins-Lee) Equation of State

In the JWL equation of state the isentrope through the CJ point is written as, ref (6):

$$P = Ae^{-R_1 V} + Be^{-R_2 V} + CV^{-(w+1)} \qquad (A.19)$$

where: A,B,C,R_1,R_2, and w are constants and $V = \frac{v}{v_0}$

The energy along this isentrope is determined from the Maxwell relationship:

$$\left.\frac{\partial e}{\partial v}\right)_s = -P$$

Using the energy and pressure as reference values along the isentope in equation A.3, the equation of state becomes:

$$e = \rho_0 e = \frac{A}{R_1} e^{-R_1 V} + \frac{B}{R_2} e^{-R_2 V} + \frac{C}{w} V^{-(w+1)} + \frac{V}{w}\left(P - Ae^{-R_1 V} + Be^{-R_2 V} + CV^{-(w+1)}\right)$$

(A.20)

A.2.6 Computations of Detonation Parameters

The computer modeling of one dimensional Chapman-Jouget detonation is complicated by the requirement of knowing the final products of detonation. Either assumed products of detonation, sometimes called a frozen composition, are used or the equilibrium composition must be determined. The products of detonation are not always gaseous, and like any form of combustion the process is not complete. The products are not the optimum for the highest heat of detonation. The mixed composition causes problems in the development of mixture rules for the total properties of the reacted material. The following is a very brief description of the thermodynamic numeric Tiger and Cheetah codes, Ref. (7)(8).

The Tiger and Cheetah code determines the final composition by minimizing Gibbs free energy of the major products of detonation. The code also allows for the use of frozen compositions. Since the properties are required for all products of combustion, the code is made manageable by limiting the products of detonation. This does not cause problems since many of the products not accounted for form only a small percentage of the total reacted products. This material can accurately be neglected in numerical models.

The Tiger and Cheetah codes calculates the thermodynamic variables using separate equations of state for gaseous, solid, and condensed, equations of state. Since the code is modular, containing many separate subroutines, it is possible to configure the code to use different equations of state. The pressure is computed using only the gaseous products, as the condensed constituents do not appreciably contribute to the pressure.

The Tiger routine starts the calculations at an estimated CJ point. This estimate is obtained by performing a constant volume expansion explosion point calculation. The code then performs calculations that ideally converge to the CJ point. The code then steps to the next pressure along an approximation to the Hugoniot curve:

$$P_{i+1} = \frac{P_i + 2\left(e_i - e_o\right) - \left(P_i + P_o\right)\left(v_o - v_{i+1}\right) + 2P_i\left(\frac{1}{\alpha}\right)\left(v_{i+1} - v_i\right)}{\left(v_o - v_{i+1} - 2v_i\beta_i\right)} \qquad \text{(A.21)}$$

The next estimation of the specific volume is obtained by using an expression for the CJ state:

$$v_i = v_o\left(\frac{1}{k}\left(1 - \frac{\rho_o}{\rho_i}\right) + 1\right) \qquad \text{(A.22)}$$

where

$$\alpha = \frac{1}{P}\frac{\partial e}{\partial v}\Bigg)_P \qquad \text{(A.23)}$$

$$\beta = \frac{1}{v}\frac{\partial e}{\partial P}\Bigg)_v \qquad \text{(A.24)}$$

$$k = -\frac{\partial \ln(P)}{\partial \ln(v)}\Bigg)_s \qquad \text{(A.25)}$$

The process continues until the CJ state specific volume converges to a point where very little change occurs between successive iterations. Conditions for the conservation of mass and elemental balance, energy, and final composition, which changes with pressure, are maintained during the operations. The following equations to calculate the final velocities are:

$$D = \left(v_o \frac{P_{cj} - P_o}{1 - \frac{v_{cj}}{v_o}} \right)^{-1/2} \qquad (A.5)$$

$$u_{cj} = D\left(1 - \frac{v_{cj}}{v_o}\right) \qquad (A.1)$$

and from equation A.18

$$c_{cj} = D - u_{cj} \qquad (A.18)$$

Because of the complexity of the program, a complete description is not given. It should be noted that the procedures shown and equations are a small fraction of those required in such a program.

The expansion along the isentrope, starting at the CJ point, is a measure of the performance of the explosive charge. The Tiger and Cheetah code have been written such that the properties along the isentrope may be determined. This allows for the comparison of performance between two different compositions. The Cheetah Code also fits JWL parameters to the isontropic expansion calculations, providing a means to model systems prior to cylinder testing.

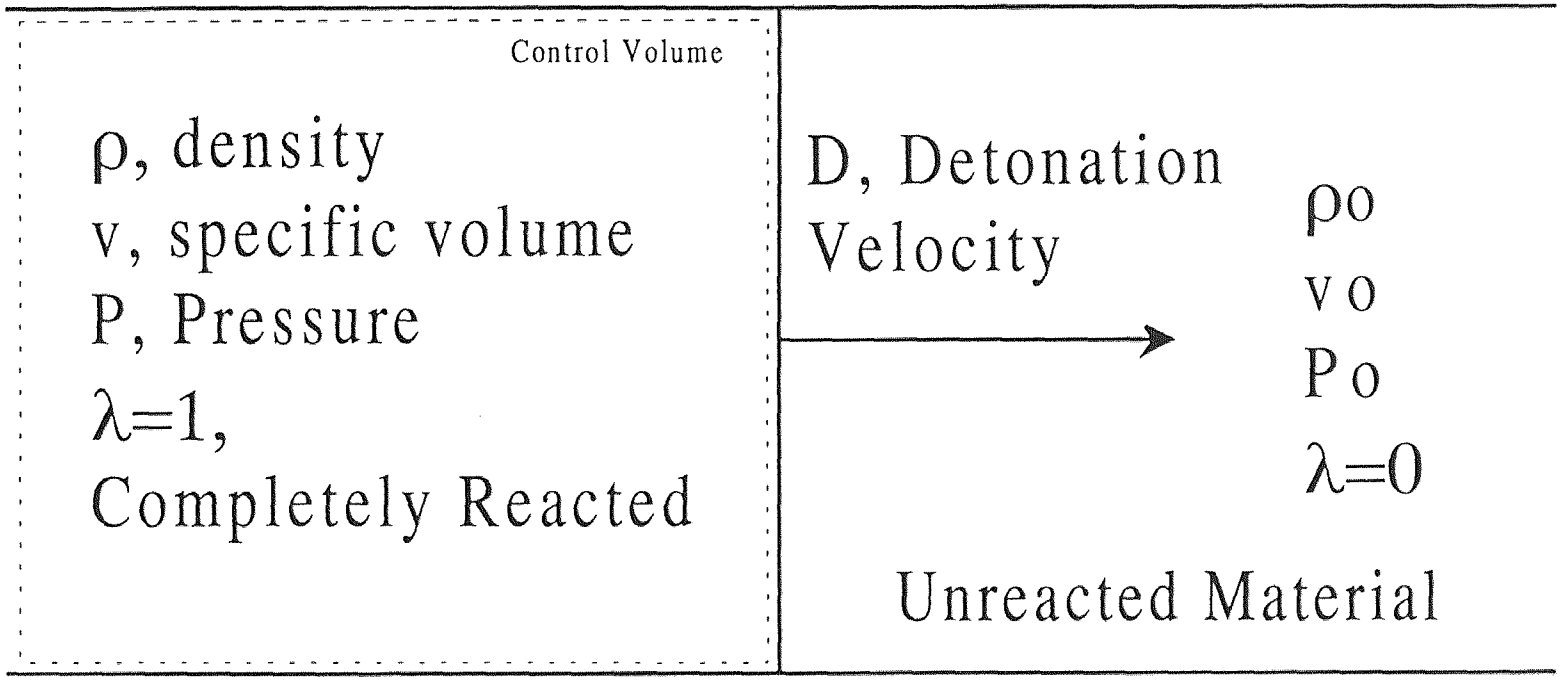

Appendix Figure 1 One Dimensional Detonation

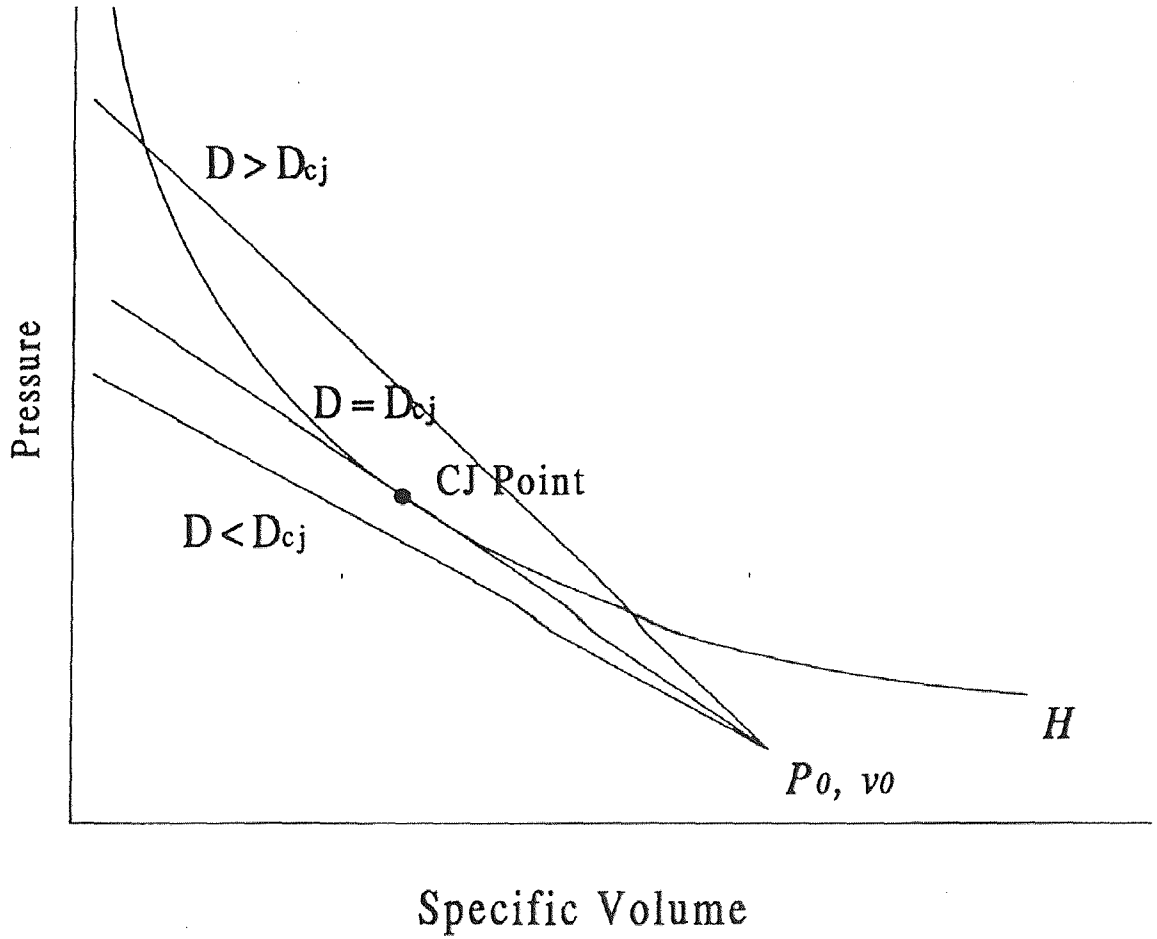

Appendix Figure 2 Rayleigh Lines at Different Detonation Velocities

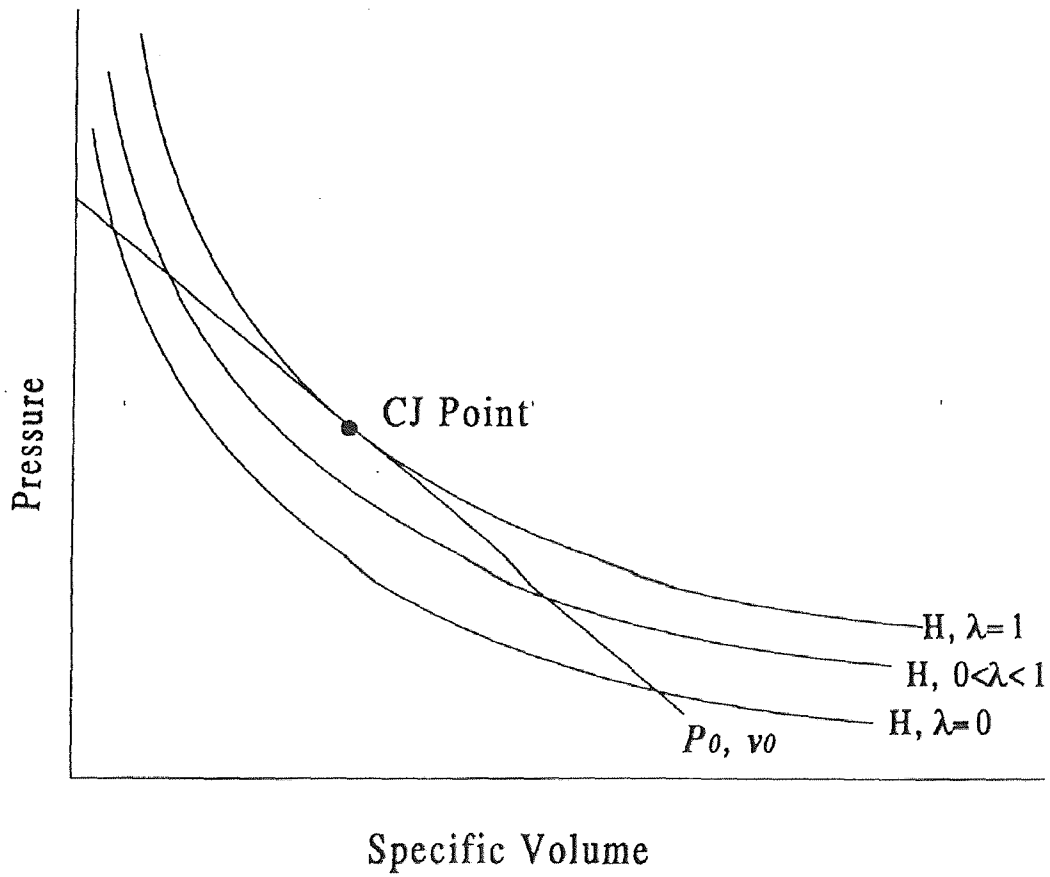

Appendix Figure 3 Hugoniot Curves at Different Degrees of Reaction

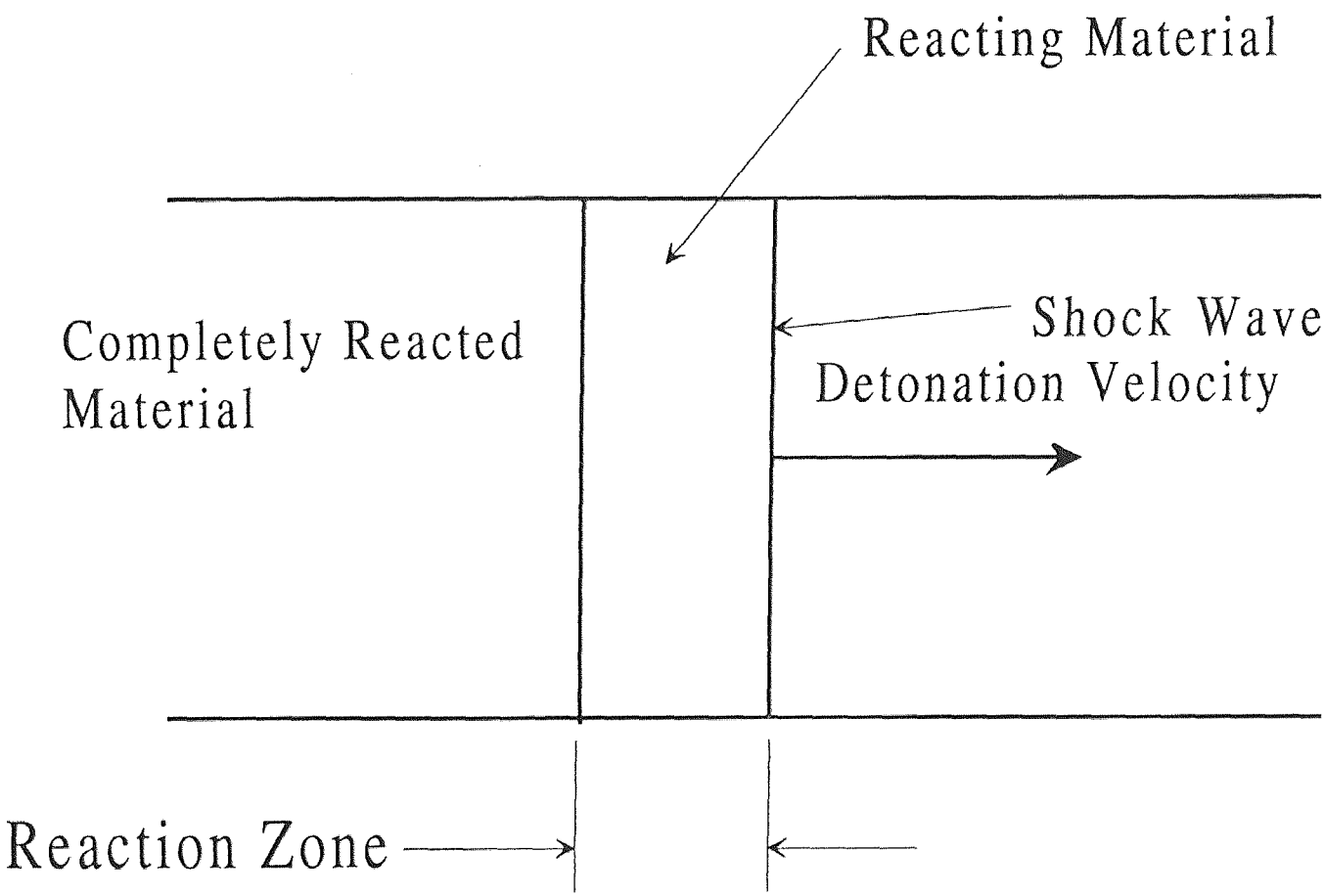

Appendix Figure 4 One Dimensional Detonation with a Finite Reaction Zone

APPENDIX REFERENCES

1. Fickett, W. and W. Davis. Detonation. University of California Press, Berkley, 1979.

2. Baker E. L. Classnotes, Wave Propagation Seminar, University of Washington, 1989.

3. Glassman, I. Combustion Second Edition. Academic Press Inc. New York. 1987.

4. Zeldovich, Ia. B. and A. S. Kompaneets. Theory of Detonation. Academic Press, New York, 1960.

6. Lennard, J. E.-Jones and A. F. Devonshire. Proceedings of the Royal Society. 1937.

7. Cowperthwaithe M. W. and W. H. Zwisler. "Tiger Program Documentation." 1973.

8. Freid, L. E. "Cheetah 1.0 User's Manual" Lawrence Livermore National Labortory, UCRL-MA-117541, 1994.